Baryon Stopping and Charged Hadron Production in Au+Au Fixed-Target Collisions at $\sqrt{s_{NN}} = 3.0$ GeV at STAR

By

BENJAMIN NOAH KIMELMAN
DISSERTATION

Submitted in partial satisfaction of the requirements for the degree of

DOCTOR OF PHILOSOPHY

in

Physics

in the

OFFICE OF GRADUATE STUDIES

of the

UNIVERSITY OF CALIFORNIA

DAVIS

Approved:

Daniel A. Cebra, Chair

Manuel Calderón de la Barca Sánchez

Ramona Vogt

Committee in Charge

2022

To my parents, thank you for fostering my love of science for as long as I can remember,
my brother, David, for always competing with me and pushing me to do better,
and to my partner, Patrick, for helping me to remember to step away from the computer and to enjoy life.

Contents

List of Figures

List of Tables

Abstract

Baryon Stopping and Charged Hadron Production in Au+Au Fixed-Target Collisions at $\sqrt{s_{NN}} = 3.0$ GeV at STAR

The RHIC Beam Energy Scan Phase-I (BES-I) program began a systematic study of the QCD phase diagram with the intent to identify the location of the critical point and prove the existence of a first order phase transition at high baryon chemical potential. While it made progress toward those goals, large statistical uncertainties and an energy range restricted by accelerator design limited the possible conclusions. The second phase of the BES program (BES-II), in conjunction with the STAR Fixed-Target (FXT) program, will allow for more precise measurements and cover a larger energy range.

This dissertation will present the results from the lowest energy of the STAR Fixed-Target program, $\sqrt{s_{NN}} = 3.0$ GeV. Invariant yields of pions ($\pi^{\pm}$), kaons ($K^{\pm}$), and protons (p) are measured in a broad phase-space and, along with the rapidity density distributions of these charged hadrons, will be used to help unravel the relative importance of the different particle production mechanisms. Trends across centrality are investigated, along with trends in collisions energy. These measurements provide an in-depth study of the various production mechanisms for light hadrons and probe unique properties of the high baryon density medium produced in these low energy collisions.

Acknowledgments

This dissertation is a culmination of a lifetime interested in science and has only been possible due to the many mentors who have helped me along the way.

First to my advisor, Daniel Cebra: thank you for the many hours spent helping me grow as a scientist. From going through QA to lengthy discussions on the Δ resonance and baryon stopping, you have helped me to grow my knowledge, independence, and confidence in ways that will last for the rest of my life. Your insistence to always push to the next step or get the additional result for the next meeting, while frustrating at times, showed me the extent of my capabilities, even when I doubted myself. Thank you also to Manuel Calderón de la Barca Sánchez, who has always been available for discussions about STAR tracking or hadron production, and in many ways has been a second advisor and a constant supporter. Thank you to my undergraduate mentor, Brett Fadem, who introduced me to and sparked my interest in heavy-ion collisions at Muhlenberg. You showed me what was possible as a physicist and helped to foster my curiosity.

To my dissertation committee: Daniel, Manuel, and Ramona: thank you for the detailed comments and suggestions for this document. Your recommendations have been invaluable to improving this dissertation. Ramona, your careful reading has found many typos and suggested numerous improvements to content and formatting which make this dissertation readable. Manuel, many of your comments made me question my understanding of STAR software and forced me to dig through the code to gain a more complete understanding.

To my fellow graduate students, Matt and Zach. Matt, your coding practices and organization are perhaps the only reason this analysis is so comprehensive. You have taught me how to keep my code organized (even if I still make copies of functions) and have been invaluable in the many discussions we've had about the mimic method or the physics implications of our results. Zach, I've immensely enjoyed the discussions with you regarding centrality and FXT collisions and wish you luck in the ambitious task of analyzing the higher moments of all the FXT data. To the rest of the UCD NPG, thank you for giving me a home in Davis.

I also would like to thank my family and friends. Thank you to my parents for always supporting me and giving me alarm clocks and computers to take apart. Thank you to my brother for your constant support for providing me someone to argue with. Thank you to Bethany, Anthony, Joni, and Dylan for being there as only family can be; I'll miss being close to you. Thank you to my friends at UC Davis: Ben, Caitlin, David, Davis, Luke, and Rose; you helped me survive first year classes and beyond and have become lifelong friends. Finally, thank you to my partner, Patrick, for your encouragement and for reminding me to take breaks and have fun.

Chapter 1

Introduction

Physics, at its core, is the study of the universe with the intent to describe and predict its behavior. This may seem impossible, and it is, but that doesn't stop us from doing the best we can. Each sub-discipline attempts to do this in its own way, each one attempting to describe quite different aspects of the universe's behavior. Ultra-relativistic heavy-ion collisions, a sub-discipline of nuclear physics, attempts to describe the universe as it was approximately 13.8 billion years ago [1], $\sim 10^{-5}$ seconds after the big bang.

At this early time in the universe's expansion, temperatures were too high to permit quarks to bind into hadrons, let alone form nuclei or neutral atoms. It is believed that this epoch was dominated by a hot, dense medium which was comprised of free quarks and gluons, known as the Quark-Gluon Plasma (QGP). Ultra-relativistic heavy-ion collisions (henceforth shortened to heavy-ion collisions) attempt to recreate these conditions and form a QGP, facilitating the study of the universe at some of the earliest times possible in order to understand its properties.

This dissertation will focus on the methods of hadron production and will attempt to understand the hadron rapidity density distributions, with the purpose of better understanding the dynamics of the QGP medium and its formation. Changing hadron production mechanisms, which can be investigated by measuring hadron yields, are closely related to the energy density of the system and therefore can help understand the medium as it transitions between a hadron gas and a QGP. The yields of pions ($\pi^{\pm}$), kaons ($K^{\pm}$), and protons (p) are measured in fixed-target heavy-ion collisions

at $\sqrt{s_{NN}} = 3$ GeV in a two-dimensional kinematic phase space. This phase space will span the longitudinal (beam) and transverse directions; rapidity characterizes the longitudinal motion and will be used to study how the energy and baryon number shift from the beam to the center of mass of the system, while the transverse motion is used to characterize the thermodynamic environment of the produced fireball.

This first chapter will begin with a brief history of heavy-ion collisions, which will lead into a discussion of the physics addressed in this dissertation, namely hadron production. A motivation for the use of fixed-target collisions will be presented, followed finally by an overview of the work in this dissertation.

1.1 History of Heavy-Ion Collisions

Nuclear physics is the broader field under which heavy-ion collisions falls. As such, it is worthwhile to understand the history of the field, which started with the discovery of the nucleus by Ernest Rutherford. When scattering α particles off a thin gold foil, Rutherford, Giger, and Marsden observed a larger deflection of the incident α than could be described by the plum pudding model (in this model, the atom was thought to be comprised of a positive matrix, the pudding, with electrons studded throughout, the plums), and concluded that the positively charged nucleus was the center of the atom, the rest containing mostly empty space [2].

Upon further investigation, Rutherford observed an anomaly when scattering α particles through nitrogen compared to other gasses. He observed an enhancement in scintillation consistent with that from hydrogen and concluded that protons are present in other nuclei [3], effectively discovering the proton (in reality, Rutherford studied the $^{14}\mathrm{N} + \alpha \rightarrow {}^{17}\mathrm{O} + p$ reaction). Chadwick, in 1932, bombarded beryllium with alphas, which required a neutral particle of similar mass to the proton in order to conserve energy and momentum [4]. In studying the $^{9}\mathrm{Be} + \alpha \rightarrow {}^{12}\mathrm{C} + n$ reaction, Chadwick had discovered the neutron.

The proton, neutron, and electron were considered fundamental particles after their respective

discoveries, but a question still remained: what held the protons and neutrons together to form the nucleus? In 1934, Yukawa proposed the first theory of the strong force, which required a particle with a mass between the electron and proton to mediate the interaction between nucleons [5]. This particle turned out to be the pion, π, discovered in 1947. The study of the strong force then began in earnest.

From this time on, many new particles were discovered, including strange ones, named due to their strange behavior, particularly their longer than expected lifetimes. These strange hadrons were proposed to have a new conserved quantity called "strangeness". As more of these strange hadrons were discovered, patterns in their behavior were observed, leading to the development of the eightfold way by Gell-Mann [6]. With this method of organizing hadrons by their strangeness and charge, Gell-Mann had recognized the SU(3) symmetry of the strong force. From this symmetry, Gell-Mann posited that hadrons were in fact composite particles formed of quarks [7]. However, Gell-Mann was not completely correct in this as he posited that flavor (flavor referring to the quark species) followed SU(3) symmetry, but the known quark masses break this symmetry. Rather, in order for a fully antisymmetric state such as the Ω^- to exist, quarks must have an additional quantum number [8, 9], later called color charge, and shown to have a true SU(3) symmetry [10, 11]. Over the following decades, new hadrons, containing new quarks, were discovered, leading to the Standard Model as we know it.

The Standard Model describes quantum chromodynamics (QCD), the strong interaction, named due to the three "color" charges of the theory. Nuclear physics is the study of QCD, though there are many different aspects to it. Of particular interest to this dissertation are the mechanisms by which hadrons are produced through QCD processes. Fermi, in 1951, developed a statistical model for pion yields [12], which has evolved into modern-day thermal models. Landau expanded on this for nucleus-nucleus collisions by positing that the system expands according to hydrodynamics [13]. This implied a medium that expands and "freezes-out" at a given temperature, predicted by Landau to be comparable to the pion mass.

Hagedorn *et. al.* expanded on this using a statistical bootstrap model, indicating a hadronic

phase boundary [14]. They further go on to say,

> [...] in order to properly understand the approach to the phase boundary, one has to incorporate and understand the properties of the hadronic world beyond the critical curve — we believe that a transition to the quark-gluon plasma phase occurs.

This moved nuclear physics solidly into the modern era, where the sub-discipline of heavy-ion physics has been tasked with understanding the quark-gluon plasma (QGP) and describing the phase transition between normal hadronic matter and the QGP.

1.2 The Physics of Quark-Gluon Plasma

The insight regarding the existence of a new form of matter, the QGP, led to a wave of theoretical predictions of its possible properties, along with methods to measure them. Some of these predictions, such as the suppression of quarkonia or the collective flow of hadrons, directly probe the properties of the QGP. Other predictions, such as the hadron yields, more directly probe the onset of deconfinement and the formation of the QGP. Many measurements have been made over the past 40 years which attempt to characterize the QGP. The Alternating Gradient Synchrotron (AGS) at Brookhaven National Laboratory (BNL) and the Super Proton Synchrotron (SPS) at CERN were two of the first accelerators directly searching for the QGP, with the Relativistic Heavy Ion Collider (RHIC) at BNL and the Large Hadron Collider (LHC) at CERN following them up and performing precision measurements. In 2010-2014, a Beam Energy Scan (BES) program was performed at RHIC to systematically scan collision energies to probe the QGP, identify the threshold for QGP formation, and characterize the phase transition between QGP and a hadronic gas [15]. Many interesting results were obtained from this program, but definitive answers to these questions were not possible, so a second phase to the Beam Energy Scan program (BES-II) was run between 2018 and 2021 with detector improvements and higher statistics to hopefully answer these questions [16]. Numerous exciting results were obtained by various experiments at these and other accelerators, along with various theoretical advances, but only a small selection will be presented in the following paragraphs,

focusing on some of the most important observations regarding the QGP.

Diving deeper into the QGP signatures, we can begin with quarkonia suppression. In the 1980s, predictions were made that heavy quarkonia ($c\bar{c}$ or $b\bar{b}$) could be suppressed by a QGP through a mechanism similar to Debye screening in an electromagnetic plasma [17]. Just as Debye Screening can impede the interaction between two free elecromagnetic charges, so too could the interaction between two color charges in a QGP be impeded, assuming a high enough temperature such that the Debye screening radius is smaller than the quarkonium binding radius. Such suppression has been observed in the J/ψ and Υ states by experiments at RHIC and the LHC. Furthermore, a sequential melting of quarkonia has been observed where more tightly bound states are less suppressed than more loosely bound ones [18]. Such suppression can be investigated using the nuclear modification factor, R_{AA}. The nuclear modification factor is the yield in heavy-ion (AA) collisions scaled by the inverse of the number of binary collisions, divided by the yield in pp collisions; this should indicate an excess ($R_{AA} > 1$) or suppression ($R_{AA} < 1$) of hadrons if there is a medium affecting the production, assuming that the production processes for the hadrons are hard and scale with the number of binary collisions (which is the case for high p_T hadrons, jets, and heavy quarkonia). Hard processes are those which involve a large momentum transfer, such as a large mass or transverse momentum scale, allowing a perturbative expansion in powers of the (inverse) scale, α_s. Figure 1.1 demonstrates this sequential melting with the three Υ states ($b\bar{b}$) measured by CMS [18, 19] where the lower R_{AA} for the Υ(2S) state compared to the Υ(1S) state indicates a larger degree of melting, which is further demonstrated by the Υ(3S) having a lower R_{AA} than the Υ(2S). This sequential melting of quarkonia is a clear signature of QGP formation and can be used to determine the medium temperature at the earliest times, when the QGP is hottest, as the different states should melt at different temperatures due to differing binding energies.

The nuclear modification factor can also be used to study jet quenching, which is another signature of QGP formation. Jets are a cluster hadrons of assumed to originate from a single hard-scattered parton into a single object, the important apsect being the hard-scattered parton. As a colored parton traverses the QGP, it will interact with the medium and lose energy through

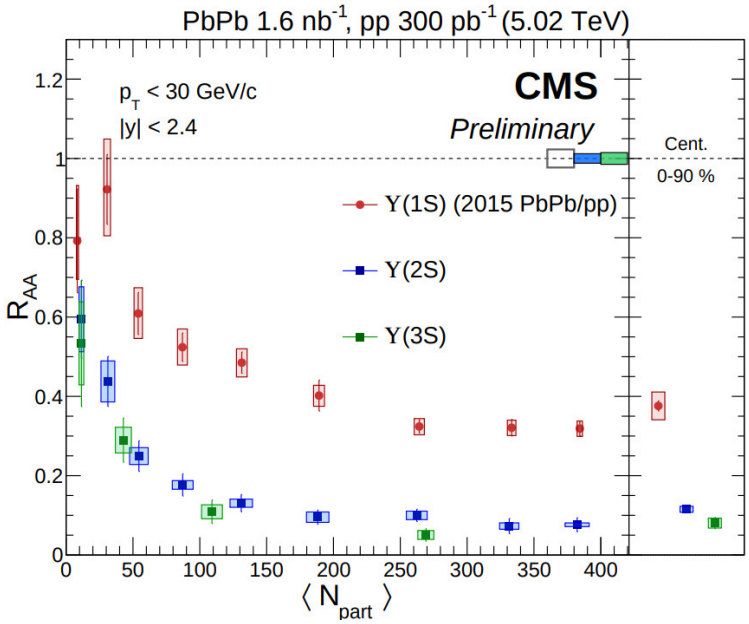

Figure 1.1: Nuclear modification factors for Υ(1S), Υ(2S), and Υ(3S) measured by CMS [18, 19]. Larger suppression of higher mass states with corresponding lower binding energy indicate a sequential melting of quarkonia.

gluon bremsstrahlung [20], similar to the traditional electromagnetic bremsstrahlung. Additionally, a longer path-length within the medium will translate to a larger suppression. Figure 1.2 shows R_{AA} at top RHIC energies from PHENIX, which demonstrates that colored probed (high-p_T final state hadrons) are suppressed, while electroweak probes (direct photons) are not. The jet quenching phenomena are most readily apparent above 6 GeV/c, where hard processes dominate, for pions and etas, where a clear suppression exists. Similar measurements of R_{AA} were some of the first evidence of jet suppression and QGP formation.

Additional effects of the medium on jets have also been observed in dihadron azimuthal correlations, which are a proxy for jets. In this measurement, the azimuthal angle of high p_T hadrons are compared to the azimuthal angle the highest p_T hadron. This creates a distribution with peaks at $\phi = 0$ and π, indicating the production of two back-to-back partons from a 2-to-2 hard scattering process, which hadronize into jets of relatively colinear hadrons. Figure 1.3 is a cartoon of this hard scattering process which creates back-to-back partons. As can be seen, the parton traveling

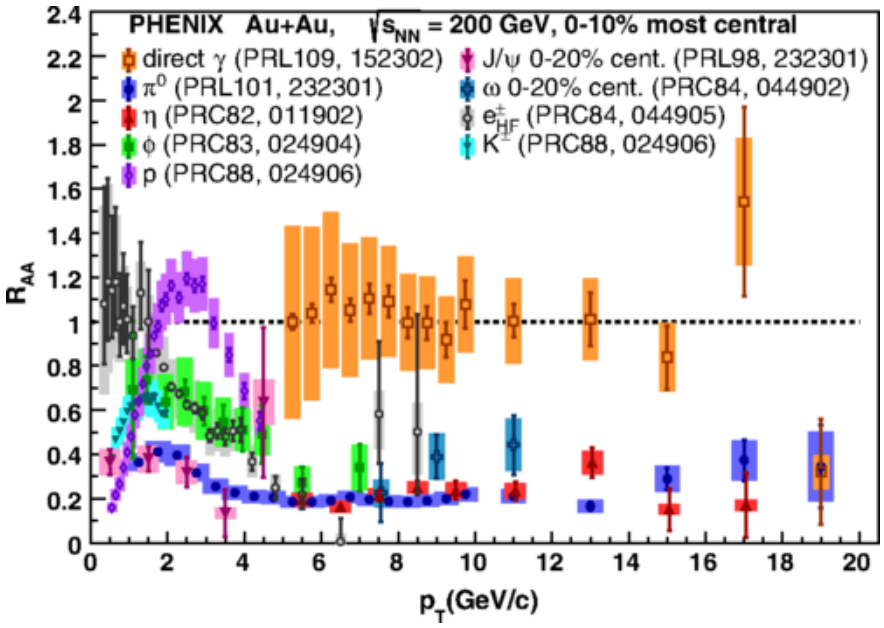

Figure 1.2: Nuclear modification factor for central Au+Au collisions at $\sqrt{s_{NN}} = 200$ GeV from PHENIX [20].

through the medium in the heavy-ion collision will lose energy, causing a suppression of the hadrons from the corresponding jet compared to the *pp* case. Figure 1.4 shows this measurement by STAR and demonstrates an almost complete disappearance of the away-side jet at $\phi = \pi$ compared to the same measurement in $p + p$ and d+Au collisions, neither of which indicate this suppression. Such a suppression in the Au+Au collisions suggests energy loss of the away-side jet within a QGP, reinforcing the idea that a QGP is formed in some collisions at RHIC.

One of the biggest discoveries which underpins much of the modern understanding of the QGP is its near-perfect fluid behavior [23]. Collective phenomena are most easily characterized with hydrodynamics. In non-central heavy-ion collisions where the initial geometry is anisotropic, the large energy densities create an anisotropic flow of hadrons which can be described with relativistic hydrodynamics [24]. This flow can be characterized by the Fourier expansion

$$E\frac{d^3N}{d^3p} = \frac{1}{2\pi}\frac{d^2N}{p_T dp_T dy}\left(1 + \sum_{n=1}^{\infty} 2v_n \cos\left(n(\phi - \Psi)\right)\right), \tag{1.1}$$

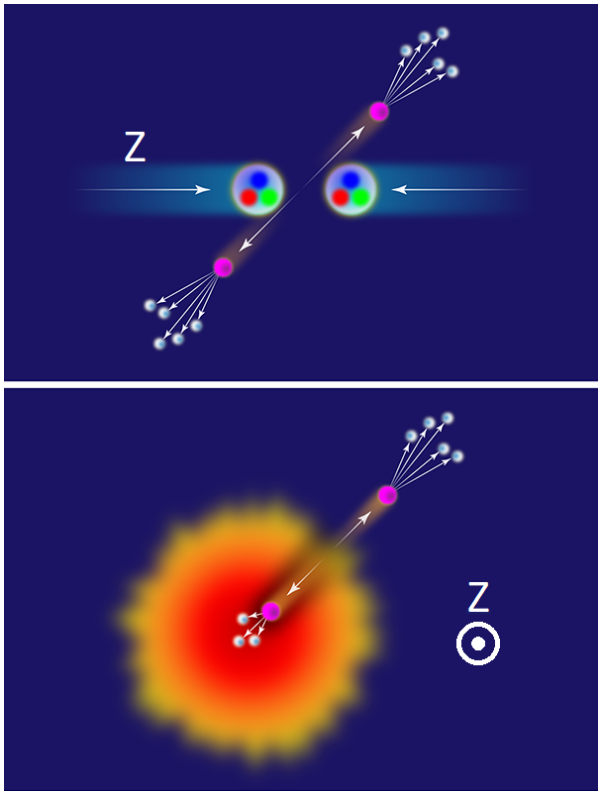

Figure 1.3: Cartoon of a hard scattering process [21]. (Top) Longitudinal plane view in a pp collisions creating two back-to-back partons which hadronize into jets. (Bottom) Transverse plane view in an AA collisions creating two back-to-back partons which hadronize into jets on the surface of the medium, one of which must traverse a larger distance of the medium and is therefore suppressed.

where v_n is the n^{th} order Fourier coefficient, ϕ is the azimuthal angle of the particle, and Ψ is the event plane angle (which is an estimate of the reaction plane and calculated using the flow vectors) [25]. The first two Fourier coefficients, v_1 (directed flow) and v_2 (elliptic flow), are sensitive to the expansion dynamics of the produced medium and are commonly used to characterize its properties. It has previously been shown that the elliptic flow coefficient, v_2, scaled by the number of constituent quarks is consistent across particle species within a few percent, indicating partonic rather than hadronic collectivity [26]. Recent measurements by STAR at $\sqrt{s_{NN}} = 3$ GeV indicate a disappearance of this partonic collectivity (see Fig. 1.5), raising the question of the threshold of QGP formation and questioning the applicability of hydrodynamics if a QGP is not formed. This measurement clearly indicates a change in the behavior of the medium at $\sqrt{s_{NN}} = 3$ GeV.

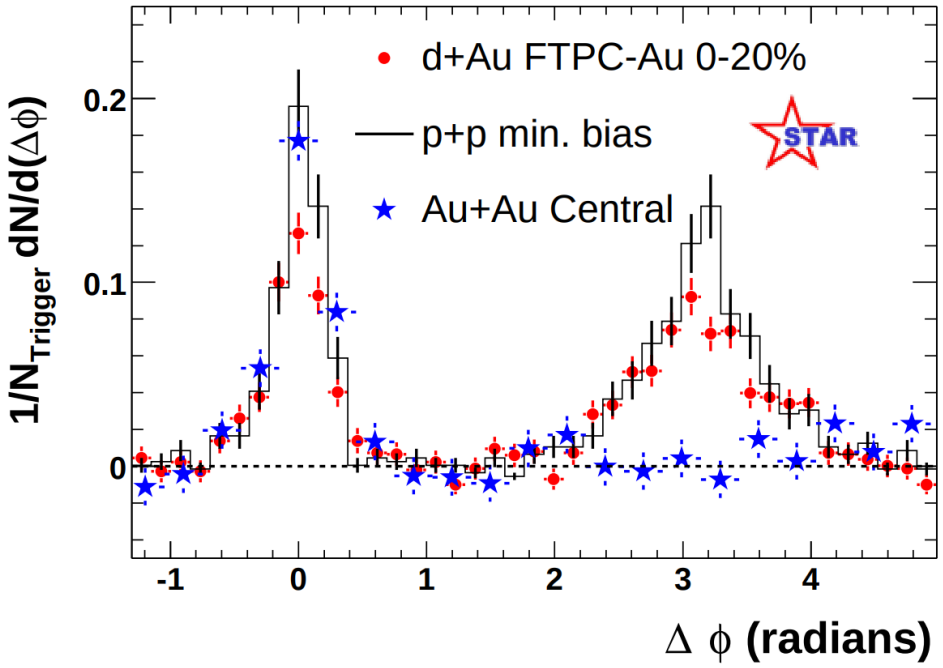

Figure 1.4: Dihadron azimuthal correlations at high p_T from STAR [22]. A suppression of the away-side jet ($\phi = \pi$) is evident in $Au + Au$ collisions (blue stars) while no suppression is observed in $p + p$ (black histogram) or $d + Au$ collisions (red circles), suggesting that such suppression is due to the interaction with the QGP.

As previously mentioned, the QGP is a different form of matter than a normal hadron gas and there must be a phase transition between the two. Measurements of flow can help to identify where partonic collectivity disappears, perhaps indicating the absence of QGP in the corresponding collisions. Another way in which this phase transition is probed is through fluctuations in conserved quantities. Much of this is based on results from lattice QCD, in which space-time is discretized into a lattice, permitting QCD calculations without divergences from finite energy scales due to the large coupling, α_s. Lattice QCD calculations predict a continuous phase transition at $\mu_B = 0$ and $T = 154$ MeV [27]. Baryon chemical potential, μ_B, represents the asymmetry of matter over antimatter, with $\mu_B = 0$ indicating an equal amount of each. At finite baryon chemical potential, other calculations (oscillations and complex components in the QCD Lagrangian cause the well-known "sign" problem causing cancellations, which have, until recently, prevented direct calculation at finite μ_B) indicate

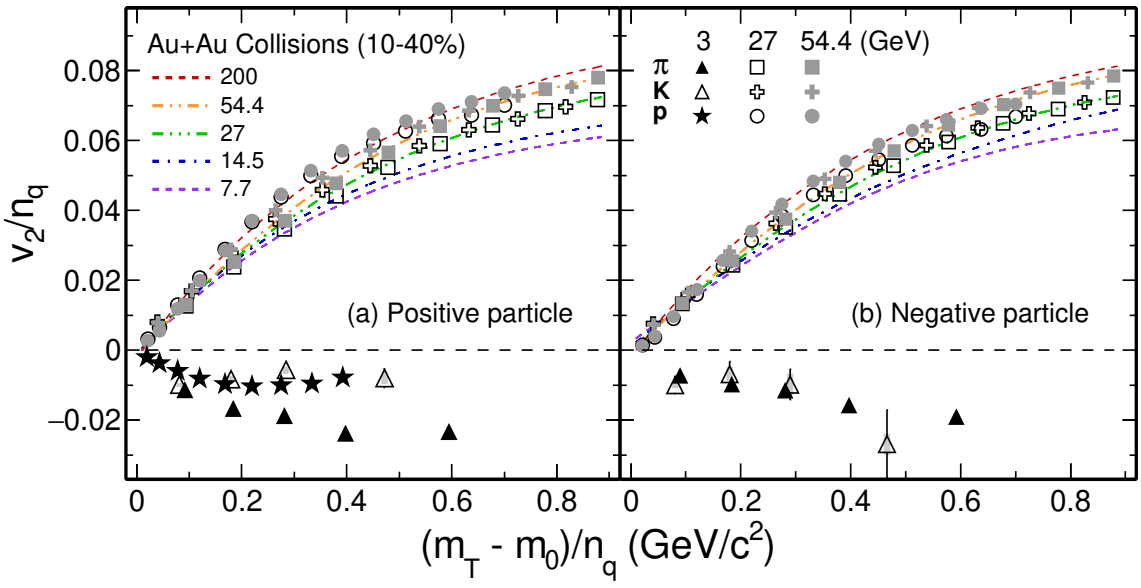

Figure 1.5: Second order Fourier coefficient (elliptic flow) plotted against the reduced transverse mass, both scaled by the number of constituent quarks. This shows good agreement between all particle species at high collision energy, indicating partonic collectivity. The measurement at $\sqrt{s_{NN}} = 3$ GeV does not exhibit the same constituent quark scaling, indicating that the medium has different properties at this energy.

a first order phase transition [28]. The change from a first order to a continuous phase transition requires the presence of a critical point, and finding it is the purpose of studies of fluctuations of conserved quantities.

Conserved quantities, such as baryon number, are expected to be sensitive to the correlation length of the system [29], which diverges at the critical point. The baryon number susceptibility, χ_B, can be directly calculated from QCD, and are directly related to the correlation length, ξ. Ratios of various susceptibilities can be constructed, which have been shown to be equivalent to the ratios of cumulants of conserved quantities [30], with higher orders being more sensitive to the correlation length and therefore can be used as signatures of critical fluctuations. As part of the BES program to search for the critical point, STAR has measured higher-order cumulants of the difference in the number of protons and antiprotons, also called the net-proton number, which is used as a proxy

for net baryon number as neutrons are not measurable with the charged-particle tracking of STAR, the results of which can be seen in Fig. 1.6. These BES-I measurements suggest non-monotonic

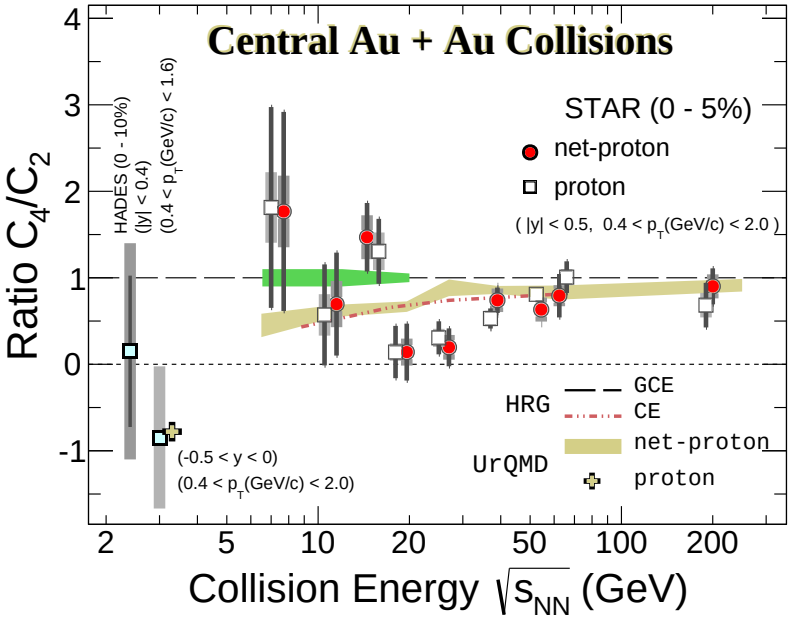

Figure 1.6: Ratio of fourth to second order net-proton cumulants as a function of $\sqrt{s_{NN}}$. Non-monotonic measurements from STAR BES-I hint at critical point around $\sqrt{s_{NN}} = 7.7$ GeV, but large uncertainties preclude a definitive conclusion.

behavior that is consistent with the expectations of a critical point near $\sqrt{s_{NN}} = 7.7$ GeV, but large uncertainties prevent any definitive conclusions. Additional measurements done as part of BES-II will reduce statistical and systematic uncertainties, hopefully identifying the location of the critical point.

One observable which remains to be discussed, and is the focus of this dissertation, is the yields of hadrons. Strangeness production has been proposed as a signature of the onset of deconfinement [31, 32]. The NA49 experiment at the SPS measured the yields of kaons and pions in an energy scan and identified a peak in the K^+/π^+ ratio as a signature of the onset of deconfinement, as shown in Fig. 1.7. While a clear peak can be seen in the ratio of K^+/π^+, no such feature is observed in K^-/π^-. While this may be an indication of the onset of deconfinement, as argued by the NA49

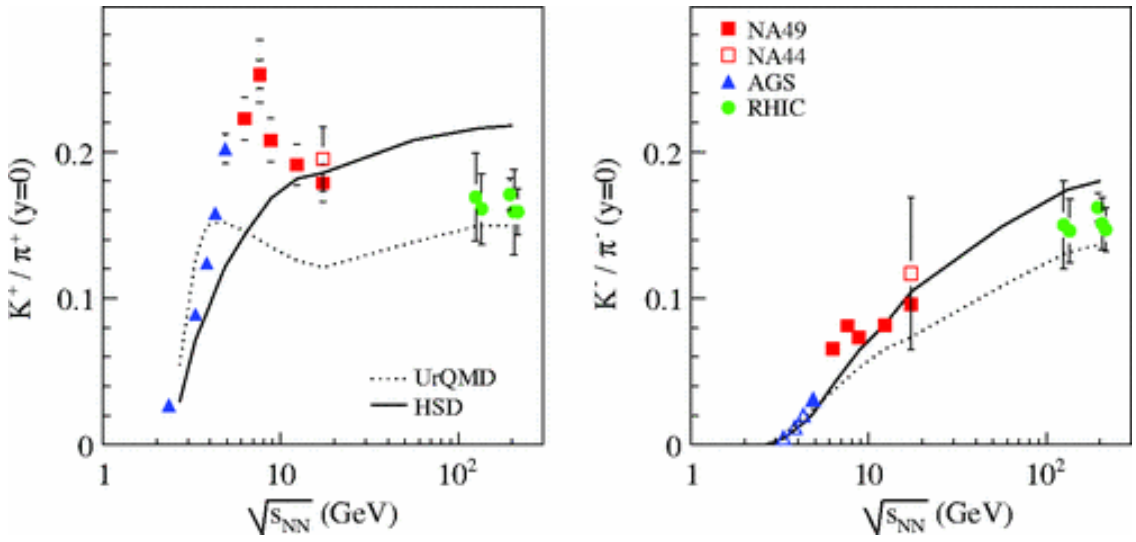

Figure 1.7: Ratio of K/π at midrapidity as a function of center of mass collision energy.

collaboration, it also may be explained by changing mechanisms for the production of pions and kaons. In the energy range where this peak occurs (~ 7 GeV), the kaon production mechanism is changing from K^+ production in association with a Λ baryon to pair production, which would cause a peak in the Λ and K^+ yields, followed by a drop once the $K^+ + K^-$ energy threshold is reached. This change in production mechanism may be enough to account for this dramatic peak and not require an onset of deconfinement, though further study is required to understand the exact cause of this "horn". The work presented in this dissertation will be the first of many high-statistics analyses in the energy range of $\sqrt{s_{NN}} = 3 - 27$ GeV that will help to understand this feature and attempt to identify whether it is due to the onset of deconfinement or changing hadron production mechanisms.

Hadron yields can also be used to determine the location of the collision on the QCD phase diagram, a cartoon of which is shown in Fig. 1.8. Chemical equilibrium models use various parameters (temperature, chemical potentials, suppression factors, and volume) to estimate the yields of all hadrons, and attempt to match measured yields by tuning those parameters. By measuring the yields of hadrons and using them as inputs to different chemical equilibrium models, the chemical freeze-out parameters can be obtained, allowing the position of the collision on the phase diagram to be determined.

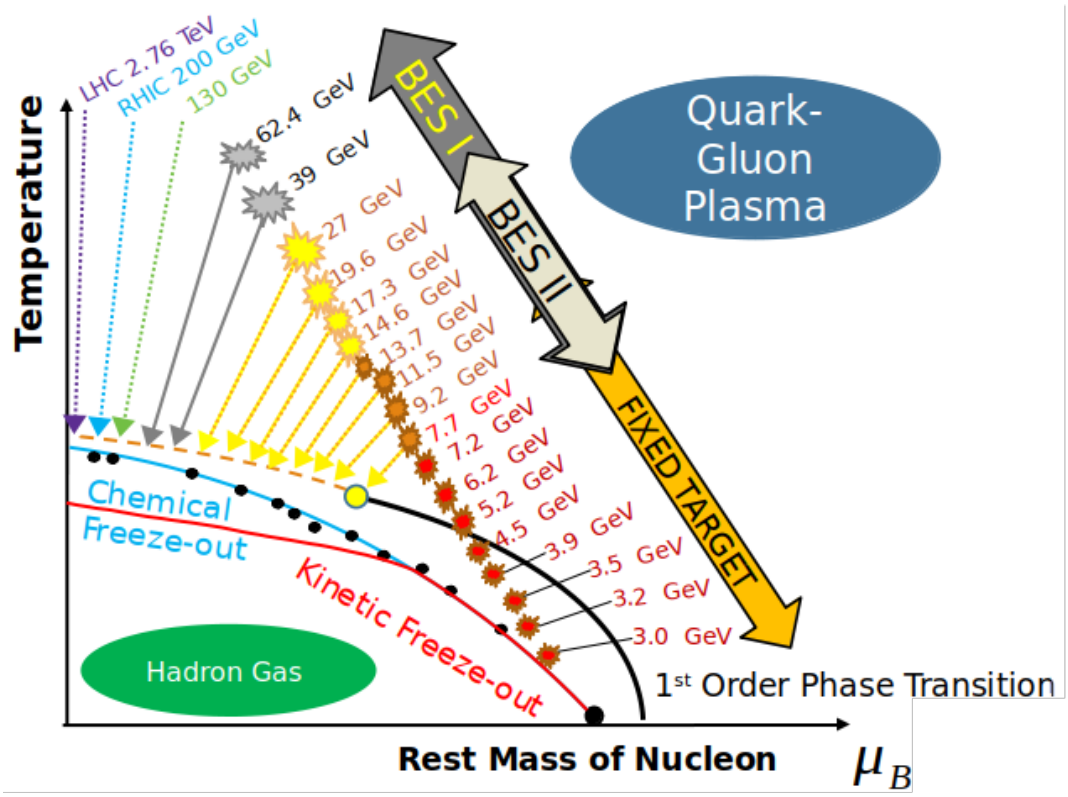

Figure 1.8: Cartoon of the QCD phase diagram with T and μ_B axes. The blue and red curves represent chemical and kinetic freeze-out respectively. The dashed orange curve is an estimate of the continuous phase transition, with the solid black curve representing the first order phase transition. The yellow circle is the location of the critical point. Estimates of where collisions at various energies lie within the phase diagram are shown as blasts of various colors, including energies from the BES-I, BES-II, and STAR Fixed-Target programs.

1.3 Fixed-Target Program

The STAR Fixed-Target (FXT) program is a complement to the BES-II program as it permits the collision of ions at a lower energy than is possible with the RHIC beams. The possible onset of deconfinement at $\sqrt{s_{NN}} = 7.7$ GeV requires measurements at both higher and lower energies. The BES-II program provided the energies above 7.7 GeV and the FXT program provided the ones below, down to $\sqrt{s_{NN}} = 3$ GeV. Additionally, any critical point requires the same: measurements above and below the critical point to ensure any critical fluctuations return to baseline. Some recent

theoretical predictions suggest the critical point is located at even lower energies ($\sqrt{s_{NN}} = 2.5 - 4.1$ GeV) [33], reinforcing the importance of collisions at the lower energies of the STAR FXT program. This section will further discuss the necessity of a fixed-target program at STAR and focus on the physics, while technical details of the program will be discussed in Chapter 3.

RHIC was designed to run as a collider experiment and the RHIC rings were intended to have ions injected with a minimum rigidity, corresponding to a single Au beam with energy of 9.8 GeV. As part of the BES-I program, beams were successfully injected into RHIC below injection energy, down to 3.85 GeV. Attempts were made to inject and stabilize beams at lower energies, but they were unsuccessful. As the superconducting RHIC magnets were designed to operate at a minimum rigidity, their operation at lower currents than designed caused problems with beam stability, preventing the operation of a collider program at energies below $\sqrt{s_{NN}} = 7.7$ GeV. With the installation of a fixed-target in STAR, lower energy collisions became possible. From the Mandelstam variable $s = m_1^2 + m_2^2 + 2E_1E_2 - 2\vec{p}_1 \cdot \vec{p}_2$, it is relatively easy to show that in the center of mass frame of a symmetric AA collision

$$\sqrt{s} = 2E, \tag{1.2}$$

and in a fixed-target AA collision

$$\sqrt{s} = \sqrt{2m^2 + 2Em}, \tag{1.3}$$

where E is the total energy of the nucleon and m is the mass of the nucleon. From these, it is easy to see how collisions with a fixed-target provide center of mass energies lower than those in beam-beam collisions when using the same beam energies. Due to the large cost to construct an accelerator and detector, it is beneficial to use pre-existing infrastructure to perform measurements, which is exactly what has been done with the STAR FXT program. The success of the STAR FXT program also benefited from the experience of the RHIC accelerator division and the STAR operations, software, and analysis teams.

Admittedly, a number of measurements have already been preformed at the AGS and SPS in the energy range covered by the STAR FXT program; however, there are many observables that were not

formulated until more recently, and the previous data are inaccessible or contain too low statistics for these newer measurements. Analyses such as the net-proton cumulants were not performed at the AGS or SPS, and so in order to identify the QCD critical point, this energy range must be studied, particularly if the critical point is in this region as some theoretical calculations predict.

1.4 Overview of Work in this Dissertation

Having discussed the history of nuclear physics, the physics goals and means of observation, and the necessity of a fixed-target program, the remainder of this chapter will present an overview of the work in this dissertation. The primary goal of this dissertation is to obtain the spectra and yields of the light charged hadrons: $\pi^{\pm}$, $K^{\pm}$, and p. These five hadrons comprise the majority of those measured in heavy-ion collisions and allow for an in-depth investigation of the various mechanisms by which each are produced.

The work in this dissertation was performed on Au+Au collisions at $\sqrt{s_{NN}} = 3$ GeV in a fixed-target geometry collected with STAR. Previous spectra measurements have been performed in this energy range by the E895 [34, 35] and E866/E917 [36] experiments at the AGS, but some of these were only midrapidity measurements and all were only in central collisions. The work in this dissertation contains large rapidity coverage measurements of all hadrons across all centralities. These are used to investigate the various hadron production mechanisms: pair production vs Δ resonance production for $\pi^{\pm}$, pair production vs associated production with a Λ for $K^{\pm}$, and baryon stopping for p. Additionally, final state interactions such as the Coulomb potential will be discussed.

To accomplish these goals, the mechanisms by which the ions are accelerated and the methods by which the charged hadrons are measured will be discussed in Chapter 2. Chapter 3 will present technical details on the setup and operation of RHIC and STAR in a fixed-target mode, along with the geometry of such a setup. Chapter 4 will discuss the method used to determine collision centrality and presents the multiplicity cuts used for centrality in the analysis. The data selection requirements are presented in Chapter 5 along with a detailed description of the binning procedure used to create

histograms for the analysis. Corrections to the detector performance are explained in Chapter 6, encompassing acceptance and efficiency, energy loss within detector material, and excess hadrons due to weak decays or interaction with detector material. Chapter 7 describes the methods used to extract the yields of hadrons. Chapter 8 presents the main results of this dissertation: the hadron spectra with accompanying fits, rapidity density and mean transverse momentum distributions, and full phase space yields of each hadron. Chapter 9 presents an analysis of the production mechanism of each hadron using the measured yields and suggests interpretations of the results. Finally, Chapter 10 summarizes and concludes the results of this dissertation.

Chapter 2

Accelerator and Detector

Relativistic heavy-ion collisions are performed at a number of accelerators across the world, each with a different energy range and capabilities. Each detector at these accelerators also has it own unique acceptance and capabilities. The primary accelerators currently in use to study relativistic heavy-ion collisions are the Schwer-Ionen-Synchrotron (SIS18), the Relativistic Heavy Ion Collider (RHIC), and the Large Hadron Collider (LHC). The data used in this dissertation were collected using the Solenoidal Tracker at RHIC (STAR), which is an experiment on the ring of RHIC, located at Brookhaven National Laboratory (BNL) in Upton, New York. This chapter will discuss the details of RHIC and the STAR detector. Particular detail will be given to the subsystems of STAR that are important for the data analysis.

2.1 The Relativistic Heavy-Ion Collider

RHIC is the largest particle accelerator currently in operation in the United States of America and the second largest in the world at the time of this dissertation. RHIC was designed to accelerate gold ions up to 100 GeV/nucleon ($\sqrt{s_{NN}} = 200$ GeV in collider mode or $\sqrt{s_{NN}} = 13.7$ GeV in fixed target mode) and can support stable beams with as little energy as 3.85 GeV/nucleon ($\sqrt{s_{NN}} = 7.7$ GeV in collider mode or $\sqrt{s_{NN}} = 3.0$ GeV in fixed target mode). RHIC also has the unique capability of colliding polarized protons at energies up to $\sqrt{s} = 510$ GeV with up to 60% polarization[37]. The

work in this dissertation focuses on Au+Au measurements, therefore, the remaining discussion will focus on RHIC as a heavy ion accelerator. Figure 2.1 shows a full rendering of the RHIC accelerator complex.

RHIC itself consists of two rings with a circumference of 3.8 km, the yellow beam traveling counter-clockwise around the ring and the blue beam traveling clockwise. A unique feature of RHIC is that these rings are independent, allowing the energy of the beam in each ring to be controlled independently of each other. RHIC also has the capability to be used as a set of storage rings without acceleration, extending the range of energies, though the lowest energy beams determined to be stable are at a total energy of 3.85 GeV/nucleon.

2.1.1 Beam Acceleration Procedure

In order to accelerate Au ions to various relativistic energies, a multi-step acceleration procedure is used. The acceleration procedure begins with an ion source, of which there are two: the Tandem Van de Graff [38, 39] and the Electron-Beam Ion Source (EBIS) [40, 41]. Figure 2.2 shows a schematic of the acceleration phases for both Tandem and EBIS acceleration through the booster and AGS.

Tandem Van de Graff Acceleration

The Tandem Van de Graff has been used as an ion source for the AGS since 1986 and starts with negative gold ions (Au^{-1}), which are extracted from a pulsed sputter ion source. These negative ions are accelerated through a stripping foil and then accelerated again, leaving the Tandem with a kinetic energy of 0.928 AMeV and a charge state of Au^{+12}. The unit AMeV (or AGeV) is one way in which the energy of a heavy-ion beam is identified and represents the kinetic energy of a single nucleon in the beam, where A represents the atomic number and indicates that each nucleon has that kinetic energy; other methods of identifying the beam energy are in the total energy of the beam per nucleon (units of GeV/u) or the center of mass collision energy per nucleon pair ($\sqrt{s_{NN}}$, which requires care, particularly in fixed-target collisions). Upon exiting the Tandem, the ions are further stripped to a charge state of Au^{+31} and are transferred $\sim$ 850 m along a heavy ion transfer

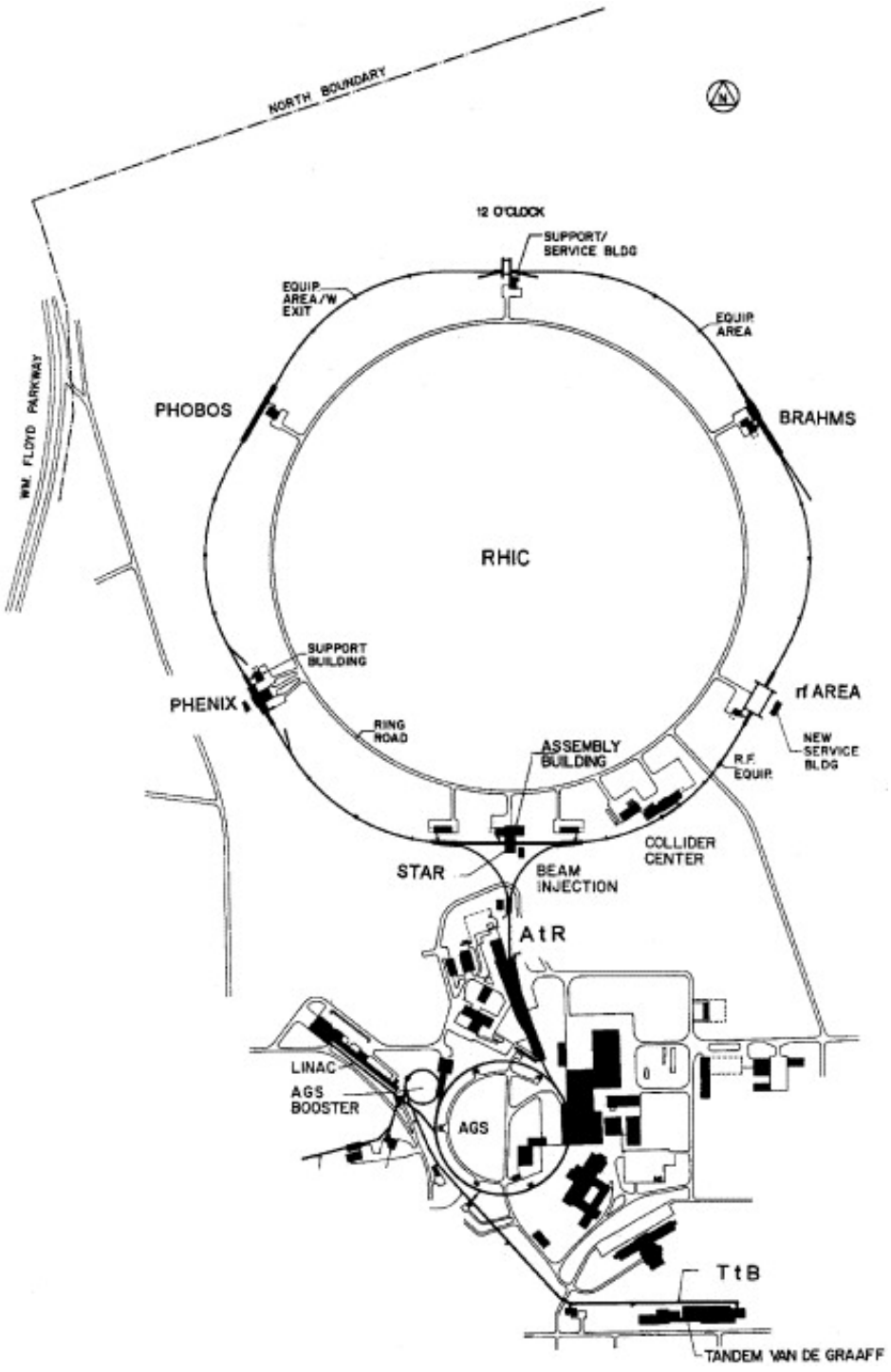

Figure 2.1: Rendering of the RHIC complex, taken from [38].

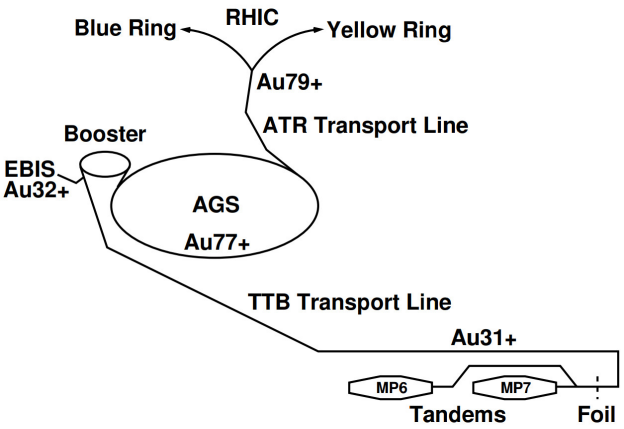

Figure 2.2: Schematic of acceleration procedure from ion sources to RHIC, taken from [40].

line to the Booster. In the booster, the ions are accelerated to 101 AMeV and are ejected into a transport line to the AGS, passing through another stripper along the way leaving them in a charge start of Au^{+77}. In the AGS, the ions are further accelerated to 8.86 AGeV before being sent through another transport line into RHIC, passing through a final stripper along the way to obtain a charge state of Au^{+79}.

EBIS Acceleration

The EBIS began operation as an ion source in 2012 for RHIC in order to provide a wider range of ions for acceleration. An electron beam incident on a gas of gold creates gold ions, which, through some additional acceleration [41], creates a beam of Au^{+32} at 2 AMeV, which is injected into the booster. In the booster, the ions are accelerated to 105 AMeV before being extracted and sent through a stripper on the way to the AGS, leaving the ions in a charge state Au^{+77}. In the AGS, the ions are accelerated to 8.865 AGeV before being extracted and sent through another stripping foil, leaving them in their final charge state of Au^{+79}, before being injected into RHIC.

2.1.2 RHIC Acceleration

Nominal injection kinetic energy into RHIC is approximately 8.86 AGeV, corresponding to a total beam energy of 9.8 GeV/u. RHIC, which is a synchrotron, can then accelerate beams up to

100 GeV/u. As previously discussed, RHIC can be used as a storage ring without acceleration, with beams below injection energy. Stable beams are possible down to a total energy of 3.85 GeV/u, which corresponds to a center of mass energy in beam-beam collisions of $\sqrt{s_{NN}} = 7.7$ GeV. In beam-fixed target collisions, this same beam provides collisions at $\sqrt{s_{NN}} = 3.0$ GeV. The data discussed in this dissertation were collected in 2018 in collisions between a gold beam with total energy 3.85 GeV and a gold target, providing fixed-target collisions at this lowest achievable energy at RHIC. As the beam required for these collisions was below injection energy and RHIC was used as a storage ring, further details on the RHIC acceleration procedure will not be discussed. An overview of the RHIC acceleration procedure can be found in reference [38].

2.2 The Solenoidal Tracker At RHIC

The Solenoidal Tracker At RHIC (STAR) detector, shown in Fig. 2.3, is a large multi-purpose detector with excellent tracking and particle identification (PID) capabilities, along with calorimetry used for high momentum-particles. At the core of STAR is its 0.5 Tesla solenoidal magnet, which operates at room temperature and provides a uniform magnetic field along the z-axis (the beam axis is approximately in the z direction, within a few milliradians). The analysis at hand focuses on particle identification, which is done by the Time Projection Chamber (TPC) and Time of Flight (TOF) detector; therefore, the following sections will go into detail on these subsystems in particular, in addition to details on the STAR fixed-target program. An overview of the STAR detector as a whole can be found in reference [42].

2.2.1 The Time Projection Chamber

The Time Projection Chamber (TPC) is perhaps the most important subsystem in STAR. It consists of a 4.2 m long cylinder, coaxial with the beam pipe in the z-axis (longitudinal direction). The inner field cage has a radius of 50 cm and the outer field cage has a radius of 200 cm, each with respect to the center of the beam pipe, indicating the inner and outer radius of the TPC respectively. The

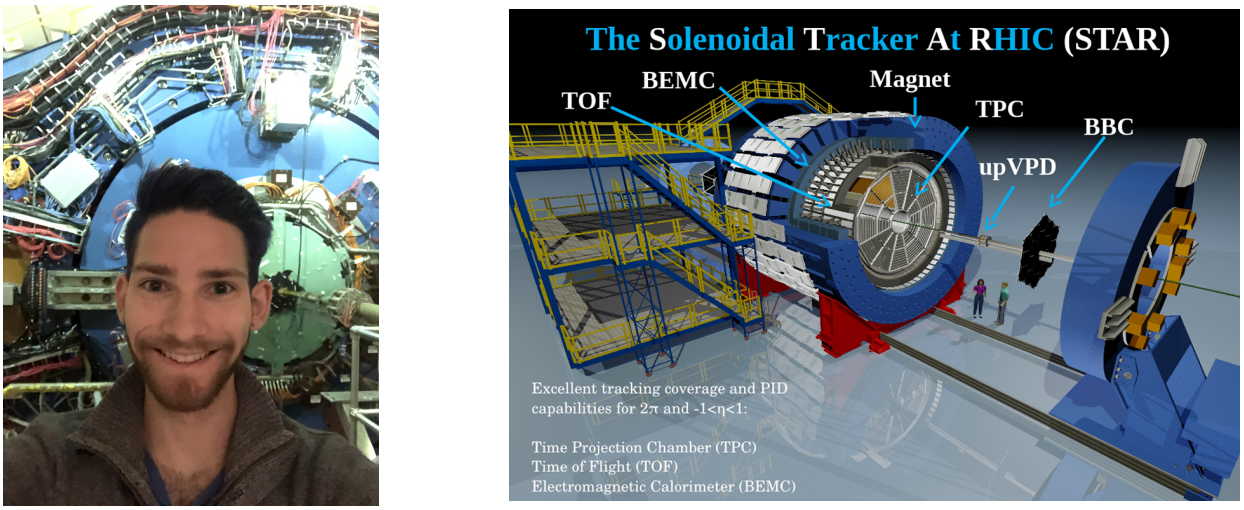

Figure 2.3: (Left) Photograph of the author in front of the STAR detector. (Right) Diagram of the STAR detector and a selection of subsystems [43].

volume of the TPC is filled with P10 gas (90% argon and 10% methane) held just above atmospheric pressure to prevent contamination in case of a leak. The argon is the primary source of ionization electrons and is also inert so that is does not react with any detector materials. The methane acts as an energy absorber due to its large number of rotational and vibrational degrees of freedom; this allows it to absorb kinetic energy from drifting electrons and give them a constant drift velocity. At the center of the TPC (2.1 m from either end) is the central membrane, a cathode held at 28 kV. The central membrane creates a uniform electric field along the z-axis, which is also defined by wire planes at the endcaps, that are held at ground, and resistor chains in the field cages that create equipotential surfaces. Figure 2.4 shows a diagram of the STAR TPC.

The TPC has two main purposes, which are complementary to each other: particle tracking and particle identification. Both rely on charged particles ionizing the gas in the TPC volume, which create ionization electrons. These ionization electrons will drift toward the endcaps due to the uniform electric field; their drift velocity is approximately constant around 5.45 cm/μs due to interactions with gas molecules as previously discussed. Changes in atmospheric pressure, temperature, and humidity can affect the drift velocity, so it is measured regularly using lasers as precisely known locations within the TPC which cause known patterns of ionization and are used to determine

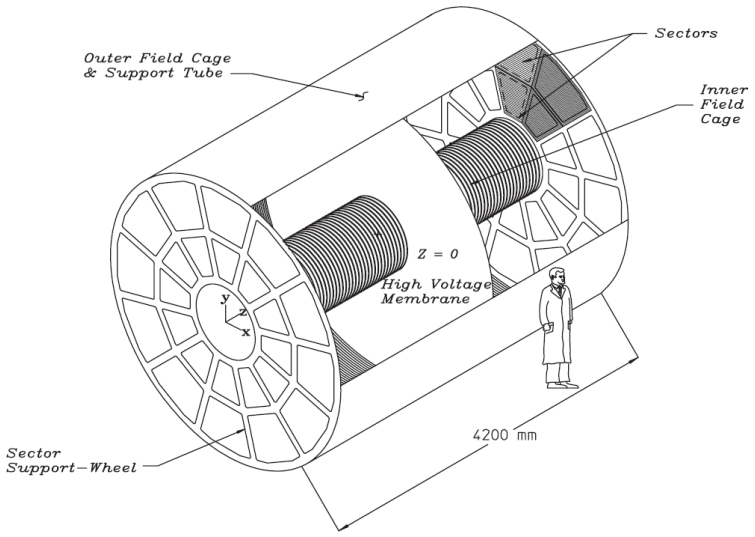

Figure 2.4: Schematic of the STAR TPC obtained from reference [44].

the precise drift velocity. This drift velocity is important as it allows for precise determination of the longitudinal position of the charged particle when used in conjunction with the hit time. By multiplying the known drift velocity by the difference in the measured hit time and triggered collision start time, the time is used to project the measured hit and get the z-coordinate of the ionization point, hence the name Time Projection Chamber. Each endcap of the TPC is azimuthally segmented into 12 trapezoidal Multi-Wire Proportional Chambers (MWPC) which serve as the readouts. Each sector is further segmented into an inner sector, which consists of 13 pad rows, and an outer sector consisting of 32 pad rows. Figure 2.5 shows a schematic of one of these sectors. In 2019, the inner sectors were upgraded by replacing the original 13 pad rows with 40 pad rows. This upgrade greatly increases the rapidity acceptance of STAR, but was unfortunately not in place for the data set discussed in this dissertation. As electrons approach the endcaps, they drift toward the strong fields of the anode wires, which causes an avalanche that amplifies their signal, providing amplification of 1000 to 3000. The corresponding image charge formed on the pad planes is then read out as a signal of the ionization energy lost by the initial charged particle. The two-dimensional position of the pad plane gives the x-y coordinates of the hit.

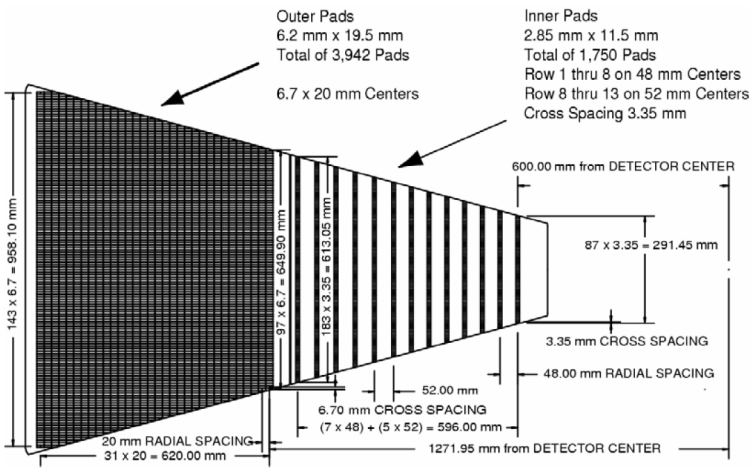

Figure 2.5: Schematic of an MWPC sector of the TPC obtained from reference [44]. The inner portion on the sector is on the right and the outer portion is on the left.

Momentum Determination

In order to determine the momentum of a charged particle, the hits measured in the TPC pads must be reconstructed into tracks. The first step in this process is clustering in which signals from adjacent pads in the x- or y-axis are combined. Hits in adjacent pads with similar drift times are assumed to be Gaussian to determine the centroid, or in some cases a weighted mean algorithm is used, with the deposited energy across the pads added together to get the total energy of the cluster. These discrete clusters are interpolated into continuous tracks with a Kalman filtering process, in which helices are iteratively fit to the clusters. These helicies are parameterized by

$$\begin{aligned} x(s) &= O_x + \frac{\cos\left[\phi + s \times h \times c \times \cos\left(\theta\right)\right] - \cos\left(\phi\right)}{c}, \\ y(s) &= O_y + \frac{\sin\left[\phi + s \times h \times c \times \cos\left(\theta\right)\right] - \sin\left(\phi\right)}{c}, \\ z(s) &= O_z + s \times \sin\left(\theta\right), \end{aligned} \tag{2.1}$$

where O_x, O_y, and O_z are the origin coordinates of the first hit, ϕ is the phase and represents the azimuthal angle, h is the helicity identifying the direction of curvature and is given by $-$sign(qB), where q and B are the charge and magnetic field, c is the curvature and is $1/R$ in the $x-y$ plane,

θ is the dip (polar) angle, and s is a pathlength used to get the coordinates at various points along the helix (where $s = 0$ would be at the origin point). The helix can be used to determine the pseudorapidity of a track using the dip angle or the Distance of Closest Approach (DCA) by calculating the straight-line distance between the vertex and the first hit of the track, among many other quantities. From the helices, the momentum vector of each track can be determined, with direction of the curvature identifying the charge of the track.

Particle Identification with Energy Loss

As charged particles travel through matter, they lose energy due to ionization of the medium. The Bethe-Bloch equation [45] predicts the mean energy loss of a particle per unit path length as a function of its velocity

$$\left\langle -\frac{dE}{dx} \right\rangle = Kz^2 \frac{Z}{A} \frac{1}{\beta^2} \left[\frac{1}{2} \ln \left(\frac{2m_e c^2 \beta^2 \gamma^2 T_{\max}}{I^2} \right) - \beta^2 - \frac{\delta(\beta\gamma)}{2} \right], \tag{2.2}$$

where K is a constant ($K = 4\pi N_A r_e^2 m_e c^2$ MeV $\cdot$ cm^2/mol), $N_{\rm A}$ is Avogadro's number (1/mol), r_e is the classical electron radius ($r_e = e^2/4\pi\epsilon_0 m_e c^2$ fm), ϵ_0 is the vacuum permittivity, m_e is the electron mass, Z is the atomic number of the absorber, z is the atomic number of the incident particle, A is the atomic mass of the absorber (g/mol), β is the relativistic velocity ($\beta = p/E$), γ is the Lorentz factor ($\gamma = 1/\sqrt{1-\beta^2}$), $T_{\max}$ is the maximum energy transfer ($T_{\max} = \frac{2m_e c^2 \beta^2 \gamma^2}{1+2\gamma m_e/m_0+(m_e/m_0)^2}$), m_0 is the mass of the incident particle (MeV), I is the mean excitation energy (eV), and $\delta(\beta\gamma)$ is a density effect correction that is material dependent.

In STAR, a significant amount of effort has been put into characterizing the energy loss of particles in the TPC, which has lead to the use of Bichsel curves [46, 47]. These Bichsel curves have a different shape as a function of the $\beta\gamma$ of the track and a different dependence on the track segment length compared to the Bethe-Bloch curves. Figure 2.6 shows the dE/dx plotted against total track momentum with the Bichsel curves superimposed for π, K, p, and e.

The energy lost will be related to the number of ionization electrons created, which are measured

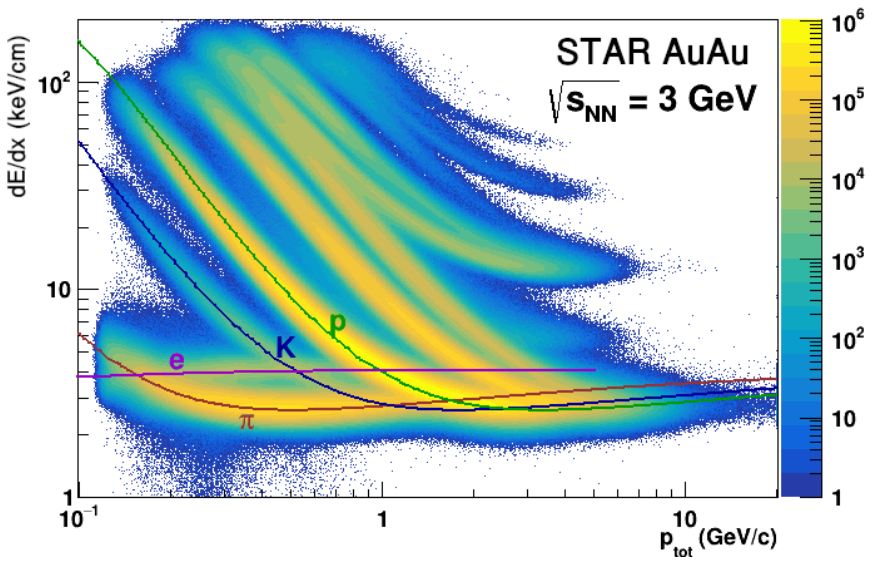

Figure 2.6: Energy loss per unit length (dE/dx) plotted against total momentum of primary tracks for collisions at $\sqrt{s_{NN}} = 3.0$ GeV. Bichsel curves of various colors are superimposed and indicate the most probable predicted energy loss for π, K, p, and e.

by the TPC but not used for track reconstruction nor momentum determination. Each hit point on a track has its own associated energy loss, though each track needs to be given a single value of dE/dx. The probability distribution of the ionization produced by a single track follows an approximate Landau distribution and has a long tail toward high dE/dx values. A maximum-likelihood fit is performed for each track in order to determine the most probable dE/dx, which is then used for particle identification, which will be discussed in Ch. 7. Previously, a 70% truncated mean has been used rather than a maximum-likelihood fit, but the latter produces better fits.

2.2.2 The Time of Flight Detector

The Time of Flight (TOF) detector is also used for particle identification purposes, although it operates through a different mechanism than the TPC. The TOF identifies particles by measuring the time it takes for each particle to hit its active volume from the initial time of the collision. The following will provide a brief overview of the TOF, with more exhaustive descriptions available in [48, 49].

The TOF itself is mounted outside of the TPC at a radius of 2.1 m and is used to measure the stop time for each track. The start time is determined using TPC-identified particles and their corresponding measured stop times, details of which will be discussed later. The TOF consists of 120 trays (60 on each side of the central membrane) with 2π azimuthal coverage and $|\eta| < 1$. Each TOF tray contains 32 Multi-gap Resistive Plate Chamber (MRPC) modules, which are made of a stack of resistive glass plates with freon gas gaps in between the layers. Electrodes are applied to the outer surface of the outer plates which creates a large electric field in the gas gaps. A charged particle traveling through the MRPC will create avalanches in the gas gaps; the total signal being the sum of all avalanches in these gaps. This design provides a timing resolution $\sigma_{\mathrm{TOF}} \approx 100$ ps. Each tray is angled such that particles originating from the nominal vertex position (located at the center of the beam pipe and longitudinally in the center of the TPC) traverse each MRPC perpendicularly. Figure 2.7 shows the geometry of the TOF tiles on one side of the detector for a beam-beam collision at the nominal location.

Figure 2.7: TOF tray side view indicating the angling of tiles, from reference [49].

An algorithm matches tracks from the TPC to hits in the TOF; this matching procedure has an efficiency of only $\sim 60\%$. With the track momentum and known helix, the track is projected to the position of the corresponding TOF hit and that path length, L, is determined. From the path length and the measured time of flight, the speed can be determined:

$$\beta = \frac{L}{c\Delta t}, \tag{2.3}$$

where β is the speed of the particle, L is the projected path length, c is the speed of light in a vacuum, and Δt is the measured time of flight subtracted from the start time. Previously, the start time had been determined using the Vertex Position Detector (VPD); however the VPD requires an East-West

coincidence, which is impossible in fixed-target collisions, and also suffers from background and low statistics in Beam Energy Scan II. Instead, a startless-T_0 (start time) algorithm has been developed, which uses pions identified with their dE/dx with additional requirements on the momentum to remove contamination from other particle species. The expected time of flight of the pion can be calculated by solving Eq. 2.3 for Δt and calculating β with the known track momentum and energy ($\beta = p/E$):

$$\Delta t_{\pi,\text{predicted}} = \frac{L}{c\beta}. \tag{2.4}$$

The start time, T_0, is calculated for each of these pion tracks by taking the difference between the measured stop time from the TOF and the predicted time of flight of the pion, $T_0 = t_{\text{stop}} - \Delta t_{\pi,\text{predicted}}$. An iterative outlier rejection procedure is implemented to remove values which are more then $2.5\sigma_{\text{TOF}}$ (σ_{TOF} is the time resolution of the TOF pad) from the mean across all tracks. Outliers mostly originate from bad matching of tracks to TOF hits or contamination of other particle species into the pion sample. In fixed-target collisions, both protons and pions are used for this startless-T_0 determination, which the author of this dissertation developed for the STAR Collaboration. At the low energies of the STAR fixed-target collisions, the proton yield is higher than the pion yield, causing a large uncertainty in the T_0 when only pions are used, which prompted the addition of protons to the calculation for these collisions. Additional constraints on dE/dx and momentum are implemented to further reduce contamination from other particle species with each track either being identified as a pion or a proton: protons are required to have a positive charge and have a dE/dx within 2σ of the Bichsel mean, pions are required to have a dE/dx within 2σ of the Bichsel mean and positive charges further require $0.2 \leq p_{\text{total}} \leq 1.0$ GeV/c while negative charges require $p_{\text{total}} \geq 0.2$ GeV/c. The same iterative outlier rejection is used and removes contamination from other particles into the pion and proton samples, for which T_0 would deviate significantly compared to properly identified tracks. The time of flight and β for each track are then recalculated using this start time and the measured stop time.

Chapter 3

The STAR Fixed-Target Program

The STAR Fixed-Target program can be traced back to studies done at UC Davis of collisions of the gold beam halo and the aluminum beam pipe in 2009-2011. These initial analyses were a proof-of-concept that the STAR detector, which has been optimized for collisions in the center of the TPC, was able to reconstruct tracks in a very different geometry. The success of these analyses led to a dedicated fixed-target test run, which was conducted in 2015. For this test run, a gold target was installed within the beam pipe upon which the edge of the gold beam was incident, triggering approximately 1M events. This test run provided high enough statistics to perform a number of standard measurements including spectra, flow, and interferometry [50]. This successful test run proved the viability of a fixed-target program at STAR. In 2017, a new target was installed within the beam pipe and the STAR Fixed-Target Program began.

3.1 Experimental Setup

The STAR fixed target consists of a 0.25 mm thick gold foil (corresponding to a 1% nuclear interaction probability) mounted on a half collar with two aluminum support rods. A photograph of the target and support structure can be seen in Fig. 3.1. The target itself is positioned at the west edge of the TPC, which is longitudinally 200 cm away from the nominal interaction point at the center of the TPC. The target is situated at the bottom of the beam pipe such that the top edge of the gold foil

Figure 3.1: Photograph of the STAR fixed target with accompanying support structure.

is 2 cm below the center of the beam pipe. This positioning is important as it prevents unintended collisions between the beam and the target when running in collider mode. When operating in fixed-target mode, the accelerator technicians lowered the beam 1.8 cm until the trigger rate reached 2 kHz, which is the limit of the Data Acquisition (DAQ) system.

When running in fixed-target mode, the accelerator only has one beam cycling. In this configuration, the beam is filled with only 12 bunches, each containing 7×10^9 ions. This limit on the number of bunches separates out-of-time pileup by a sufficiently large distance and also limits the DAQ rate. If two collisions occur too close together temporally, the vertices will appear too close together longitudinally in the TPC and may be reconstructed as a single vertex with a multiplicity equal to the two independent collision multiplicities summed together. To prevent these out-of-time pileup vertices, a reduction of the number of bunches separates them spatially. It was determined that 12 bunches was optimal as that longitudinally offsets these out-of-time vertices by ~ 5 cm, which is sufficiently far from the nominal vertex position to remove with cuts.

3.2 Fixed-Target Geometry

An important distinction between fixed-target collisions and beam-beam collisions (collider mode) is that the center-of-mass and laboratory frames are equivalent for beam-beam collisions but they are different for fixed-target collisions. In fixed-target collisions, the target will be at a laboratory rapidity (or pseudorapidity) of zero, and the beam, by convention, will have a positive rapidity. Rapidity in general is

$$y = \frac{1}{2}\ln\left(\frac{E + p_z}{E - p_z}\right), \tag{3.1}$$

where E and p_z are the energy and longitudinal momentum of a particle. In the case of a beam colliding with a fixed-target, E and p_z are the energy and longitudinal momentum of a particle in the beam. Midrapidity, y_{CM}, lies directly in the middle: $y_{\mathrm{CM}} = y_{\mathrm{beam}}/2$. Midrapidity, while

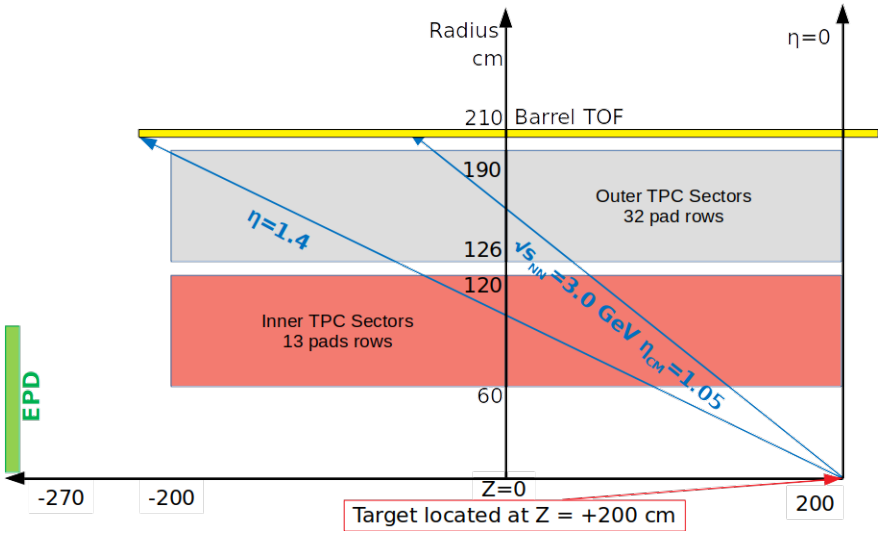

Figure 3.2: Transverse slice of the STAR detector in the laboratory frame. Midrapidity at $\sqrt{s_{NN}} = 3.0$ GeV is labeled and goes directly through the center of the TPC and into the TOF. The far corner of the TOF has a pseudorapidity of 1.4, indicating the approximate limit of particle identification with the TPC in its 2018 configuration.

representing the center of mass of the system, also indicates where the bulk of particle production occurs, and so it is important to understand where it lies with the detector acceptance. In beam-beam collisions, midrapidity lies at $\eta = 0$ and is well within the detector acceptance. In fixed-target

collisions, understanding the location of midrapidity in the laboratory frame will indicate the detector acceptance. Figure 3.2 shows a cartoon of the STAR detector with midrapidity (approximated as the same value of pseudorapidity) displayed for fixed-target collisions at $\sqrt{s_{NN}} = 3.0$ GeV. As this figure shows, midrapidity goes through the entire TPC and hits the barrel TOF, indicating that these tracks are long and have good resolution; it also indicates that these tracks will have good particle identification capability. Furthermore, the pseudorapidity line drawn to the top corner of the bTOF at $\eta = 1.4$ indicated the limit of TOF particle identification, which is essential at higher total momentum. This larger limit indicates that STAR has good acceptance forward of midrapidity as well and that particle identification can be performed both forward and backward of midrapidity.

Chapter 4

Centrality Determination and Cuts

In classical scattering, a useful variable is the impact parameter, b, which is defined as the transverse distance between the centers of the two objects following their original straight-line trajectories [51], as seen in Fig. 4.1. In $p+p$ collisions, such terminology is unnecessary since the collision is really an interaction of the strong fields of the two protons. However, in heavy-ion collisions, which involve multiple nucleons and a much larger size, such a description can be beneficial for characterizing the size of the collision system, which has implications for the medium produced in such collisions as well as for the particle dynamics. Unfortunately, the impact parameter is a measurement that is inaccessible and must be inferred through other means. The primary method for characterizing the size of the collision system is by classifying each collision into one of many centrality bins, each covering a different range of impact parameters. Central collisions (low centrality) are the most head-on and have the smallest impact parameters and the largest overlap of the nuclei whereas peripheral collisions are more glancing collisions and have larger impact parameters and less overlap of the nuclei.

4.1 Centrality Determination

Centrality is defined as a fraction of the $A+A$ total cross section, which is determined by matching a model to the measured charged particle multiplicity. It has been observed that multiplicity, on

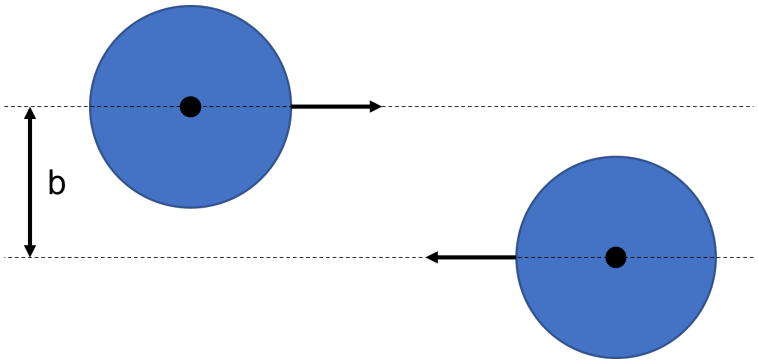

Figure 4.1: Diagram of the collision between two objects traveling in different directions. The impact parameter is labeled as the transverse distance between the centers of the two objects.

average, increases monotonically with decreasing impact parameter (lower centrality). The centrality variable which has been decided on for use in fixed-target collisions is called FXTMult (short for fixed-target multiplicity), defined as the number of primary tracks in the picoDSTs (for calculation purposes, it is the number of tracks in an event with "isPrimary()==true", identifying that the track originated from the primary vertex). picoDSTs are a file structure used in STAR to store data and which many analyses use. The FXTMult variable for this data set can be seen in Fig. 4.2 as the black data points. In STAR data collected in collider mode, this multiplicity is normally limited to a pseudorapidity range $|\eta| < 0.5$ in order to stay toward the center of the detector where the acceptance and particle reconstruction efficiency is highest to ensure consistency across a wide range of vertex positions. In the Fixed-Target collisions presented here, such a restriction is unnecessary as the collision vertex is always in the same location (within the target), so there are no such concerns about changing acceptance and efficiency and, therefore, the entire TPC acceptance is used.

4.2 Glauber Monte Carlo Model

A two-component model is used to determine the centrality. The first component is a Monte Carlo (MC) Glauber Model, which is used to simulate two gold nuclei, with nucleons randomly distributed according to a Wood-Saxon density, colliding with a random impact parameter. The main assumption of this Glauber Model is that an $A + A$ collision is a superposition of some number of $p + p$ collisions.

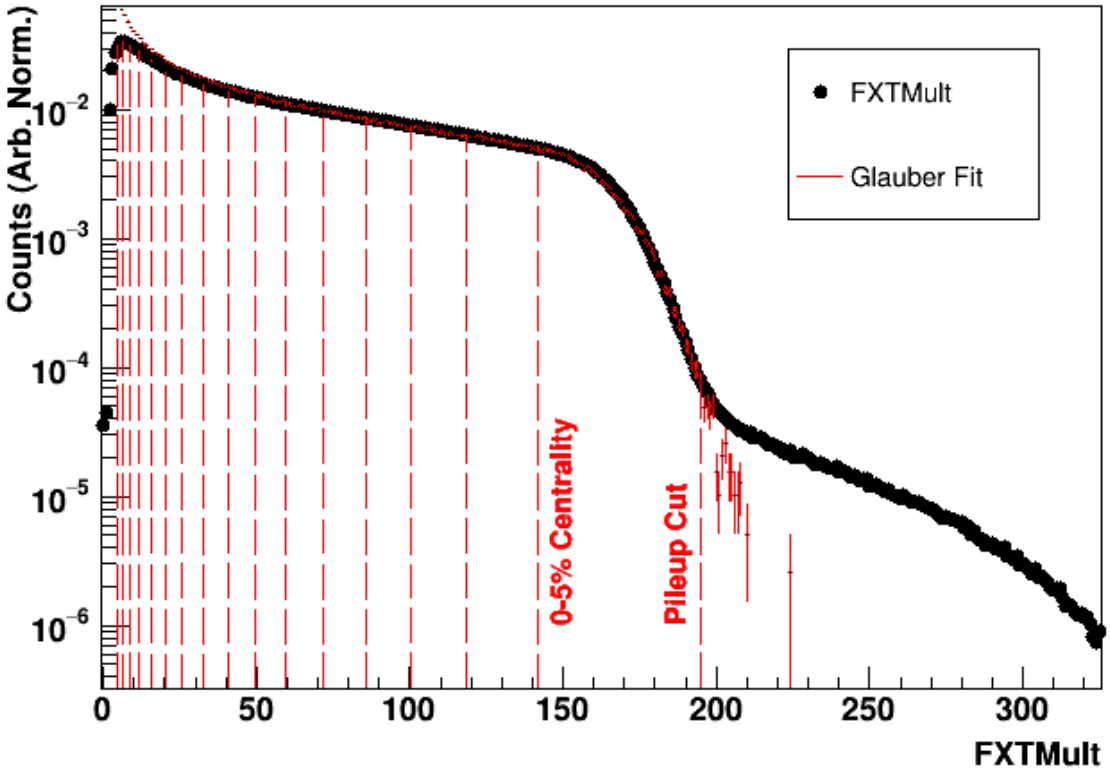

Figure 4.2: Centrality selection for STAR FXT Au + Au collisions. The centrality variable is the number of primary tracks within the entire TPC acceptance. The black points are the data and the red curve is the Monte-Carlo Glauber + negative binomial fit to the data. Vertical lines indicate the minimum number of tracks required for an event to be in the corresponding centrality bin. Events with a multiplicity greater than 195, where the pile-up line is drawn, were excluded from all analyses since this region of multiplicity is dominated by pile-up events.

A nucleon from one nucleus can collide with another nucleon from the other nucleus if their randomly generated positions are within a certain transverse distance from each other, which is related to the $p+p$ inelastic cross section ($d < \sqrt{\sigma_{\text{inel}}^{NN}/\pi}$). For this Glauber Model, a nucleon-nucleon inelastic cross section of $\sigma_{\text{inel}} = 28.2$ mb was used, determined by fitting $p+p$ total and elastic cross section data [45] and taking the difference (checks at various energies were performed and confirmed that the fits accurately describe the data). Each nucleon from one nucleus has its transverse position compared to those in the other nucleus to identify if it is within the threshold distance, and if so,

the number of binary collisions, N_{coll}, is increased along with the number of participating nucleons, N_{part}. Each nucleon can be counted as a participant only once, but can undergo multiple binary collisions. By employing the Glauber model, distributions of the number of N_{part}, N_{coll}, and impact parameter are created.

The second component is a particle production model which uses a Negative Binomial Distribution (NBD) to randomly produce particles. The NBD itself has two parameters, μ, which controls the turnover position, and k, which is called the shape parameter and controls the slope. For each MC collision, a NBD is sampled m times, where

$$m = xN_{\text{coll}} + (1-x)\frac{N_{\text{part}}}{2}, \tag{4.1}$$

and x is the hardness parameter, which determines the contributions of hard collisions ($x \sim 1$) which scale with N_{coll} vs. soft collisions ($x \sim 0$) which scale with $N_{\text{part}}/2$.

This is a three parameter problem with x and the two NBD parameters: μ and k. This distribution of simulated produced particles is compared to the measured charged particle multiplicity to find the three parameters which provide a shape that best matches the data. Both the data and MC Glauber model are normalized in the same region, between multiplicities of 40 and 195, the higher end being the pileup cut. By scanning this three-dimensional parameter space, it was determined that the optimal parameters which best reproduce the multiplicity data at $\sqrt{s_{NN}} = 3.0$ GeV are $x = 0.0$, $\mu = 0.90$, and $k = 39.98$. The value of x being zero indicates that there is only soft hadron production in these collisions, in contrast to collisions at top RHIC energy where $x = 0.14$ and there is a noticeable contribution from hard processes, or at LHC energies where $x \sim 1$ and hard production dominates. The Glauber fit with these parameters is shown in red in Fig. 4.2. These parameters produce a $\chi^2/\text{DOF} = 620$, which is reasonable given that the pileup tail is not being fit and the model does not account for the trigger inefficiency. Given this fit, the trigger efficiency is 72%, calculated by dividing the integral of the data by the integral of the Glauber fit, both from zero to the pileup cut.

4.3 Centrality Cuts

In order to obtain the centrality classes, the simulated multiplicity distribution is integrated from the highest multiplicities down toward low multiplicity until 5% of the total multiplicity is obtained. Multiplicity is an integer value so the centrality cut is defined by the multiplicity where the integral passes the 5% threshold. This process is repeated, adding on 5% of the total multiplicity each time, to define all multiplicity cuts for each centrality bin. In each centrality class, the mean N_{part} and N_{coll} are also obtained by creating distributions of those variables based on the multiplicity cuts. In the analysis done for this dissertation, seven centrality bins were defined to improve statistics for the more peripheral collisions, for which the multiplicity cuts and $\langle N_{\text{part}} \rangle$ and $\langle N_{\text{coll}} \rangle$ can be found in Tab. 4.1.

Centrality Range	FXTMult Range	$\langle N_{\text{part}} \rangle$	$\langle N_{\text{coll}} \rangle$
0-5%	195-142	334.4 ± 6.5	717.5 ± 23.6
5-10%	141-119	287.0 ± 10.0	588.0 ± 21.5
10-20%	118-86	224.2 ± 11.4	425.3 ± 23.3
20-30%	85-60	159.6 ± 8.7	271.8 ± 16.5
30-40%	59-41	110.4 ± 6.3	167.2 ± 10.7
40-60%	40-16	59.1 ± 5.7	74.4 ± 8.3
60-80%	15-5	20.2 ± 2.0	19.0 ± 2.4

Table 4.1: Centrality cuts for FXT $\sqrt{s_{NN}} = 3.0$ GeV with corresponding $\langle N_{\text{part}} \rangle$ and $\langle N_{\text{coll}} \rangle$ used in this analysis.

Chapter 5

Data Selection and Binning

The data for this analysis were collected over a five-day period starting on May 31, 2018 through June 4, 2018. The yellow beam only was circulated with 12 bunches, which allowed the highest DAQ rate possible while separating out-of-time pileup by a far enough distance (~ 5 cm) so that out-of-time tracks are not pulled into the primary vertex by the vertexing algorithm. The center of the beam was lowered by 1.8 cm so that the edge of the halo would scrape the top of the fixed target (located 2 cm below the center of the beam axis). During data collection, a fast version of the reconstruction chain is run in order to provide quick feedback on data quality, called the High Level Trigger (HLT). The RHIC operators kept the rate of the HLT-good trigger, a trigger indicating the number of good events identified by the HLT, near 2 kHz throughout the data collection by defocusing the beam. This was the first official physics data set of the fixed-target program and the dedicated work of the RHIC operators, STAR Operations team, STAR detector experts, and the shift takers allowed us to develop a conduct of operations that have worked well for the rest of the fixed-target data collection.

A total of 337M events satisfied the main trigger, 257M of which also satisfied the HLT-good conditions. The original data production had a similar number of good events compared to the HLT good number. Due to some observed issues, particularly with the startless-T_0 algorithm discussed in Ch. 2.2.2, a new production of the data was completed using the SL20d Library. This has one main change: the startless-T_0 algorithm included pions and protons (previously it only included pions)

which improved the acceptance for peripheral events.

5.1 Bad Run Rejection

As with any other data set, bad runs had to be identified and removed from analysis. This was done by performing run-by-run QA on the picoDSTs and making plots of the mean of various observables as a function of the run. For each observable, the mean and RMS across all the runs are found and any run where the observable is one or more RMS away from the mean is flagged. Each flagged run is investigated further to evaluate the deviations more closely. From this, two separate bad run lists were constructed.

The first bad run list is a smaller list which removes fewer runs and is intended for more robust analyses (the present analysis included). For this list, any run that was flagged as having an observable deviating from the mean was investigated further and individually determined if it should be removed or not. The vast majority of flagged runs are removed, except for those flagged because of only having DCA variations. Once the runs on this list are removed, 275M events remain for analysis.

The second bad run list is a much larger list which removes many more runs and is intended for more sensitive analyses (such as the net proton higher moments). Any runs that were flagged for any reason are placed on this list and removed without question. Additionally, the first two and a half days of data taking were removed since beam conditions were changing and the conduct of operations was still under development. Once the runs on this list are removed, 147M events remain for analysis, which is less than half of the original statistics. While this is a significant drop in statistics, it is important for sensitive analyses to use as clean of a data sample as possible, which is why we recommend this bad run list for those analyses.

These bad run lists were been presented to the main Physics Working Groups dealing with fixed-target and BES-II analyses in STAR, along with the STAR Quality Assurance (QA) Board. The STAR QA Board was formed in 2019 and tasked with monitoring data quality both during

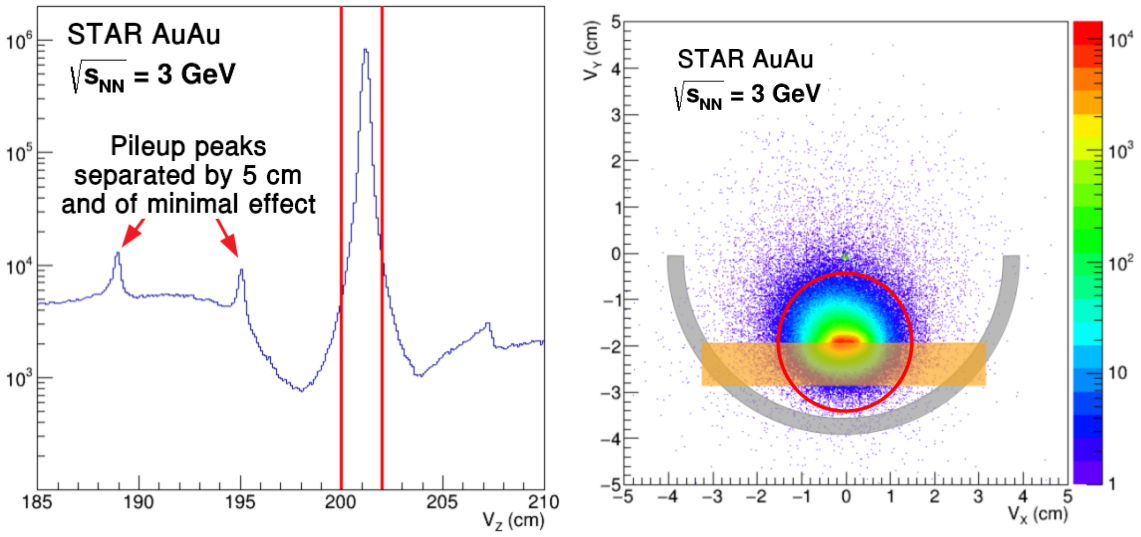

Figure 5.1: (Left) Longitudinal vertex distribution with cuts overlaid in red ($198 \leq V_z \leq 202$ cm). Clear out-of-time pileup peaks are visible, each separated by approximately 5 cm due to the use of only 12 bunches. (Right) Transverse vertex distribution with radial cut overlaid in red ($V_r < 1.5$ cm, centered at $[-2, 0]$). A cartoon of the target and aluminum support structure is also overlaid.

data collection and in the official production process; part of its duty is to determine bad run lists for each data set for general use within the collaboration. The bad run lists for this data set were approved as official for the collaboration to use.

5.2 Event Selection

To ensure that only high-quality events were used in the analysis, the primary vertex of the collision was required to be within the region of the target ($V_z = [198, 202]$ cm) and be within a radius of 1.5 cm of the center of the beam spot (which is located at $[-2, 0]$ cm). The radial vertex cut removes collisions with the beam pipe, which would occur 2 cm below the center of the target. Figure 5.1 shows the vertex position prior to any selection cuts, with an overlay of the target on the transverse distribution.

In addition to vertex cuts, events were required to have the bbce_tofmult1 trigger (offline ID 620052) which required a signal in the East BBC and 5 or more hits in the barrel TOF. An additional

offline cut requires that one or more tracks is matched with a hit in the bTOF.

5.3 Track Selection

In all events that passed the event selection requirements, all tracks are further evaluated. The main goal of this track selection procedure is to select only primary tracks which came from the original collision and not from decays of particles or secondary interactions, and also to not double count any tracks which were by some error split into two pieces (this occasionally occurs to tracks which cross the central membrane of the TPC, which many do in Fixed-Target collisions).

In order to ensure that each track originated from the primary vertex, two cuts are implemented. First, a cut requires the distance of closest approach (DCA) of each track from the primary vertex be less than 3 cm (DCA $\leq$ 3 cm) which ensures that the track originated at the primary vertex. Each track is also required to have the "isPrimary()==true" flag as this means the track was successfully refit with the vertex as an additional hit point along its trajectory.

To prevent the double counting of tracks, three cuts are implemented. The first requires the number of hit points used to reconstruct the track be greater than or equal to 15 (nHitsFit$\geq$ 15). In 2018, when these data were collected, the inner TPC sectors had 13 pad rows (indicating the number of possible hit points in the transverse plane) and the outer sectors had 32 pad rows; the cut requires greater than 15 hit point in the track reconstruction and ensures that a track is not mistakenly split across the inner and outer sectors and, if it is, only the outer portion will be kept, preventing double counting of that track. Similarly, a ratio of the number of hits fit to the number of possible hits on the track (which is obtained by projecting the helix of the track through the TPC and identifying how many hit points it could have) is required to be greater than 51% in order to ensure tracks are not split across the central membrane and, if they are, only the longer portion is kept. Finally, a cut requires that the number of hits used for dE/dx is greater than or equal to 10 to ensure that the dE/dx information is of high quality since it is the core of particle identification (in reality, most tracks use all of their hit points for the dE/dx calculation, so this cut is just a fail-safe).

5.3.1 TOF Track Selection

In addition to the track selection cuts presented above, many tracks (approximately 70%) are matched to hits in the Barrel Time of Flight, the data from which is also required to pass certain quality cuts. Not all tracks are required to pass the following cuts, only those which have a TOF match. Furthermore, the following cuts are also only applied to TOF data and any track that has such data but fails to pass the following criteria is still used in the TPC data. For any track that has a match to a bTOF hit, the first step is to get the corresponding hit and cross-check that it has been matched to a track. Next, the 2D location of the hit along the bTOF tile position is required to be in the center of the active region of each tile, with constraints of $|Z_{\text{local}}| < 2.8$ cm (longitudinal along the beam direction) and $|Y_{\text{local}}| < 1.6$ cm (along the ϕ direction). These cuts reduce the number of mismatches which cause background in the yields; these mismatches are when the dE/dx from the TPC and the m^2 (or $1/\beta$) from the TOF suggest different particle species, which occurs more frequently when the TOF hit is further from the center of the tile, indicating why such a constraint is implemented. An additional cut requires $\beta \geq 0$ since that is a physical threshold and anything lower would imply a negative velocity.

5.4 Data Binning

From the events and tracks that pass the quality cuts discussed above, numerous multidimensional distributions are constructed. There are three sets of histograms constructed for the analysis: m^2, Z_{TPC}, and TOF-identified Z_{TPC}. m^2 contains data from the TOF, Z_{TPC} contains data from the TPC, and TOF-identified Z_{TPC} contains data from the TPC that has been used mass restrictions from the TOF to identify certain particle species. Chapter 7 will go into more detail regarding the construction and use of each of these distributions. Events are binned into seven centrality bins, which were defined in Tab. 4.1. Tracks belonging to events within each centrality bin are further binned by rapidity, y, and reduced transverse mass $m_T - m_0$. Transverse mass, $m_T = \sqrt{p_T^2 + m_0^2}$, has a close relationship to the total energy, $E = m_T cosh y$, and longitudinal momentum, $p_z = m_T sinh y$,

while m_0 represents the known PDG mass [45] of the particle in question. Reduced transverse mass, $m_T - m_0$, is used in this analysis as it has a value of zero when p_T is zero (which is not true for m_T alone) and is also the variable used in previous analyses at similar energies, which allows for easy comparisons. Rapidity bins each have a width of $\Delta y = 0.1$ and cover the range $y_{\mathrm{CM}} = [-0.95, 0.75]$ (this corresponds to $y_{\mathrm{lab}} = [-1.8, -0.1]$). Bins were chosen to have the same width as previous measurements with midrapidity, $y_{\mathrm{lab}} = -1.05$, at the center of a bin. Transverse mass bins have a width of $\Delta m_T = 0.05$ GeV and cover the range $m_T - m_0 = [0, 2.5]$ GeV, bins were chosen to be small enough such that the total momentum range covered by each bin is sufficiently small while providing high enough statistics to perform measurements at low $m_T - m_0$ where detector efficiencies are low (see discussion in Ch. 6) as well as at high $m_T - m_0$ where yields are low. Both rapidity and transverse mass are dependent on the particle mass and so different versions of each histogram must be created for each particle of interest with the correct mass assumption. In total, 35 3-dimensional histograms must be created for every observable: five particles (π^+, π^-, K^+, K^-, and p) each with seven centrality bins. Each of the three sets of multidimensional histograms described at the beginning of this section contains these 35 histograms, totaling 105 3-dimensional histograms.

Chapter 6

Detector Performance Corrections

For many reasons, the measured spectra are not the same as those generated by the collisions themselves and corrections accounting for known effects must be applied to give us our best guess at the true spectra, within statistical and systematic uncertainties. Corrections due to the limited detector acceptance and efficiency, in-medium energy loss, feed down, and knockout must be assessed for relevance and, in cases where determined to be significant, applied.

6.1 Energy-Loss Correction

As charged particles travel through matter, they lose energy due to ionization (the mechanism by which the TPC functions) or some other mechanism. However, as discussed in Ch. 2.2.1, the inner radius of the TPC is 50 cm away from the center of the beam pipe. Thus there is a region where we have no information about our particles. In this region, charged particles lose energy as they traverse the beam pipe, target, and the support structures of the detector. The vast majority of energy loss occurs in the beam pipe, but the target is included in the detector response model to properly reproduce the physical detector as best as possible. This changing energy translates into a constantly changing momentum, which must be corrected for. This correction is already built into the reconstruction software, which, for the purposes of energy loss, assumes that all tracks are a pion. The remaining task is then to correct the kaon and proton momenta properly. The

same embedding procedure used for acceptance and efficiency corrections can be used here, and the code which determines those corrections simultaneously determines the energy loss corrections. The energy loss correction must be the first one applied as it shifts the $m_T - m_0$ of each spectrum point, and subsequent corrections assume that the value of $m_T - m_0$ being used is already corrected for this effect. Naively, this correction should be largest for larger lab rapidities due to larger amounts of material traversed; however, this is a correction to the total momentum which is being applied to $m_T - m_0$. Due to the inherent relationship between total momentum and $m_T - m_0$, the low total momentum region gets compressed when looking at $m_T - m_0$ for more extreme lab rapidities, causing this correction to end up small for large rapidities and larger for small ones at low $m_T - m_0$.

For each rapidity bin and integrated centrality, the difference in embedded and reconstructed $m_T - m_0$ are evaluated and plotted for individual bins of the embedded $m_T - m_0$. Each of these 1D histograms represents the distribution of the shift of the embedded $m_T - m_0$ from the measured one and should be Gaussian. Each of these histograms is fit with a Gaussian, with the mean representing the average energy lost traveling through the detector material. For each rapidity, a graph of this mean (with the error on the mean being the uncertainty) as a function of the embedded $m_T - m_0$ is created. Each graph is initially fit with a power law function in p_T-space

$$p_T^{reco} - p_T^{\text{emb}} = A + B(p_T^{\text{reco}})^{-C}, \tag{6.1}$$

where p_T^{emb} is the input transverse momentum of the embedded track, p_T^{reco} is the reconstructed transverse momentum of the embedded track, and A, B, and C are fit parameters. In order to apply this correction to $m_T - m_0$ spectra, this function has been re-written in terms of m_T^{reco}

$$m_T^{\text{emb}} - m_T^{\text{reco}} = \sqrt{\left[\sqrt{x^2 + 2xm_0} - A - B\left(x^2 + 2xm_0\right)^{-C/2}\right]^2 + m_0^2} - (x + m_0) \tag{6.2}$$

where m_T^{emb} is the input transverse mass of the embedded track, m_T^{reco} is the reconstructed transverse mass of the embedded track, $x = m_T^{\text{reco}} - m_0$, m_0 is the mass of the particle being studied, and A, B, and C are the same fit parameters used in the p_T-space power law.

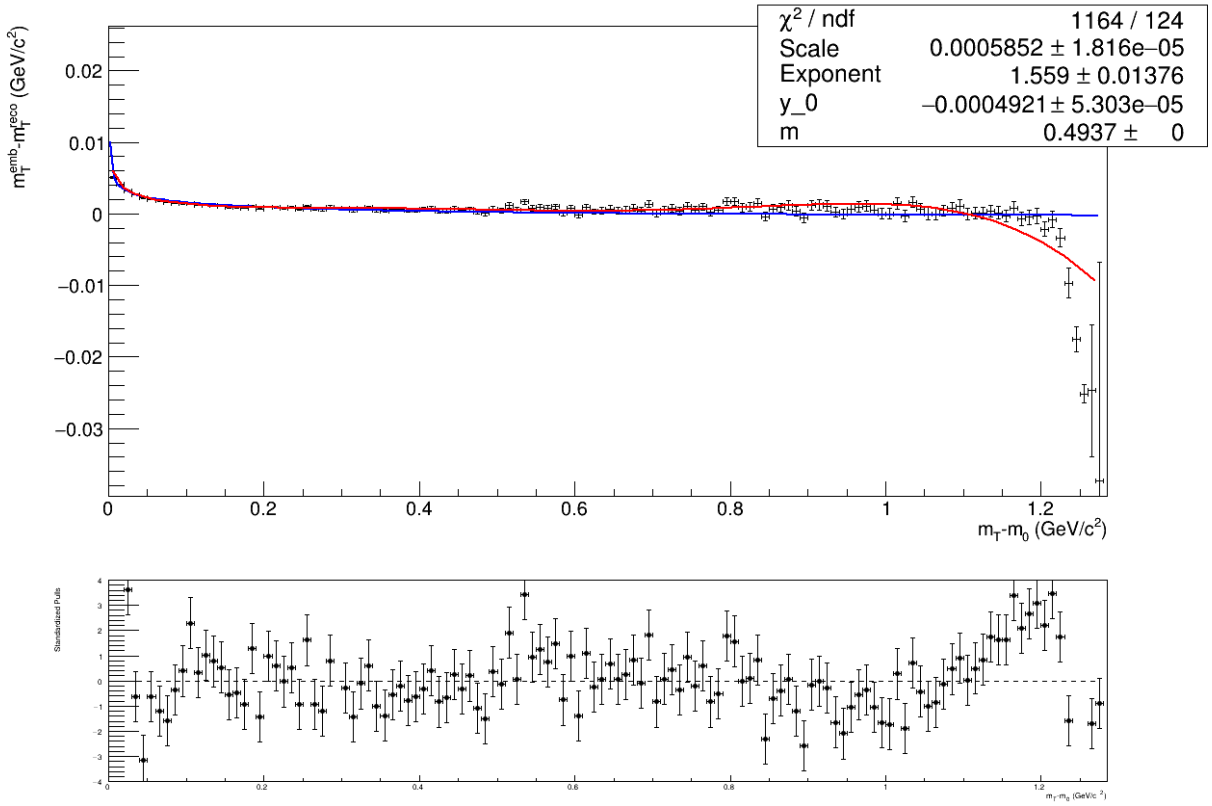

Figure 6.1: Means of embedded $m_T - m_0$ minus reconstructed $m_T - m_0$ for K^+ near target rapidity. The blue line represents the power law fit from Eq. 6.2 and the red line represents the sum of that with the Legendre Polynomial fit of the residuals.

The difference between the data and fit is taken and fit with a Legendre polynomial of 4th order to describe the deviations of the data from this simple fit function. The final fit is the sum of the m_T energy loss fit and the Legendre polynomial and can be seen in Fig. 6.1. This correction is the first one applied to the raw spectra as it adjusts the $m_T - m_0$ of each point and the corresponding invariant yield due to its $1/m_T$ dependence.

6.2 Detector Acceptance and Efficiency

The STAR Detector, while an excellent machine with great acceptance, is neither hermetic nor does it have 4π acceptance. While the TPC has close to 2π coverage in azimuth, gaps between sectors

and malfunctions in Front-End Electronics prevent full acceptance of all particles. Furthermore, in fixed-target mode, the pseudorapidity (η) acceptance is limited to $0 \leq \eta \leq 1.5$. The standard STAR practice has been to embed simulated tracks (approximately 5% of the event multiplicity) into real data and run that through a full GEANT simulation of the STAR detector to see its response. The result is then run through the full reconstruction chain, just like real data. For each centrality (determined by the data multiplicity without embedded tracks), in bins of $m_T - m_0$ and y (bins in y match those in the analysis while $m_T - m_0$ bins are narrower to provide more points for fitting), a ratio of the number of reconstructed tracks to the number of embedded tracks is constructed. This is done for each particle of interest. Once these ratios are constructed, 1D projections for each rapidity bin are made and the resulting distributions are fit as a function of $m_T - m_0$. To correct the raw spectra, a series of fits are made for each of these 1D projections in order to obtain the best overall determination of the efficiency. First, a linear function is fit to the high $m_T - m_0$ region (for pions, kaons, and protons, this is done above an $m_T - m_0 = 1.0$, 0.8, and 1.0 GeV respectively). In the low $m_T - m_0$ region, an initial fit is done for each rapidity bin with the form

$$\epsilon(m_T - m_0) = Ae^{-b/(m_T - m_0)^c}. \tag{6.3}$$

This is a standard function used in the STAR Collaboration for fitting the efficiencies, where A, b, and c are fit parameters; however, significant deviations between the data and this fit function are observed so additional fitting is required. The functional form in Eq. 6.3 is used to determine systematic uncertainties. Next, a graph of the residuals of this systematic fit is constructed and further fit by a fourth order Legendre Polynomial. The final efficiency is the sum of the systematic fit and the Legendre Polynomial fit, up to the $m_T - m_0$ of the linear fit, at which point the linear fit is used. Examples of each of these fits can be seen for π^+ at midrapidity in 0-5% central collisions in Figs. 6.2, 6.3, and 6.4. To apply the efficiency correction to the raw spectra, the combined final fit function is evaluated at the center of the $m_T - m_0$ bin of each spectral point and the raw yield is divided by the efficiency to obtain the corrected yield.

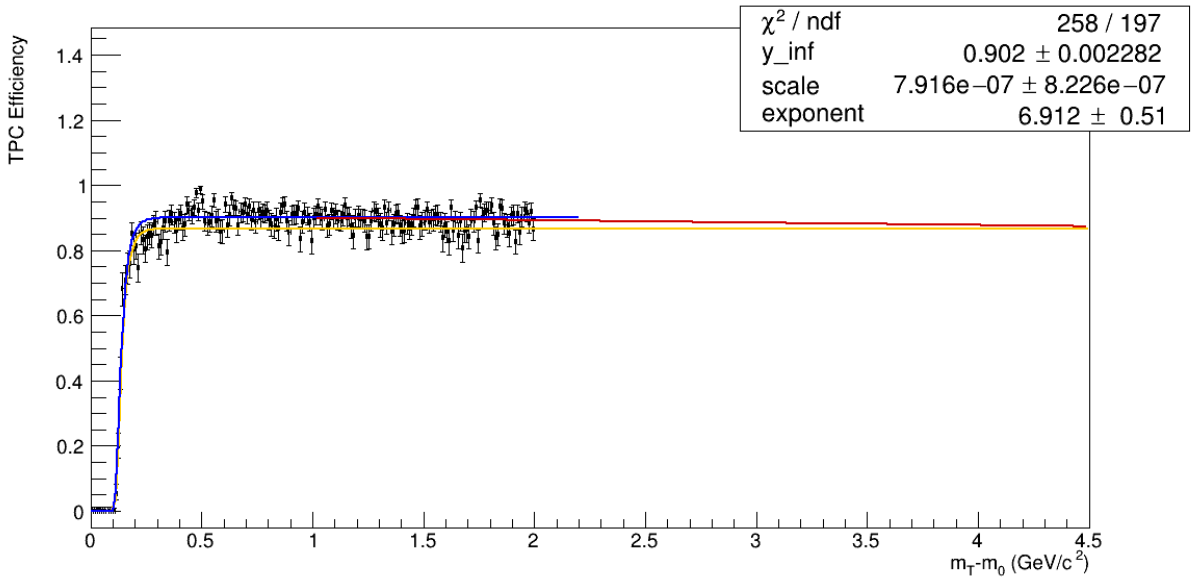

Figure 6.2: Initial fit of midrapidity π^+ efficiency for 0-5% Central collisions with systematic function (Eq. 6.3, where y_inf = A, scale = b, and exponent = c) in blue and a linear fit in red at high $m_T - m_0$. The yellow line represents the systematic function before fitting with its initial seeds and allows improved tuning of the parameter seeds.

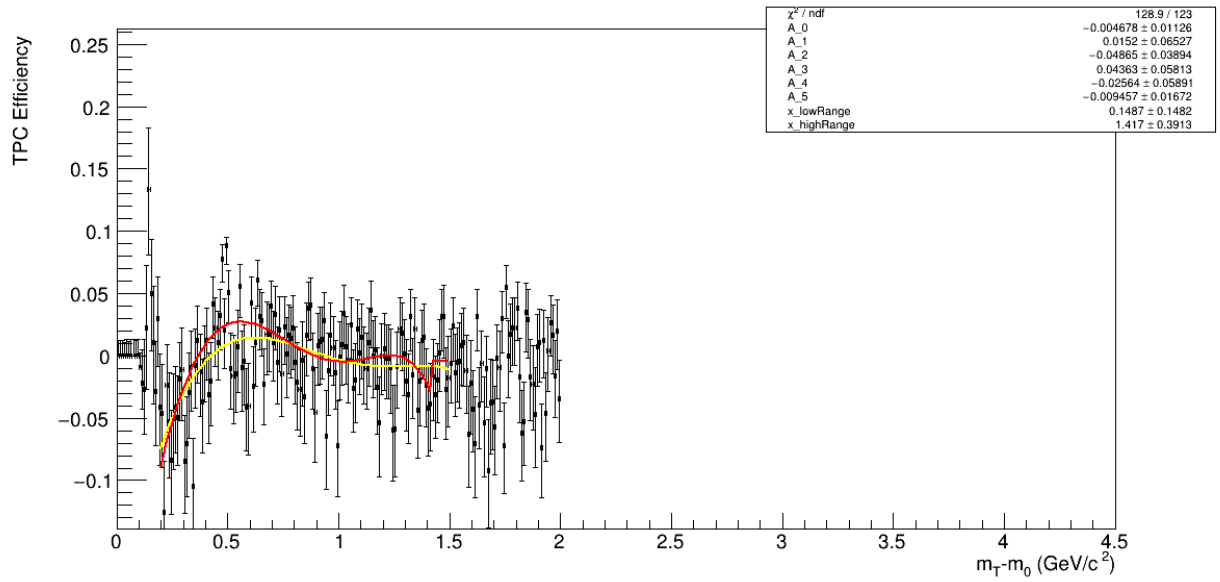

Figure 6.3: Residuals of the midrapidity π^+ efficiency from the systematic fit function for 0-5% Central collisions. The red line is the 4th order Legendre Polynomial fit to these residuals and the yellow line is the same function but with its initial parameter seed values.

6.3 Feed-Down Correction

Even for the low energy collisions in this analysis, strange baryons are created in the collision. When these strange baryons decay, they very often decay into a proton and/or pions. These protons and pions are not from the original collision and so they must be corrected for in the analysis.

One million UrQMD events in a fixed-target geometry at $\sqrt{s_{NN}} = 3.0$ GeV were generated and run the a full GEANT simulation of the STAR detector, followed by the full reconstruction chain, similar to the embedding. This reconstruction chain generates a number of different files in different STAR formats which include the embedded and reconstructed data; the file format used in this analysis is called the "minimc" file and contains just the information about the embedded and reconstructed tracks along with a matching between them. From the "minimc" files, all reconstructed particles were looped over and any which were a proton or charged pion (each particle and charge is handled individually) had their parent ID put into a histogram. The parent ID indicates the source

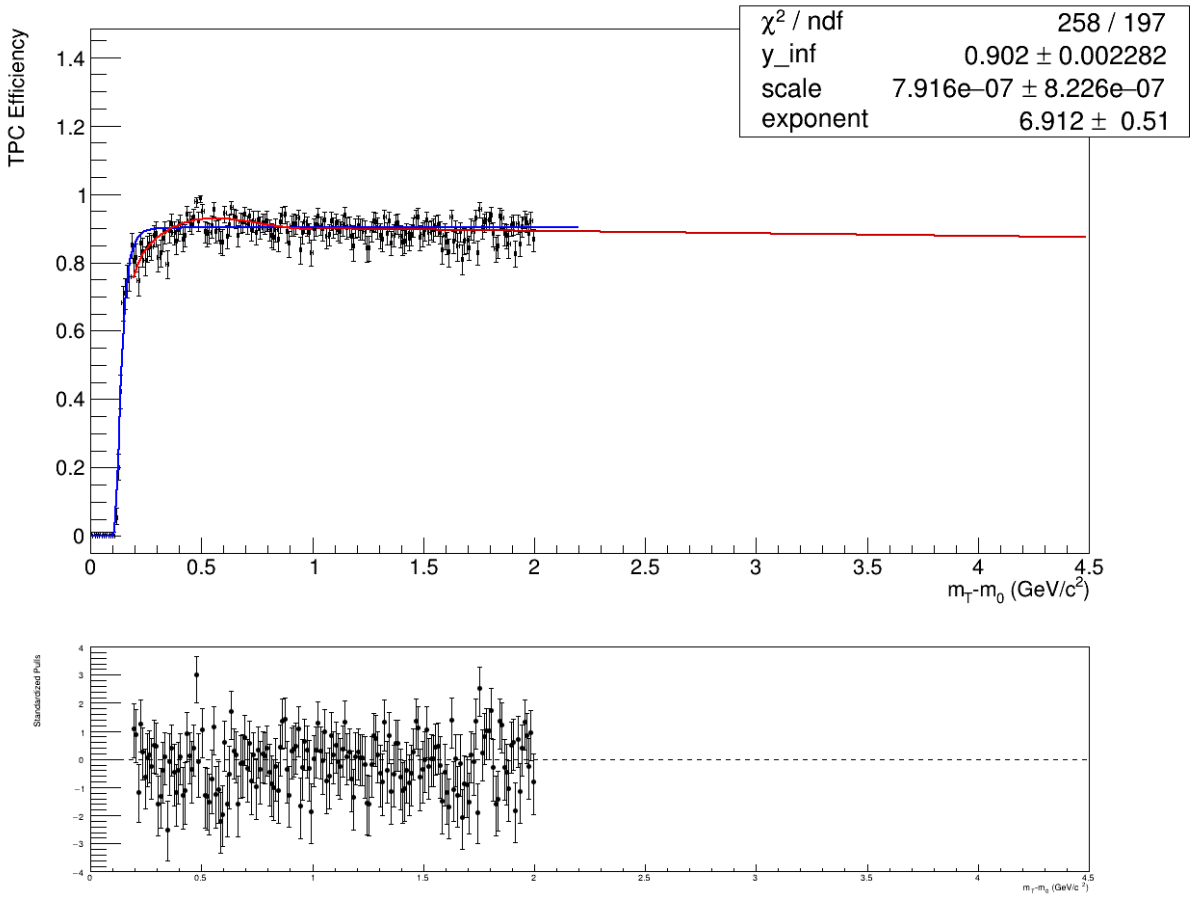

Figure 6.4: Final fit of midrapidity π^+ efficiency for 0-5% Central collisions. The blue line is the systematic fit function, which is identical to the blue line in Fig. 6.2. The red line is the sum of the systematic fit function and the Legendre Polynomial fit of the residual up to an $m_T - m_0$ of 1.0 GeV, after which a linear function takes over.

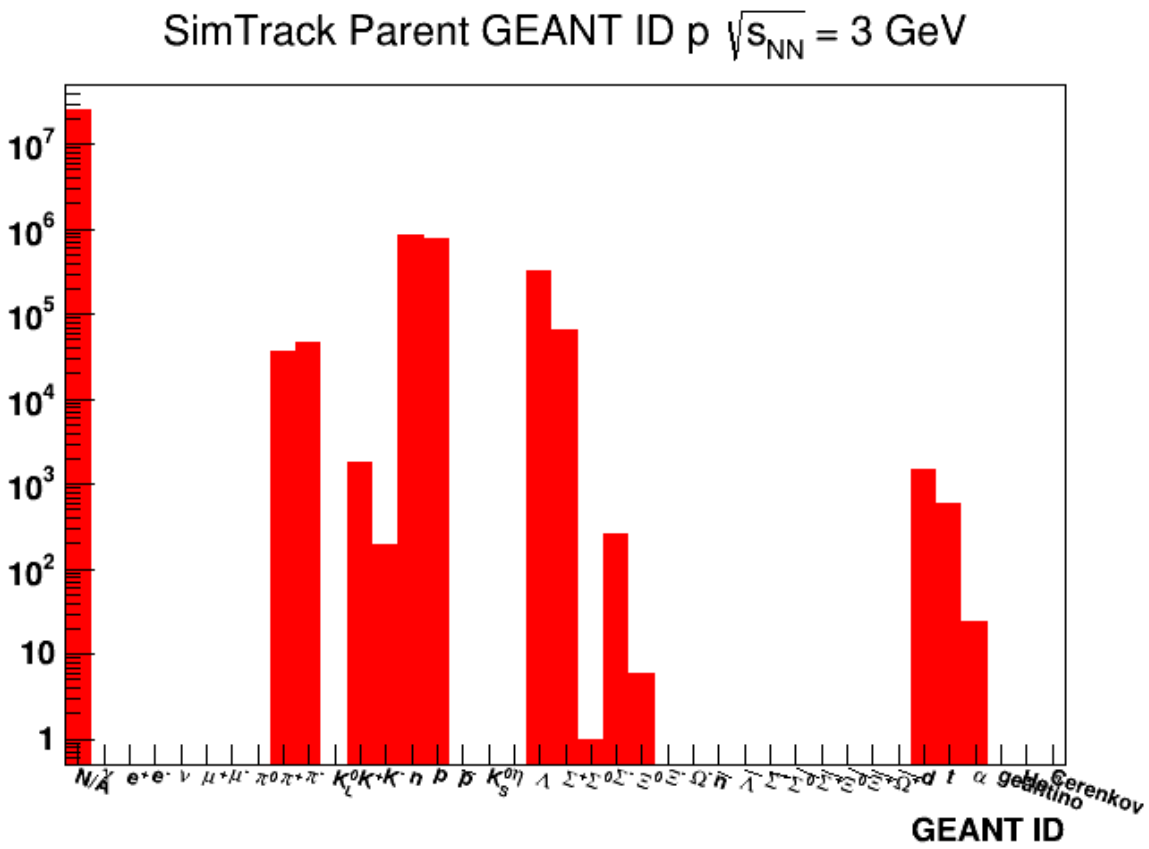

Figure 6.5: Simulated parent ID for protons reconstructed from UrQMD events run through a full GEANT simulation of the STAR detector.

of the proton or pion, where N/A indicates that the track originated from the primary collision itself and any other parent is either due to a decay (e.g. $\Lambda \to p + \pi^-$) or interaction with detector material (e.g. $p + n \to p + p + \pi^-$). Figure 6.5 shows the parent ID of protons, the majority which come from the collision itself, but there are a number which come from charged pions, charged kaons, nucleons, light nuclei, or strange baryons. Protons originating from strange baryons are predominately due to weak decay, and are the current topic of discussion. The remaining protons which did not originate in the collision are all considered knockout protons, the correction for which is discussed in the following section. When considering pions, all pions not originating from the original collision are considered due to weak decays and must be corrected for.

In order to correct for feed-down protons, in each centrality bin and for each $m_T - m_0$ and y

bin, a ratio is constructed where the numerator is the number of protons from feed-down sources (e.g. strange baryons) and the denominator is the number of protons from feed-down sources AND protons from the collision. The same ratio is also constructed using pions in place of protons. For each rapidity bin, this ratio is fit as a function of $m_T - m_0$. The maximum of this ratio, and therefore the maximum of the contamination due to feed-down protons or pions, is below 2%. To apply the correction, each spectra point in each centrality and y bin is multiplied by $1 - R$ for the corresponding bins from the simulation, where R is the fit of the ratio evaluated at the $m_T - m_0$ of the corresponding spectral point. It has been determined that such a correction is not necessary due to the low feed-down fraction, and so such a correction has not been applied.

6.4 Knockout Correction

Since the STAR detector and the beam-pipe are constructed with atomic matter, there is an abundance of protons (and neutrons) in the material surrounding the collision. STAR has been constructed to minimize the amount of material between the interaction point and the TPC, but it is impossible to remove all material. Any time a charged particle passes through material, there is a chance that it will knock out a proton (this predominately happens in the beam pipe). In the fixed-target data sets, produced particles can also interact with the gold target itself and cause an additional source of knockout protons. These protons are generally only a few centimeters from the collision itself and many times are incorrectly identified as primary (having been created in the collision itself). Since these protons are measured due to secondary interactions with detector material, we would like to remove them from the proton spectra. At higher energies where p and $\bar{p}$ are produced relatively equally or at least proportionally, the difference between protons and (scaled) antiprotons provides a data-driven method of determining the fraction of knockout protons. At this energy, without sufficient numbers of $\bar{p}$, we must turn to simulation to determine the knockout proton correction.

The knockout proton correction is determined simultaneously with the feed-down correction

discussed in the previous section and utilized the same one million UrQMD events and reconstruction procedure. The parent IDs of protons fron this UrQMD sample can be seen in Fig. 6.5. As was previously discussed, protons whose parent ID is N/A originate from the collision while those whose parent was a strange baryon are mostly due to feed-down. The protons originating from the remaining parents are all considered knockout protons.

In order to correct for knockout protons, in each centrality bin and for each $m_T - m_0$ and y bin, a ratio is constructed where the numerator is the number of protons from knockout sources (pions, kaons, nucleons, and light nuclei) and the denominator is the number of protons from knockout sources AND protons from the collision is constructed. For each rapidity bin, this ratio is fit as a function of $m_T - m_0$. The maximum of this ratio, and therefore the maximum of the contamination due to knockout protons, is below 2%. To apply the correction, each spectra point in each centrality and y bin is multiplied by $1 - R$ for the corresponding bins from the simulation, where R is the fit of the ratio evaluated at the $m_T - m_0$ of the corresponding spectral point. Like, the feed-down study, it has been determined that such a correction is not necessary due to the low knockout proton fraction, and so such a correction has not been applied.

Chapter 7

Invariant Yield Extraction

The core of the analysis at hand is to obtain the yields of π^+, π^-, K^+, K^-, and p. In order to extract raw yields there are three main steps: integrated centrality fits, individual centrality fits, and anomalous fitting, each with their own parts. Regardless of which centrality step is underway, each 3-dimensional histogram described in Ch. 5 has one-dimensional projections made onto the z-axis (corresponding to either m^2 or Z_{TPC}) for each individual bin in rapidity and transverse mass. These one-dimensional distributions are then fit with one or more normalized Gaussian distributions to fit the peaks representing the particle of interest while accounting for contamination from other species. When fitting the distributions binned based on the mass of a pion, the goal is to extract the pion yield, so the pion would be considered the particle of interest. Moving forward, particle of interest (PoI) will be used exclusively to refer the particle whose mass was used for binning, while any other language regarding particles will refer to contaminating particles being fit within that binning. For each particle of interest, different hadrons contribute to contamination and are fit. Table 7.1 shows which hadrons are fit for each particle of interest. Examples of the fits for each step will be shown for extracting the π^+ yield (π^+ is the PoI) at $y_{\mathrm{lab}} = -1.05$ and $m_T - m_0 = 0.375$ MeV.

Particle of Interest	Particles to Fit
π^+	π^+, K^+, p, and d
K^+	π^+, K^+, and p
p	π^+, K^+, p, and d
π^-	π^- and K^-
K^-	π^- and K^-

Table 7.1: Particles to be fit for each particle of interest.

7.1 Integrated Centrality Fitting

The high statistics of integrated centrality data sets provide an unparalleled ability to perform Gaussian fits to the particle peaks in order to determine the mean, μ, and standard deviation, σ. Integrated centrality histograms of m^2, TOF-identified Z_{TPC}, and Z_{TPC} are constructed by adding the distributions from the seven centrality bins together. The first step is to fit the m^2 distributions, then the TOF identified Z_{TPC} distributions, followed by the Z_{TPC} distribution.

7.1.1 m^2 Fitting

The quantity m^2 is obtained from the TOF and incorporates the track momentum which helps to improve effects due to the momentum bin width resolution. m^2 is defined by Eq. 7.1:

$$m^2 = p^2 \left(\frac{1}{\beta^2} - 1 \right). \tag{7.1}$$

For each PoI, one-dimensional projections are made for each rapidity and transverse mass bin from the corresponding histogram. Each of these projections zooms in on a region around the known mass of each particle (both the particle of interest along with contaminating particle species) and is fit with a normalized Gaussian distribution. In the case of Kaons, an additional background function (double exponential, $Ae^{be^{-cx}}$) is required as the yield is low and would be significantly influenced by the background otherwise; such a procedure is not required for other particles as their yields are sufficiently high compared to the background, which contributes less than 1% to their yields. For each PoI, the three Gaussian parameters are stored separately for each particle in each rapidity and

transverse mass bin. In cases where statistics are too low, such as at low $m_T - m_0$ or at the edges of acceptance, these fits are not performed and the stored parameters are set to zero. An example of these fits for pions and kaons are in Fig 7.1.

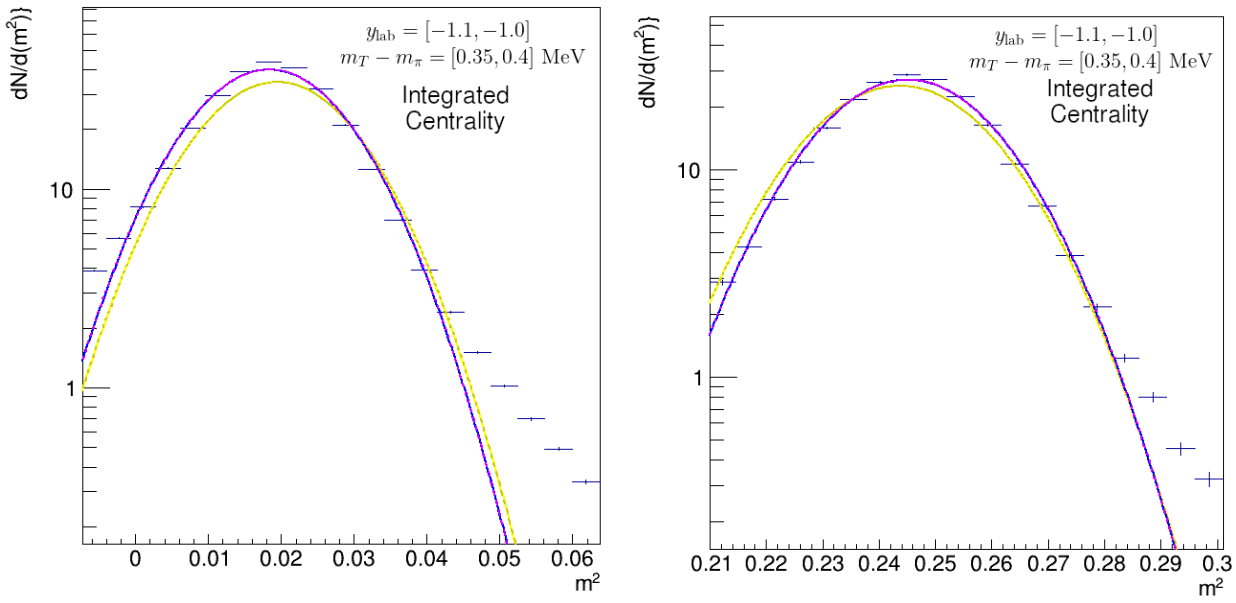

Figure 7.1: Integrated centrality fits of m^2 for π^+ (left) and K^+ (right) in a single rapidity bin. Both are Gaussian distributions, with the magenta curve representing the fit result and the yellow curve using the parameter seeds. Tails in data not described by the Gaussians originate from mis-match of a track to a TOF hit, causing an incorrect m^2.

7.1.2 TOF-Identified Z_{TPC} Fitting

The quantity Z_{TPC} is intended to make dE/dx more Gaussian as well as recenter the dE/dx distribution around the Bichsel prediction of the PoI,

$$Z_{\text{TPC}} = ln\left[\frac{(dE/dx)_{\text{measured}}}{(dE/dx)_{\text{Bichsel,PoI}}}\right], \tag{7.2}$$

where $(dE/dx)_{\text{Bichsel,PoI}}$ is the Bichsel prediction for the PoI at the total momentum of the bin. The logarithm of dE/dx is much more Gaussian in shape than dE/dx itself, which makes extracting the yield in each rapidity and transverse mass bin much easier. If the Bichsel curves are tuned

properly, the PoI should have a peak at $Z_{\mathrm{TPC}} = 0$ and contaminating particle peaks should be at their Bichsel prediction; unfortunately, that is quite often not the case which means the Gaussian mean, μ, must be obtained by fitting. In order to remove as much contamination from other particles as possible, TOF-identified Z_{TPC} distributions are constructed. For each PoI, separate histograms are constructed for each particle requiring that the m^2 be within a set range of the known mass of the particle. This generates Z_{TPC} histograms where the vast majority of tracks are truly that particle (though binned by the PoI mass assumption) and allows precise determination of the Z_{TPC} Gaussian mean and standard deviation for each particle for every PoI. The downside to this method is that it requires TOF information which has a lower efficiency and therefore lower statistics, which is why this step is done for integrated centrality. For each particle of interest and each contaminating particle, one-dimensional projections are made for each rapidity and transverse mass bin and one Gaussian is fit to each projection. For each PoI, the Gaussian mean and standard deviation are stored separately for each particle in each rapidity and transverse mass bin. In cases where statistics are too low, such as at low $m_T - m_0$ or at the edges of the acceptance, these fits are not performed and the stored parameters are set to zero. An example of these fits for pions and kaons are in Fig 7.2.

7.1.3 Z_{TPC} Fitting

As before, for each PoI, one-dimensional projections are made for each rapidity and transverse mass bin. Multiple normalized Gaussian distributions are fit to each projection based on which particles are being fit, as indicated in Tab. 7.1. In cases where the TOF-identified Z_{TPC} fit for the PoI, particle to fit, rapidity, and transverse mass bin were performed and successful (the standard deviation is not set to zero), the mean and standard deviation are fixed for the corresponding particle. In cases where those fits were not performed or failed, standard deviation is seeded to 0.06 (the limit of TPC dE/dx resolution) and the mean is seeded to the Bichsel prediction,

$$Z_{\mathrm{TPC}}(X) = ln\left[\frac{(dE/dx)_{\mathrm{Bichsel,X}}}{(dE/dx)_{\mathrm{Bichsel,PoI}}},\right] \tag{7.3}$$

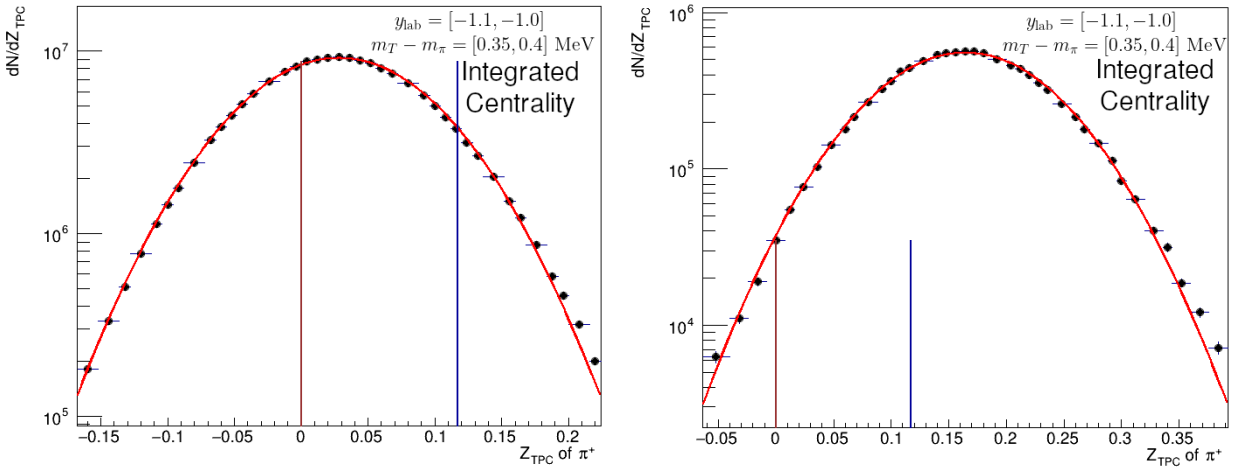

Figure 7.2: Integrated centrality fits in a single rapidity bin of TOF-Identified Z_{TPC}, used to extract Gaussian parameters to ultimately obtain the pion yield. π^+ (left) is used to obtain the pion yield and K^+ (right) is used to account for contamination, both use the pion as the PoI but different m^2 cuts to select the contribution from each particle. Both are Gaussian distributions. The vertical brown and blue lines each represent the predictions of Z_{TPC} based on the Bichsel curves for pions and kaons respectively.

where $(dE/dx)_{\text{Bichsel,X}}$ and $(dE/dx)_{\text{Bichsel,PoI}}$ are the Bichsel curve values for particle X and the PoI respectively at the total momentum of the bin. In many cases, particle bands from dE/dx merge together and make various species indistinguishable from each other (e.g. π and K merge at $p_{\text{total}} = 0.8$ GeV while π and p merge at $p_{\text{total}} = 1.6$ GeV). The standard STAR analysis method is to switch to using TOF data at those momenta, but such a method is not adopted by the author. The use of only TOF data at higher momenta requires a larger correction due to the lower efficiencies, therefore increasing the uncertainty in the measurement. Instead, the author developed a new method called the relative amplitude method to better fit the data using TOF information, but without the need for an additional efficiency correction.

The relative amplitude method addresses the problem of particle bands merging by applying constraints to the particle amplitudes using TOF information from the m^2 fits. When particles merge, we call the particle with the higher yield the major particle while the one with the smaller yield is the minor particle. These pairings along with total momentum thresholds are shown in Tab. 7.2. The amplitude of the minor particle in Z_{TPC} is set to the amplitude of the major particle in

Z_{TPC} multiplied by the fixed ratio of the amplitudes in the corresponding rapidity and transverse mass bins in the TOF. The amplitude of the minor particle is

$$A_{\mathrm{min,TPC}} = A_{\mathrm{maj,TPC}} \frac{A_{\mathrm{min,TOF}}}{A_{\mathrm{maj,TOF}}}, \tag{7.4}$$

where $A_{\mathrm{min,TPC}}$ is the final amplitude of the minor particle in the Z_{TPC} fit, $A_{\mathrm{maj,TPC}}$ is the final amplitude of the major particle in the Z_{TPC} fit, $A_{\mathrm{min,TOF}}$ is the TOF amplitude of the minor particle, and $A_{\mathrm{maj,TOF}}$ is the TOF amplitude of the major particle. To add clarity, an example of a fit function with two normalized Gaussians is

$$N = \frac{A_{\mathrm{maj,TPC}}}{\sigma_{\mathrm{min}}\sqrt{2\pi}} \frac{A_{\mathrm{min,TOF}}}{A_{\mathrm{maj,TOF}}} e^{-\frac{1}{2}\left(\frac{x-\mu_{\mathrm{min}}}{\sigma_{\mathrm{min}}}\right)^2} + \frac{A_{\mathrm{maj,TPC}}}{\sigma_{\mathrm{maj}}\sqrt{2\pi}} e^{-\frac{1}{2}\left(\frac{x-\mu_{\mathrm{maj}}}{\sigma_{\mathrm{maj}}}\right)^2}, \tag{7.5}$$

where $A_{\mathrm{maj,TPC}}$ is a free parameter for the major particle yield, $A_{\mathrm{min,TOF}}$ and $A_{\mathrm{maj,TOF}}$ are the fixed amplitude parameters from the m^2 fit in the corresponding bin for the minor and major particles respectively, μ_{min} and σ_{min} are the fixed Gaussian mean and width for the minor particle from the TOF-identified Z_{TPC} fit, and μ_{maj} and σ_{maj} are the fixed Gaussian mean and width for the major particle from the TOF-identified Z_{TPC} fit. In the case of Eq. 7.5, the only free parameter is $A_{\mathrm{maj,TPC}}$ as all others have been fixed by either the m^2 fits or the TOF-identified Z_{TPC} fits. Other cases of the relative amplitude method may add a normalized Gaussian with its own free amplitude or an additional normalized Gaussian with this relative amplitude applied as well, as can happen when fitting positively charged particles above certain total momentum thresholds.

The assumption in this method is that the TOF efficiency is the same for π and p, whereas $K^{\pm}$ decay and require a minor correction. This K decay correction is implemented directly in the construction of these amplitude ratios and uses the mean lifetime of the K and the distance traveled between the outer radius of the TPC and the inner radius of the TOF to calculate the percentage of K which remain and should hit the TOF. Removing the necessity for a TOF efficiency is an important feature of this method as there tends to be more uncertainty in this efficiency compared to the TPC tracking efficiency, and the efficiency is less well defined for fixed-target collisions in certain

regions of the detector due to the physical design of the TOF system. This method is only used when the Bichsel predictions (Eq. 7.3) of two particles that merge are within 0.25 of each other in Z_{TPC} space. This threshold was empirically determined and maximizes the momentum range where overlapping peaks from two particles can be fit and both be be well characterized. This relative amplitude method requires successful fits of both the minor particle and the major particle in the corresponding m^2 and TOF-identified Z_{TPC} bins in order to have TOF amplitudes to use as well as Gaussian means and standard deviations, which are degenerate otherwise. Comparisons between this relative amplitude method and the standard STAR method have been performed and indicate very good agreement between the two methods, with reduced uncertainty in the high momentum region where TOF data are necessary due to the use of only one efficiency correction with the relative amplitude method compared to two required in the standard method.

Minor Particle	Major Particle
π^+	p ($p_{\mathrm{total}} > 1.16$ GeV)
K^+	π^+ ($1.16 > p_{\mathrm{total}} > 0.6$ GeV) p ($p_{\mathrm{total}} > 1.16$ GeV)
p	none
d	p ($p_{\mathrm{total}} > 2.4$ GeV)
π^-	none
K^-	π^- ($p_{\mathrm{total}} > 0.6$ GeV)

Table 7.2: Pairings for the relative amplitude method for the minor particle and major particle along with corresponding total momentum range.

With this relative amplitude method, normalized Gaussians are fit to the one-dimensional projections of Z_{TPC}. For each PoI, the Gaussian mean and standard deviation are stored separately for each particle in each rapidity and transverse mass bin. In cases where statistics are too low, such as at low $m_T - m_0$ or at the edges of the acceptance, these fits are not performed and the stored parameters are set to zero. An example of such a fit is in Fig 7.3.

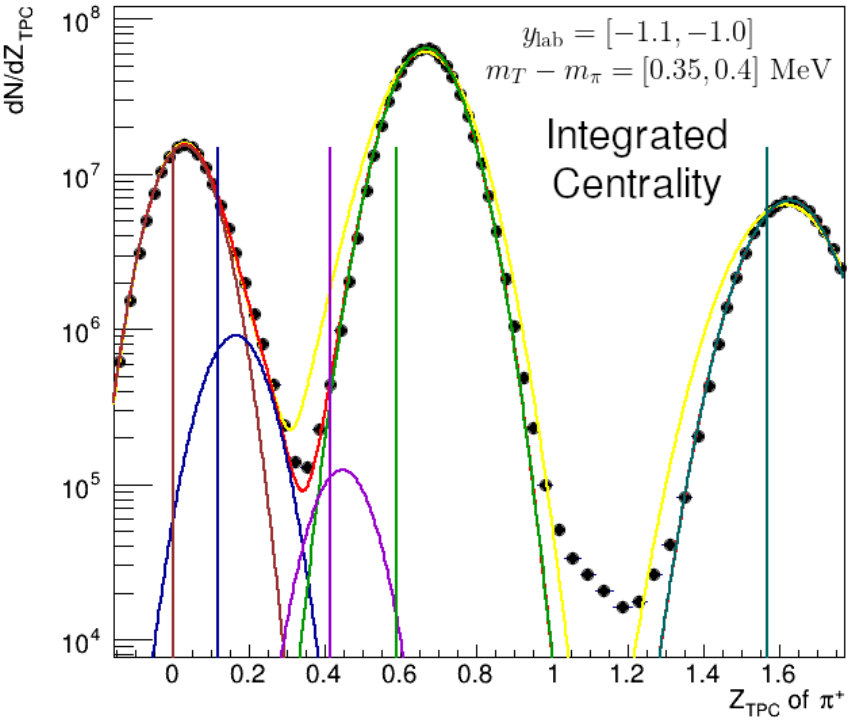

Figure 7.3: Integrated centrality fits of Z_{TPC} in a single rapidity bin. In this fit, the kaons are fully constrained by the relative amplitude method. The brown, blue, magenta, green, and teal curves are the Gaussians representing the pions, kaons, electrons, protons, and deuterons respectively. The vertical lines each represent the predictions of Z_{TPC} based on the Bichsel curves each particle. The red curve is the sum of all particle Gaussians and the yellow curve is the parameter seeds

7.2 Individual Centrality Fitting

The integrated centrality fits provide the means and standard deviations for the normalized Gaussians, so the task is to now repeat the fits in each centrality bin to obtain the yields with the means and standard deviations fixed. This assumes that the dE/dx calibration and resolution are centrality independent, which is not inherently true as a higher occupancy in the TPC causes space points to overlap, causing clusters to be less well defined; however, occupancy issues are not as significant in fixed-target collisions compared to collider ones and fits without the means fixed resulted in similar values for the mean (within 5%). The first step is to redo the m^2 fits to obtain the TOF yields for use with the relative amplitude method. For each PoI, the Gaussian yield is stored separately for

each particle in each rapidity and transverse mass bin. In cases where statistics are too low, such as at low $m_T - m_0$ or at the edges of acceptance, these fits are not performed and the stored parameters are set to zero. Next, the Z_{TPC} fits are performed similarly to the integrated centrality fits except with the Gaussian means and standard deviations now fixed: if the known means of two particles are within 0.25 of each other, the relative amplitude method is applied using the individual TOF yields to obtain the yields of those particles, in other cases the amplitude is left as a free parameter. For each PoI, the Gaussian yield is stored separately for each particle in each rapidity and transverse mass bin. In cases where statistics are too low, such as at low $m_T - m_0$ or at the edges of acceptance, these fits are not performed and the stored parameters are set to zero. Individual centrality fitting provides quite similar results as integrated centrality fitting, just with lower yields, so an example of only the final fit from which the yields are extracted is shown in Fig 7.4.

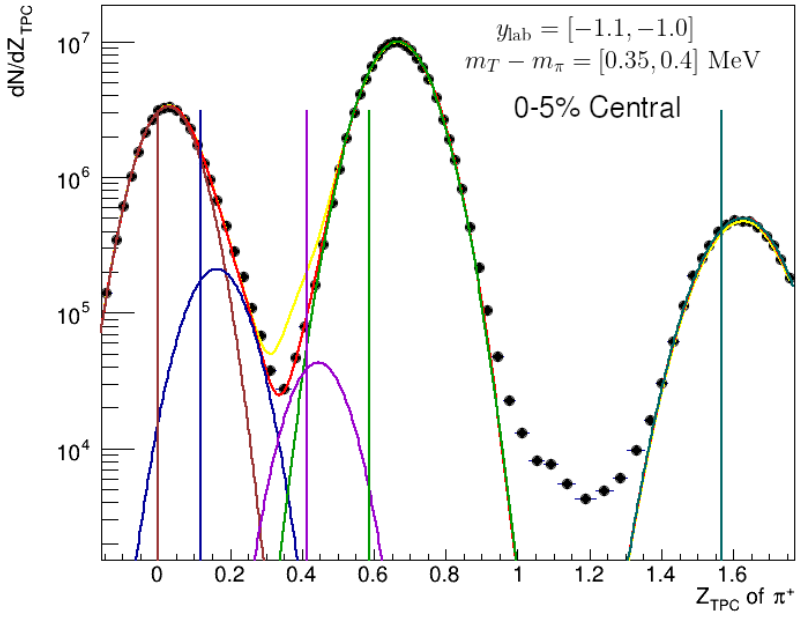

Figure 7.4: 0-5% centrality fit of $\mathrm{Z_{TPC}}$ in a single rapidity and $m_T - m_\pi$ bin. In this fit, the kaons are fully constrained by the relative amplitude method. The brown, blue, magenta, green, and teal curves are the Gaussians representing the pions, kaons, electrons, protons, and deuterons respectively. The vertical lines each represent the predictions of $\mathrm{Z_{TPC}}$ based on the Bichsel curves of each particle. The red curve is the sum of all particle Gaussians and the yellow curve is the parameter seeds

7.3 Anomalous Fitting

In some cases, the automated method implemented in the code was not able to perform good fits of the data, even though it is clearly possible. Most cases of failed fits are due to poor seeds in the integrated centrality fits, poor constraints which cause the parameters to get stuck in a local minimum, or low statistics. Each rapidity, transverse mass, and centrality fit is inspected for each particle of interest to identify if it succeeded or failed, and those that failed are added to a list. Each failed fit on this list was refit manually without the use of the complex code package. In some cases, the relative amplitude method is also applied by hand, requiring multiple fits as previously described. An example of one of these fits of m^2 for K^+ in the 20-30% centrality bin is shown in Fig 7.5

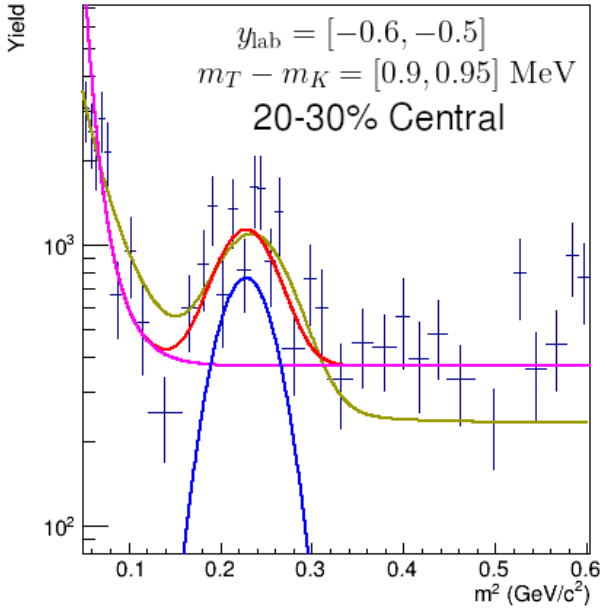

Figure 7.5: Anomalous fit of m^2 of K^+ in this bin required manual refitting. Large background contributions were not properly fit by the full algorithm, but were possible with manual fitting. The magenta curve is the double exponential background fit, the blue curve is the Gaussian fit of the kaon peak, and the red curve is the total fit, which is the sum of those two. The background is due to mismatches between tracks and TOF hits and is particularly important to characterize for kaons due to their low yields, the double exponential used to fit this background was empirically derived to appear exponential on a logarithmic vertical axis. The yellow curve shows the quality of the seeds of the fit parameters.

7.4 Invariant Spectra

All of the normalized Gaussian fits discussed above provide the multiplicity of the particle of interest (N) in each rapidity, transverse mass, and centrality bin. With these, the invariant spectra must be created. The invariant yield is

$$\frac{1}{N_{\mathrm{Evt}}}\frac{1}{2\pi m_T}\frac{d^2N}{dm_T dy}, \tag{7.6}$$

where N is the Gaussian yield from the individual Z_{TPC} centrality fits, N_{Evt} is the number of events in the centrality bin, m_T is the value at the center of the corresponding transverse mass bin, dm_T is the width of the transverse mass bin (0.05 GeV/c^2), and dy is the width of the rapidity bin (0.1). For each PoI, centrality, rapidity, and transverse mass bin, the Gaussian yield is multiplied by the corresponding factors to construct the invariant spectra. As described in Ch. 6, in order to correct for limited detector acceptance and efficiency, each of these raw invariant yields is divided by the efficiency for the corresponding PoI, centrality, rapidity, and transverse mass bin to obtain the invariant yields. Other corrections for feed-down due to weak decay of strange hadrons or the knockout of protons from detector material were determined unnecessary and were not used in this analysis, as discussed in sections 6.3 and 6.4. Figures 7.6, 7.7, 7.8, 7.9, and 7.10 show the corrected invariant yields (Eq. 7.6) of π^+, π^-, K^+, K^-, and p respectively.

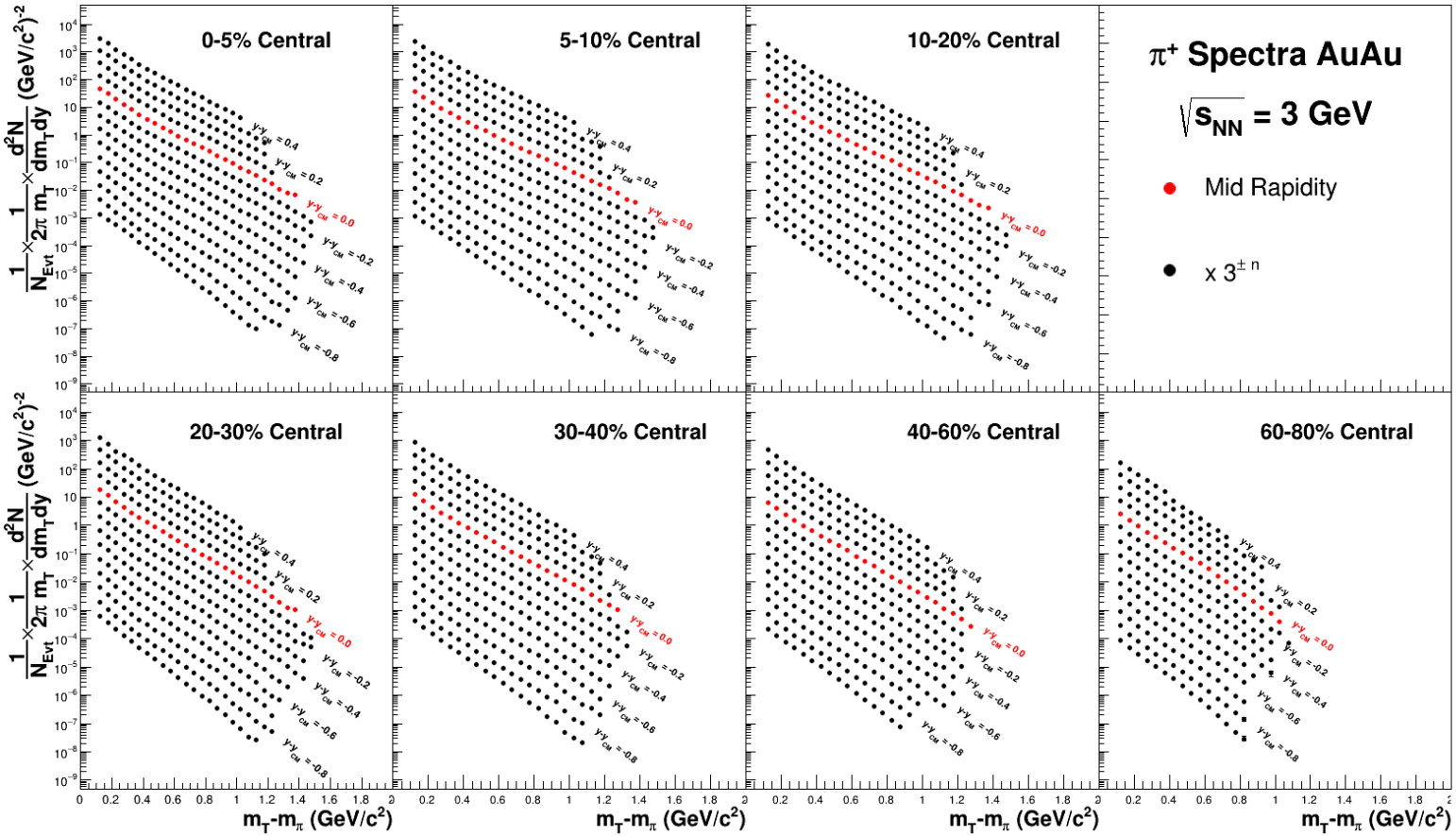

Figure 7.6: Invariant yield of π^+ at $\sqrt{s_{NN}} = 3.0$ GeV

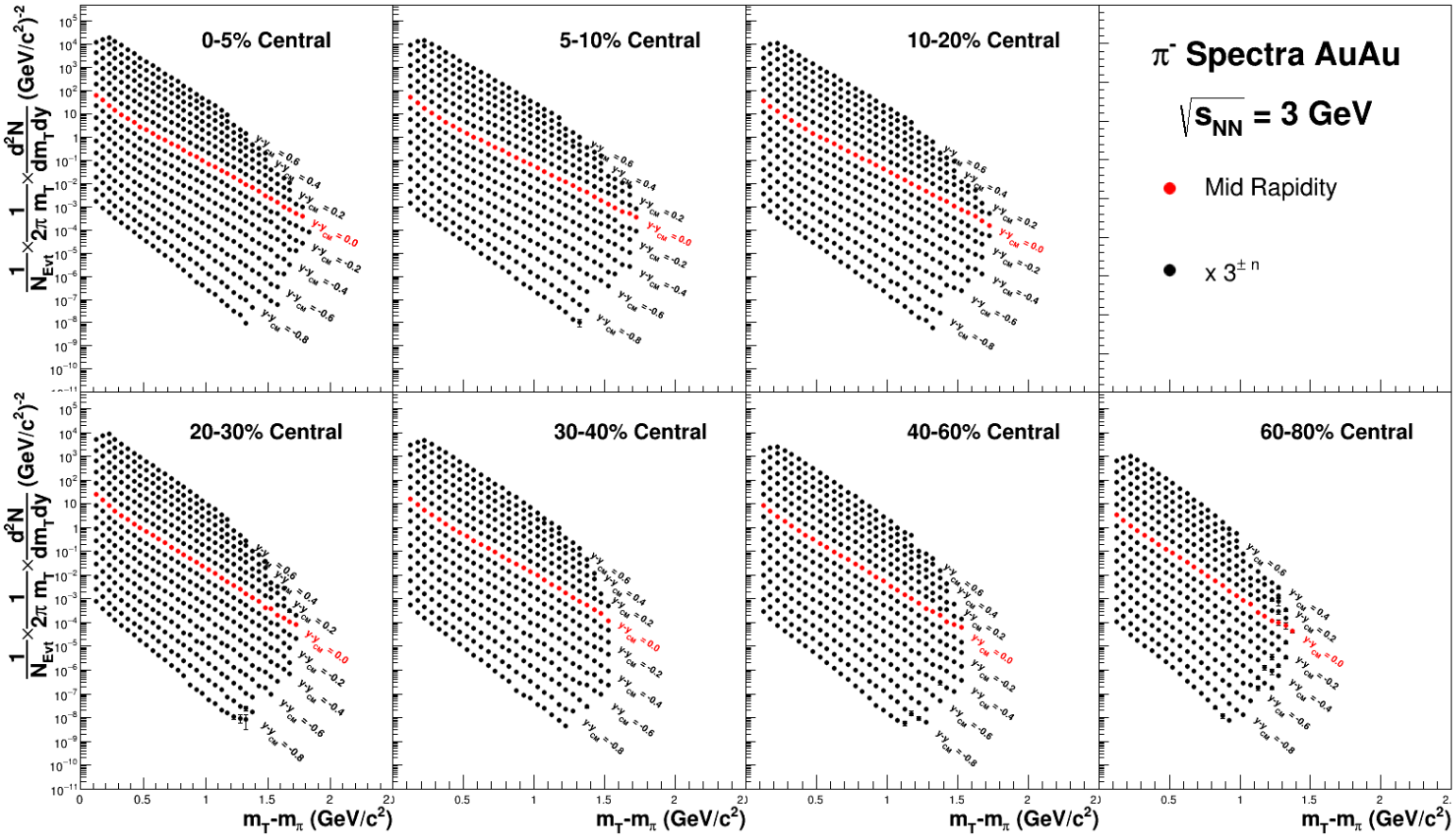

Figure 7.7: Invariant yield of π^- at $\sqrt{s_{NN}} = 3.0$ GeV

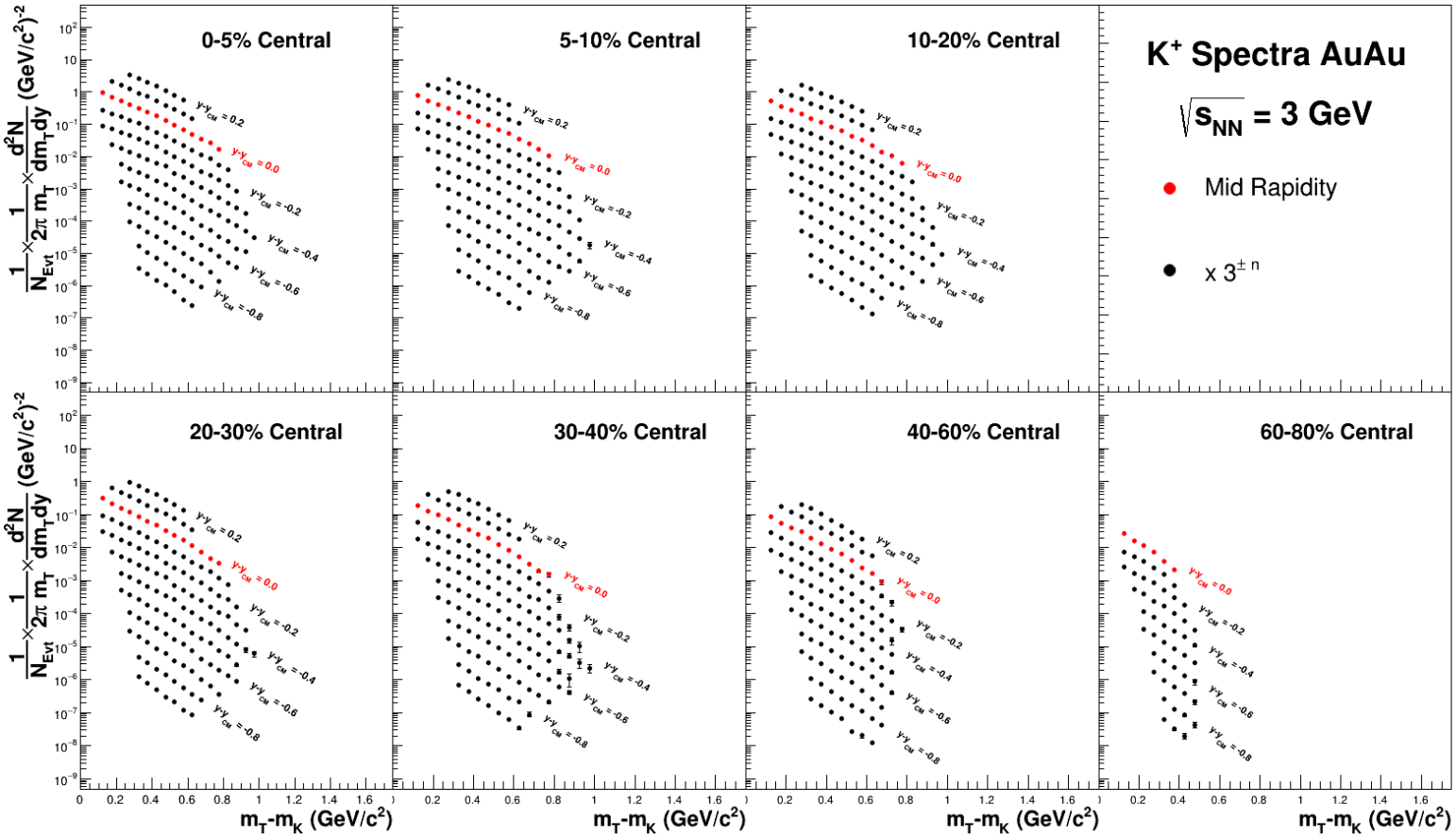

Figure 7.8: Invariant yield of K^+ at $\sqrt{s_{NN}} = 3.0$ GeV

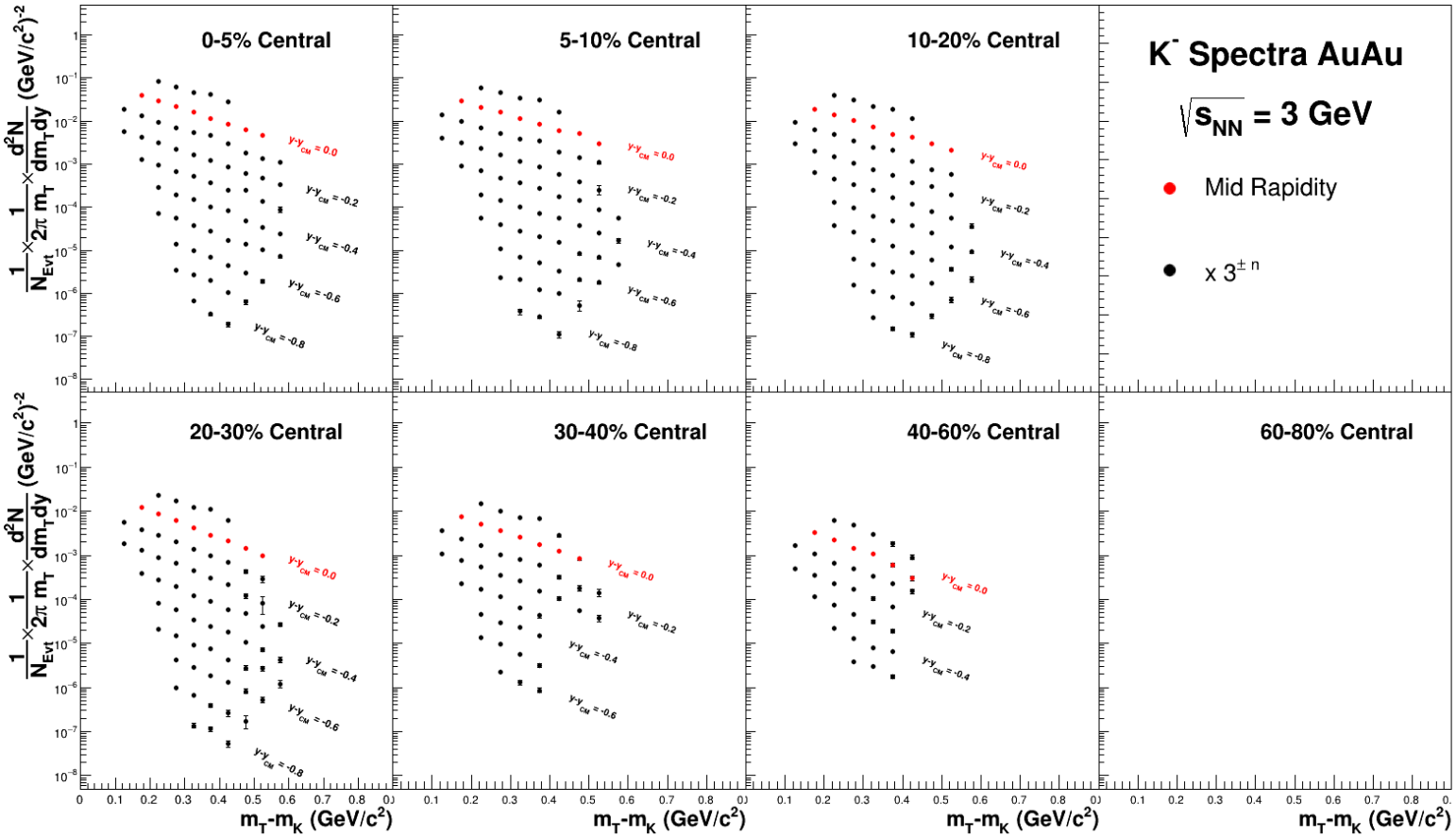

Figure 7.9: Invariant yield of K^- at $\sqrt{s_{NN}} = 3.0$ GeV

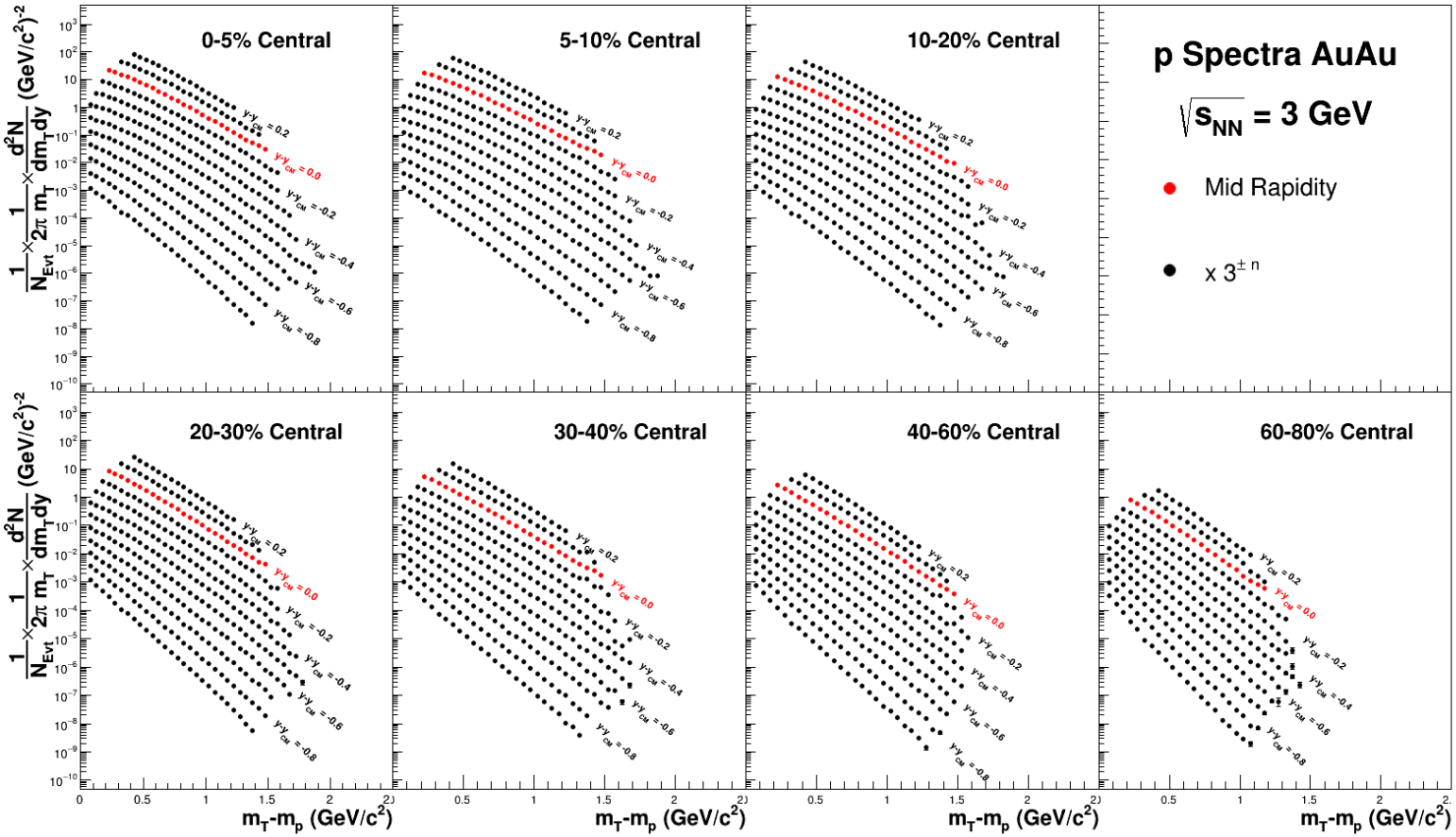

Figure 7.10: Invariant yield of p at $\sqrt{s_{NN}} = 3.0$ GeV

Chapter 8

Hadron Yields

This chapter presents the yields of pions, kaons, and protons. The first aspect of this is the invariant transverse mass spectra, which have already been presented in section 7.4. These spectra are fit with various models, discussed in section 8.1, with all fits to the spectra shown in section 8.2. The spectra and corresponding fits are then integrated to obtain the rapidity density distributions, dN/dy, and mean transverse momentum distributions, $\langle p_T \rangle$, presented in section 8.3. Finally, the rapidity density distributions are then fit and integrated to obtain the full phase space yields, 4π yields, which are presented in section 8.4.

8.1 Spectral Fits

To extract the yield of each particle species in each rapidity bin, the transverse mass spectra must be integrated over m_T. Unfortunately, due to limited acceptance at low transverse mass, the measured spectra do not extend down to $m_T - m_0$ of zero and must be extrapolated with a fit function. This section will discuss the various fit functions used for each particle species.

8.1.1 General Fit Methodology

In the Au+Au collisions studied in this analysis, the particle yields must be symmetric around midrapidity. This is implemented by performing simultaneous fits of all rapidity bins of a particle,

using the same parameters for pairs of rapidity bins which are equidistant from midrapidity. Additionally, many of the fit parameters are constrained to have a particular rapidity dependence as a function of rapidity, details of which will be discussed for each particle fit model. For each centrality, a single χ^2 is obtained for each particle species, incorporating the fits from all rapidities, which is then minimized to obtain the best overall fit for all spectra across all rapidities. Furthermore, positively and negatively charged particles of a given species are also fit simultaneously, ensuring they have the same spectral shape, though their amplitudes are allowed to be different.

8.1.2 Pions

Pions have two main production mechanisms in heavy-ion collisions: thermal (pair) production and production from the decay of the Δ-resonance. At the higher collision energies previously analyzed by STAR, the thermal production mechanism has been significantly higher and so the Δ production mechanism has been ignored. However, at the low energy of this analysis, evidence from previous measurements indicates that the Δ production mechanism plays a significant role in the pion yields. In order to account for these two production mechanisms, the sum of two thermal distributions is used to fit the pion spectra, with the form

$$\frac{1}{N_{\text{Evt}}}\frac{1}{2\pi m_T}\frac{d^2N}{dm_T dy} = A_{\text{low}} m_T e^{-(m_T-m_0)/T_{\text{low}}} + A_{\text{high}} m_T e^{-(m_T-m_0)/T_{\text{high}}}, \tag{8.1}$$

where T_{low} and T_{high} are the low and high temperatures, and A_{low} and A_{high} are the low- and high-temperature amplitudes respectively. The low-temperature term describes the production of pions when the Δ-resonance decays into a pion and nucleon while the high-temperature term describes the thermal production of pions. Examples of these fits for midrapidity pions in 0-5% central collisions can be seen in Fig. 8.1.

For each charge, the rapidity dependence of the low- and high-temperature amplitudes are parameterized as a Gaussian and as a hyperbolic cosine ($A_{\text{high}} = A_{\text{A,High}} \cosh\left[(y - y_{\text{CM}})/\sigma_{\text{A,high}}\right]$) respectively, both centered at midrapidity. Similarly, the rapidity dependence of both the low and

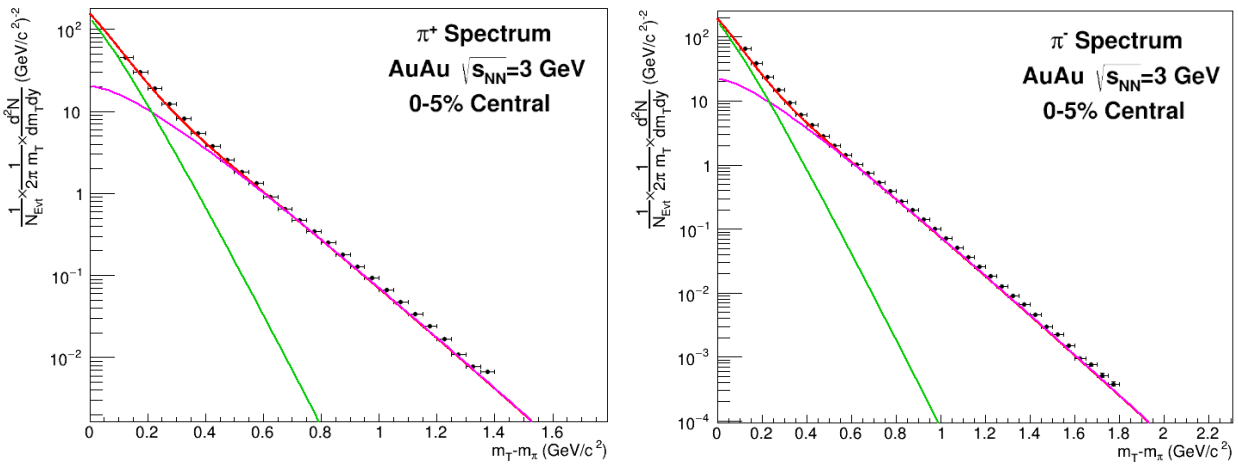

Figure 8.1: The sum of two thermal distributions, fit to the midrapidity π^+ (left) and π^- (right) spectra in 0-5% central collisions. The green line represents the low-temperature term, the magenta line represents the high-temperature term, and the red line represents the sum of the two.

high temperatures are parameterized as Gaussians, also centered at midrapidity. This reduces the number of parameters for the simultaneous fit of all rapidity bins for positive and negative pions to 12, which is significantly smaller than the 124 parameters (14 rapidity bins for π^+ and 17 for π^-, with two amplitude and two temperature parameters needed for each spectrum) required without such parameterizations. The functional form for the rapidity dependence of each parameter was empirically determined by first performing the fit with all parameters free and observing trends across rapidity. The variable that displayed the strongest trend was then parameterized according to the observed shape and then constrained to that shape for the following fit. This process was repeated until all variables were constrained to the previously described rapidity dependence. After these parameterizations were made, additional fitting was done to observe the trends of each new variable (amplitudes and widths of Gaussians or hyperbolic cosines) as a function of $N_{\rm part}$. In order to improve stability of the fits, many of these new variables were again successively constrained as a function of $N_{\rm part}$.

$A_{\rm A,low}$ (the low-temperature Gaussian amplitude) was constrained to be parabolic for π^+ and to be linear for π^- as a function of $N_{\rm part}$. One may expect the same $N_{\rm part}$ dependence of these

amplitudes for π^+ and π^-, but the differences in their production through the Δ resonance may explain the difference in shape, particularly as each production cross section changes with energy and a higher $N_{\rm coll}$ (generally corresponding to a higher $N_{\rm part}$) suggests a lower average collision energy. In the final fits, these low-temperature Gaussian amplitudes are permitted to deviate by $\pm 10\%$ and $\pm 5\%$ from the parameterized values for π^+ and π^- respectively. $\sigma_{\rm A,low}$ (the low-temperature Gaussian standard deviation) was fixed at 0.7, independent of $N_{\rm part}$, which may suggest isotropic production of pions in the Δ rest frame that gets smeared in the laboratory frame.

$A_{\rm A,high}$ (the high-temperature amplitude of the hyperbolic cosine) were left free for both π^+ and π^-, although they both exhibit a quite linear trend across centrality which is expected as the pion multiplicity plays a large part in characterizing the centrality of collisions. $\sigma_{\rm A,high}$ (the high-temperature hyperbolic cosine width) was fixed at 0.7 for π^+ and 0.9 for π^-, again independent of $N_{\rm part}$. The difference in $\sigma_{\rm A,high}$ for π^+ and π^- may be an indication that the parameterizations used are not perfect, as the pair production of pions at high temperature should be equal.

For each term in the spectral fit, the same temperatures are used for both charges of pion (i.e. $T_{\pi^+,\rm low} = T_{\pi^-,\rm low}$ and $T_{\pi^+,\rm high} = T_{\pi^-,\rm high}$). $A_{\rm T,low}$ was fixed to 0.06 GeV across all $N_{\rm part}$ while $\sigma_{\rm T,low}$ is fixed to 1.55 across all $N_{\rm part}$ (the latter being empirically determined by averaging the values observed by E895 [34]), with $A_{\rm T,high} = 0.129$ GeV at midrapidity in 0-5% central collisions. $A_{\rm T,high}$ and $\sigma_{\rm T,high}$ are both constrained to be a linear function of $N_{\rm part}$, which indicates that freeze-out for pair production occurs at a higher temperature in central collisions, perhaps due to the higher likelihood of producing pions from a Δ.

In order to evaluate the systematic uncertainty, an alternative fit function is used to extrapolate to $m_T - m_0 = 0$. For pions, this alternative function is an exponential in $m_T - m_0$

$$\frac{1}{N_{\rm Evt}} \frac{1}{2\pi m_T} \frac{d^2N}{dm_T dy} = Ae^{-(m_T - m_0)/T}, \tag{8.2}$$

where A and T are the amplitude and temperature respectively. This function cannot describe the two-slope nature of the pion spectra but is only used to extrapolate to $m_T - m_0 = 0$ and so it is

only used to fit the lowest four points in each spectrum.

8.1.3 Kaons and Protons

Kaons, like pions, have two main production mechanisms in heavy-ion collisions: thermal (pair) production and associated production with the Λ baryon. Details of these production mechanisms will be discussed in chapter 9. Unfortunately, the low $m_T - m_0$ acceptance of the kaons is not sufficient to disentangle these two mechanisms so a single function is used in the fits. Additionally, both kaons have the same spectral shape, which would naively suggest they are produced by pair production, however their yields are dramatically different indicating that there must be some additional production mechanism for K^+ that does not exist for K^-. Kaons have traditionally been fit with an exponential in $m_T - m_0$ (Eq. 8.2), but this form fails to describe the downward curvature of the kaon spectra at low $m_T - m_0$ and has such been relegated to the determination of systematic uncertainties. The curvature observed in the kaon spectra appears to be due to the radial expansion of the fireball and thus a blast-wave model has been used to fit the data. The same model is used to fit the protons. Such radial flow effects should be present in all particle species, but since it is mass dependent, it is much more difficult to observe in the pion spectra. The blast wave model used was formulated by Heinz, Schnedermann, and Sollfrank [52] and assumes a boost-invariant region around midrapidity. This implies that the rapidity dependence of the particle yields is flat as a function of rapidity, which is clearly not the case at the low energy of this analysis, as evident by other measurements. Nevertheless, this blast wave model is still used without any interpretation of the parameters across rapidity and with the sole intent to extrapolate to $m_T - m_0 = 0$. Due to the boost-invariant assumption of this model, which assumes a cylindrical expansion of the fireball, cylindrical coordinates are used and the system is described by a radially-dependent velocity profile, $\beta_T(r) = \beta_s \left(r/R\right)^n$. The quantity R represents the radial distance to the surface of the fireball. The quantity r represents the distance from the center of the fireball with $0 \leq r \leq R$. Due to the relationship between r and R, the exact value of R is irrelevant so it is set to unity. The parameter β_s represents the surface velocity of the fireball, which is equivalent to β_T when $r = R$. The parameter

n controls the shape of the transverse velocity profile. The blast wave model has the form

$$\frac{1}{N_{\text{Evt}}}\frac{1}{2\pi m_T}\frac{d^2N}{dm_T dy} = A\int_0^R rdrm_T I_0\left(\frac{p_T\sinh\rho(r)}{T_{\text{kin}}}\right)K_1\left(\frac{m_T\cosh\rho(r)}{T_{\text{kin}}}\right), \tag{8.3}$$

where I_0 and K_1 are the modified Bessel functions of the first and second kind respectively, T_{kin} is the temperature at kinetic freeze-out, and $\rho(r) = \tanh^{-1}\beta_T(r)$.

Fits of the kaons alone were unstable, therefore simultaneous fitting of K^+, K^-, and p were performed across all rapidities. The parameters β_s and T_{kin} were initially left free to observe the trends across rapidity and were then constrained successively. The kinetic temperature was determined to be independent of rapidity and is therefore held constant, though different values are required for the kaons (both charges of kaon use the same value) and protons. The surface velocity is constrained to a quartic polynomial without terms of odd degree in order to properly describe the observed flatness of β_s near midrapidity. The kaon amplitudes were also constrained to be Gaussian after observing the rapidity trends. Additionally, linear trends across the number of participants were observed in many of the parameters, so the parameter values were further constrained to be within 5% of those obtained in the N_{part} trends, similar to what was done with the pion fits. The original authors of this blast wave model recommended the use of $n = 2$ as this reproduces the same velocity profile exhibited by hydrodynamics [52]; however, previous STAR analyses [53] left it as a free parameter, which resulted in dramatic changes in the parameter across both collision energy and centrality, along with large uncertainties. A systematic study of this parameter was performed to find the optimal value of n by fixing n while leaving other parameters free and finding the value of n which provided the lowest χ^2, with the results shown in Fig. 8.2. This study indicated that the optimal value is $n = 1$ at this energy, and so it has been fixed accordingly. Examples of the blast wave fits of kaons and protons can be seen in Figs. 8.3 and 8.4 respectively.

In order to estimate the systematic uncertainty due to the extrapolation to zero transverse mass for protons, a single thermal function (Eq. 8.1 with $A_{\text{low}} = 0$) is used. This function cannot describe the entire transverse mass range and is only fit to the lowest four transverse mass points in each

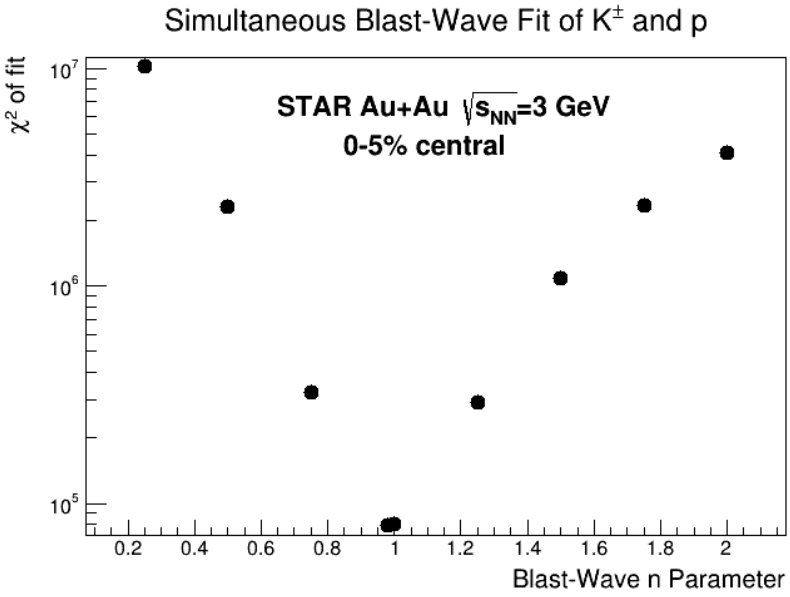

Figure 8.2: Scan of blast wave model n parameter in 0-5% central collisions. Simultaneous fits were done across all rapidities of $K^{\pm}$ and p with $0.25 \leq n \leq 2.0$ fixed in steps of 0.25 with an additional case of n left free. These fits indicate the lowest χ^2 when n is left free, giving $n = 0.98$. Leaving the parameter free creates more instability in the fits, so all fits in the analysis are fixed to $n = 1$, which provide similarly good fits of the data.

spectrum to best describe the behavior at low transverse mass.

8.2 Transverse Mass Spectra

In the section, the complete set of invariant transverse mass spectra obtained in this analysis are presented with their corresponding fits used to extrapolate to $m_T - m_0 = 0$. In each of the following figures, midrapidity is represented by red circles and a green curve. All other rapidities are represented by black circles and magenta curves. Midrapidity is unscaled, but other rapidities are scaled by $3^{\pm n}$, where n is how many bins away from midrapidity the corresponding bin is. To assist with readability, midrapidity is labeled as are each alternating rapidity bin. In the 60-80% centrality bin, it is clear that the spectra points exhibit different trends from the other centrality classes and the models only describe the data at low $m_T - m_0$, perhaps due to the large influence from spectators in such an extreme centrality bin.

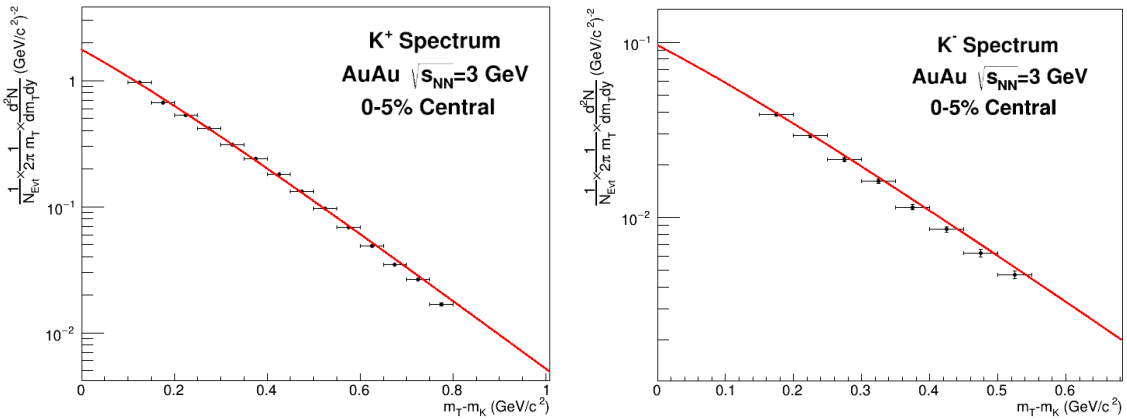

Figure 8.3: Blast wave model fit of midrapidity K^+ (left) and K^- (right) in 0-5% central collisions. The amplitude for the midrapidity fit of K^- appears to be too high, though it is good at other rapidities, which may indicate that a functional form other than a Gaussian for the amplitude may be optimal for 0-5% central collisions; however, to provide consistency across all centralities, the Gaussian was still used.

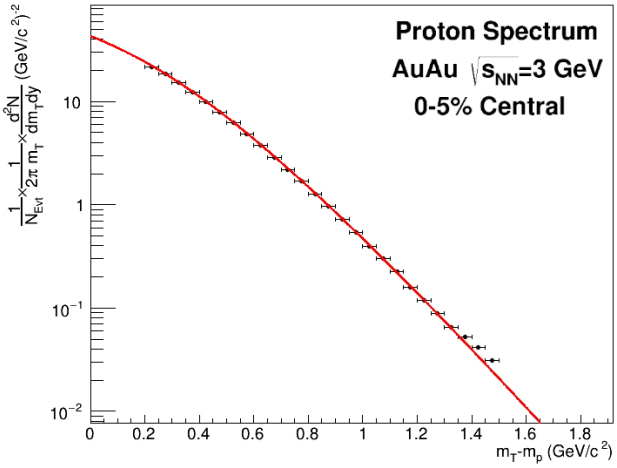

Figure 8.4: Blast wave fit of midrapidity p in 0-5% central collisions.

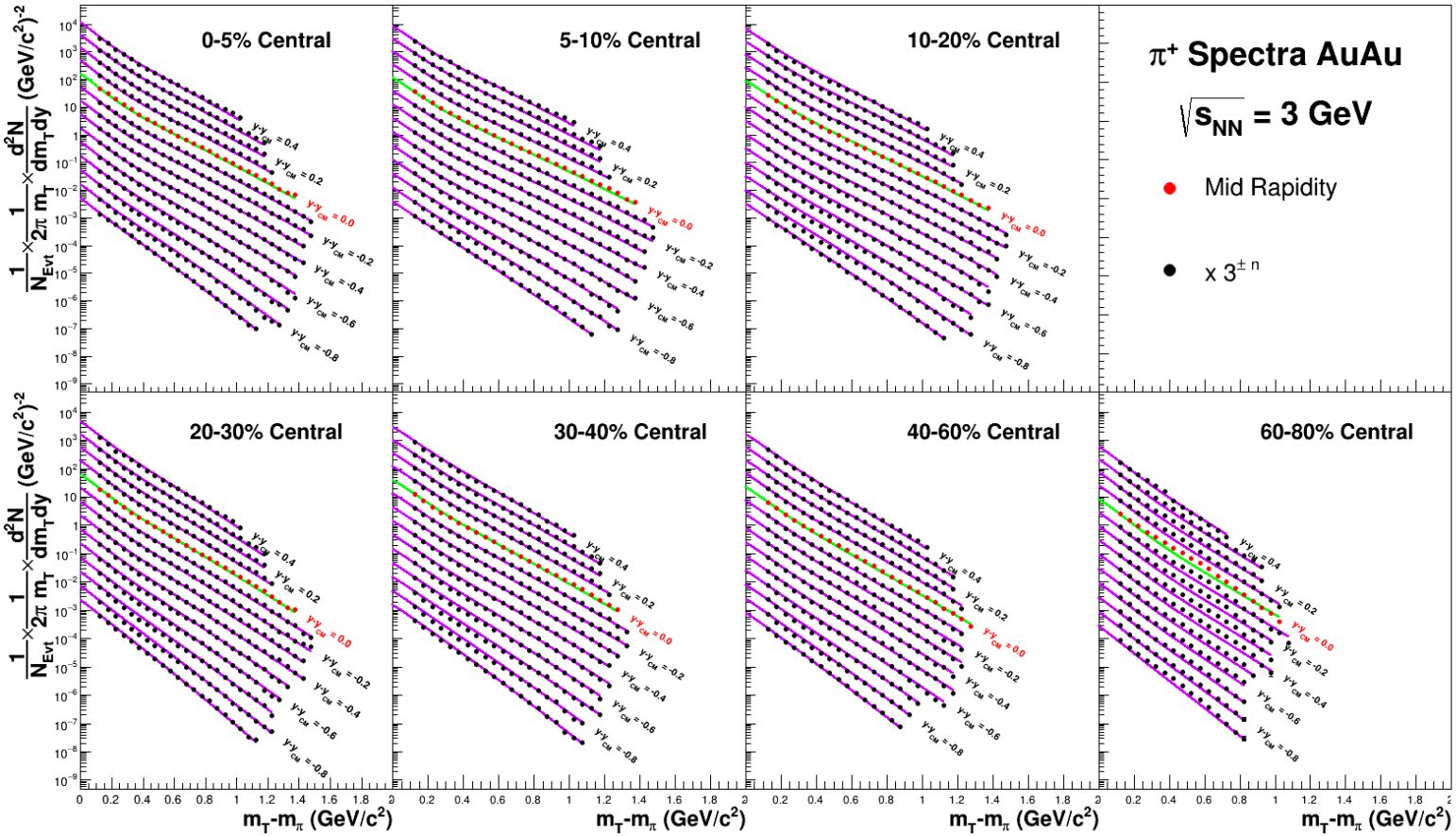

Figure 8.5: Invariant yield of π^+ at $\sqrt{s_{NN}} = 3.0$ GeV with fits for extrapolation to $m_T - m_0 = 0$.

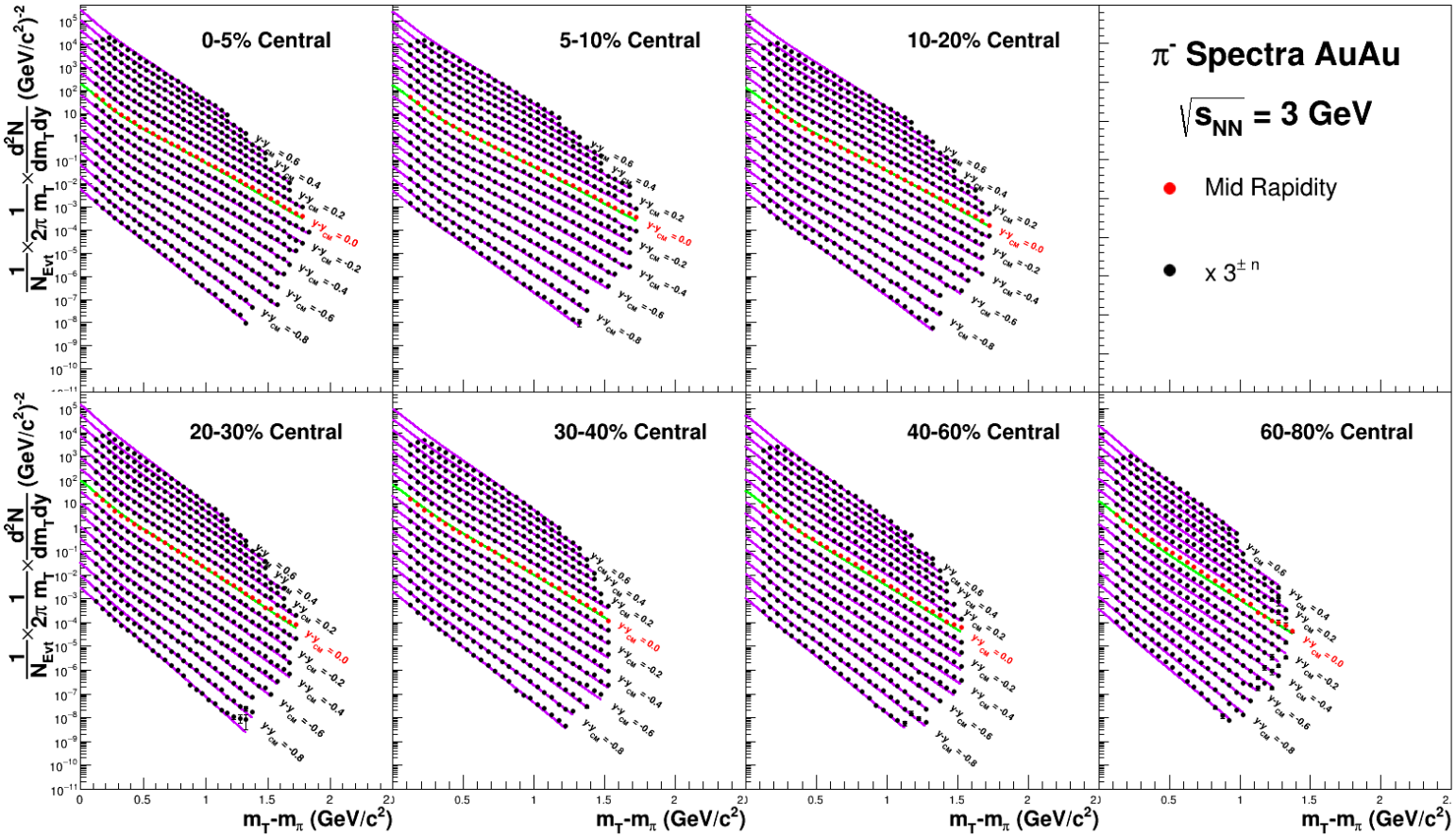

Figure 8.6: Invariant yield of π^- at $\sqrt{s_{NN}} = 3.0$ GeV with fits for extrapolation to $m_T - m_0 = 0$.

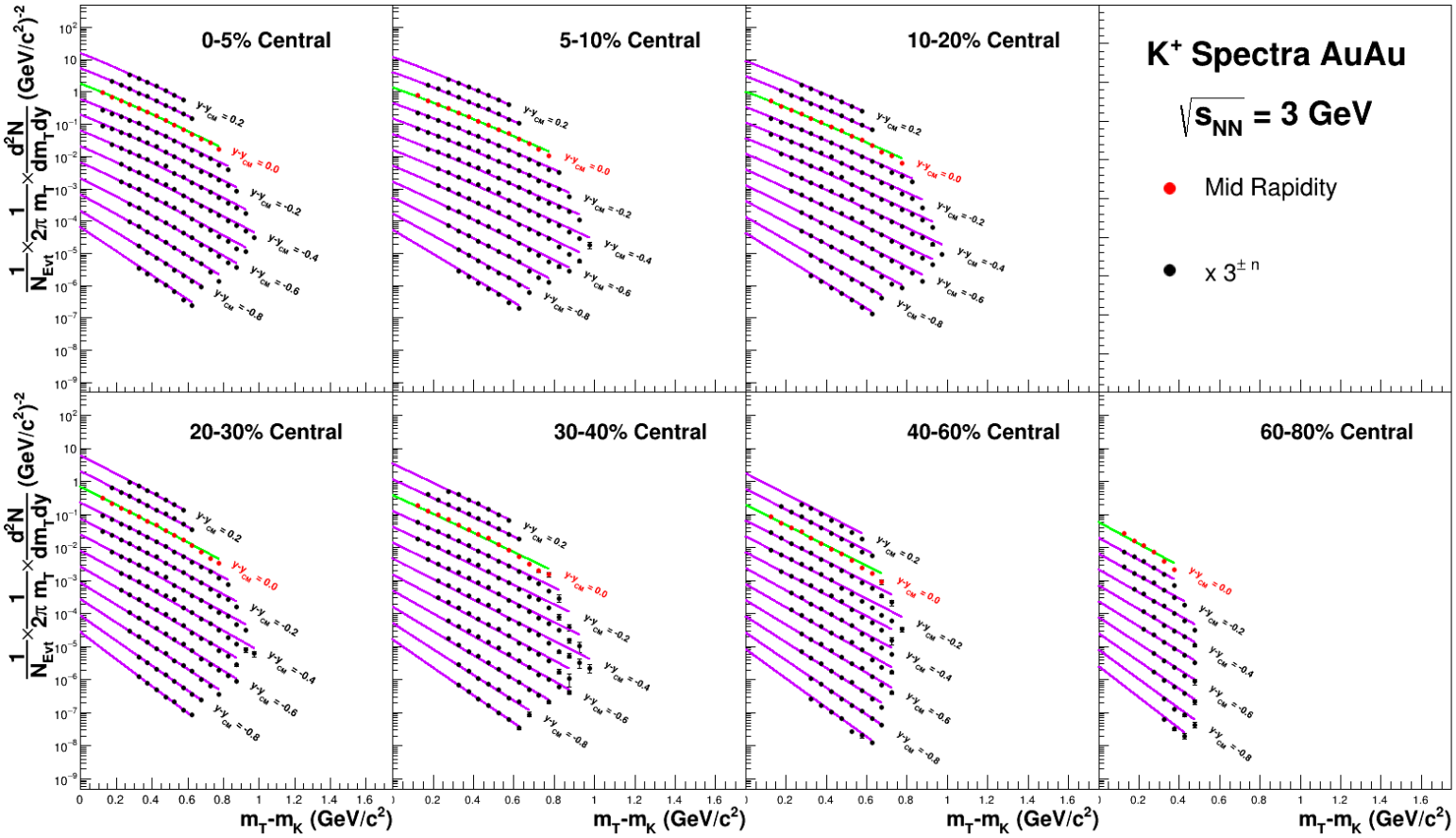

Figure 8.7: Invariant yield of K^+ at $\sqrt{s_{NN}} = 3.0$ GeV with fits for extrapolation to $m_T - m_0 = 0$.

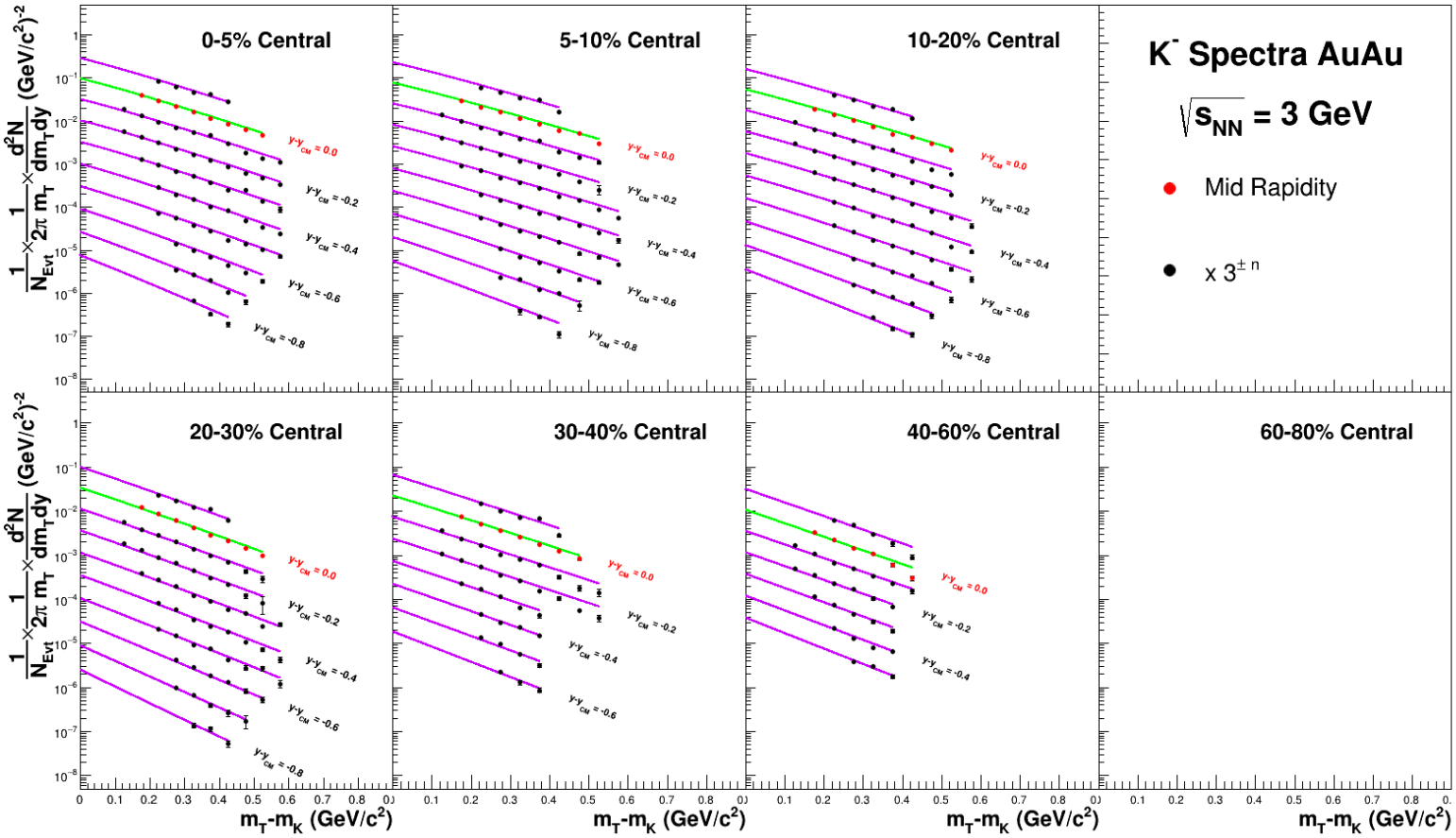

Figure 8.8: Invariant yield of K^- at $\sqrt{s_{NN}} = 3.0$ GeV with fits for extrapolation to $m_T - m_0 = 0$.

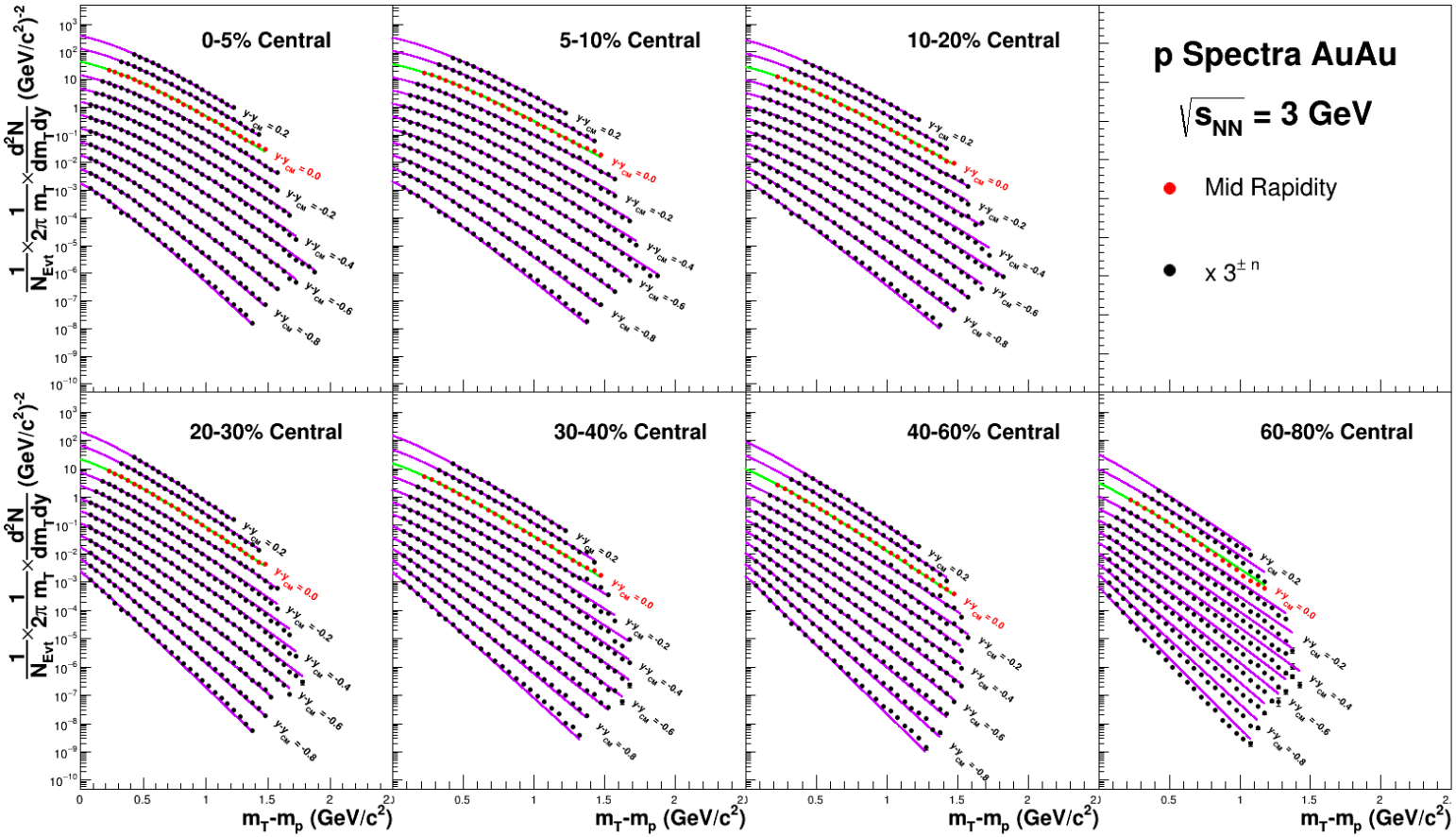

Figure 8.9: Invariant yield of p at $\sqrt{s_{NN}} = 3.0$ GeV with fits for extrapolation to $m_T - m_0 = 0$.

8.3 Rapidity Density & Mean Transverse Momentum Distributions

This section will present the rapidity density, dN/dy, and mean transverse momentum, $\langle p_T \rangle$, distributions for all particles in each centrality and rapidity bin. Each of the dN/dy and $\langle p_T \rangle$ values are determined with separate fiducial and extrapolated components, the former based purely on the measured spectra points and the latter based solely on the extrapolation to $m_T - m_0 = 0$. Statistical uncertainties are derived only from the fiducial result and the dominant contribution to the systematic uncertainties are determined by the absolute value of the difference between the nominal and systematic extrapolated values.

8.3.1 Rapidity Density Distributions

To obtain dN/dy, each invariant spectrum, multiplied by $2\pi m_T$, is integrated over transverse mass. This integration is first performed over the binned data points to obtain the fiducial yield and then on each of the nominal and systematic fit functions in the $m_T - m_0$ range of zero to the low edge of the lowest $m_T - m_0$ bin. The fiducial and extrapolated yields are then summed to obtain the nominal and systematic dN/dy, where the systematic and nominal central values are the same and the systematic uncertainty is the absolute value of the difference between the extrapolated nominal and systematic values. Figures 8.10-8.14 show the full rapidity density distributions for π^+, π^-, K^+, K^-, and p. Vertical lines represent statistical uncertainties (which generally lie within the drawn markers and are on the order of 0.5%) and boxes represent systematic uncertainties.

Physics requires the yields to be the same forward and backward of midrapidity. STAR was not designed to operate in a fixed-target geometry and such measurements are pushing the limits of its capabilities, but this means that not all rapidity bins are measured both forward and backward of midrapidity. In cases where the symmetric rapidity bins are measured, a weighted average is calculated using the inverse of the uncertainty squared as the weighting factor; these points are represented by solid stars in Figs. 8.10-8.14. In cases where only the backward rapidity was measured, those points are used directly and are then mirrored across midrapidity (midrapidity falls into this

class, but is not mirrored); these two cases are represented by solid and empty circles respectively in Figs. 8.10-8.14.

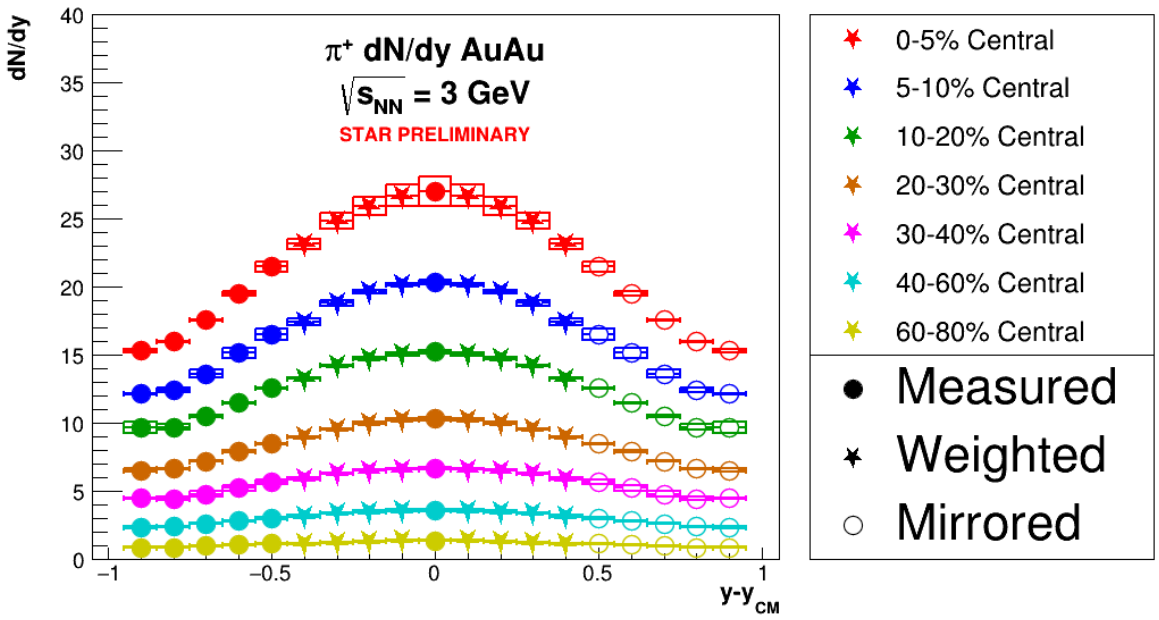

Figure 8.10: Rapidity density distribution of π^+ for all centralities.

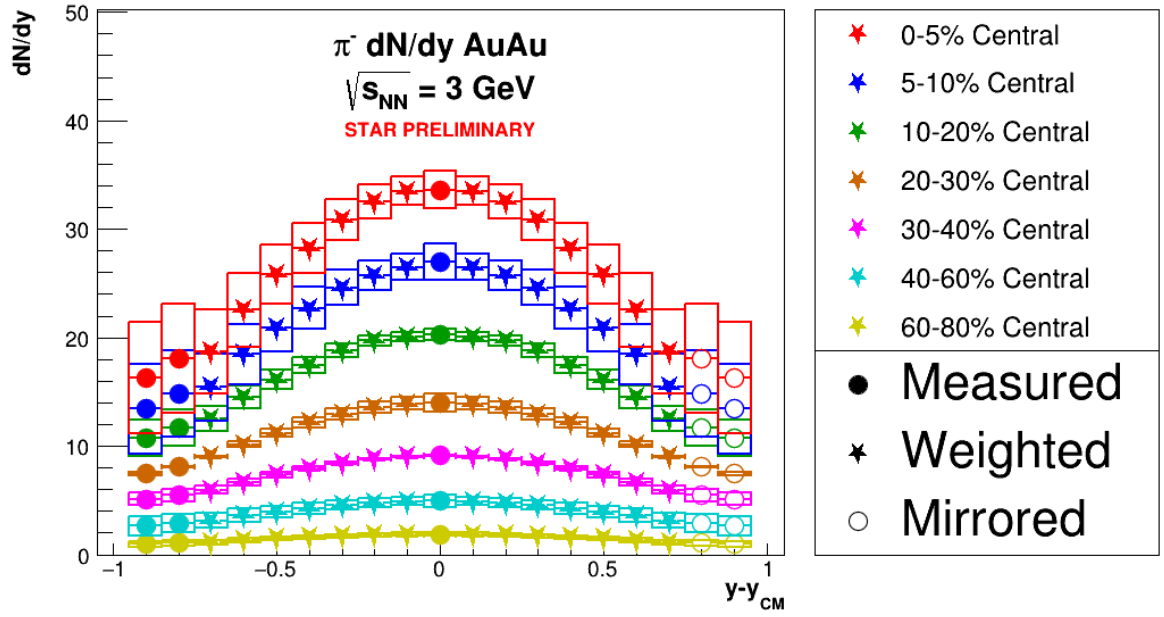

Figure 8.11: Rapidity density distribution of π^- for all centralities.

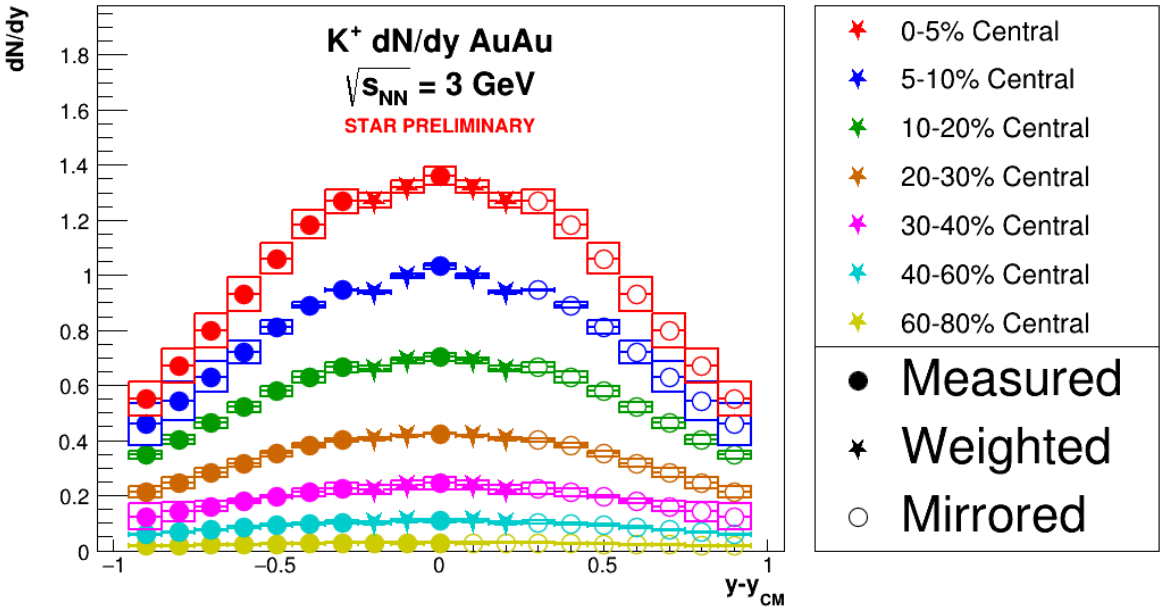

Figure 8.12: Rapidity density distribution of K^+ for all centralities.

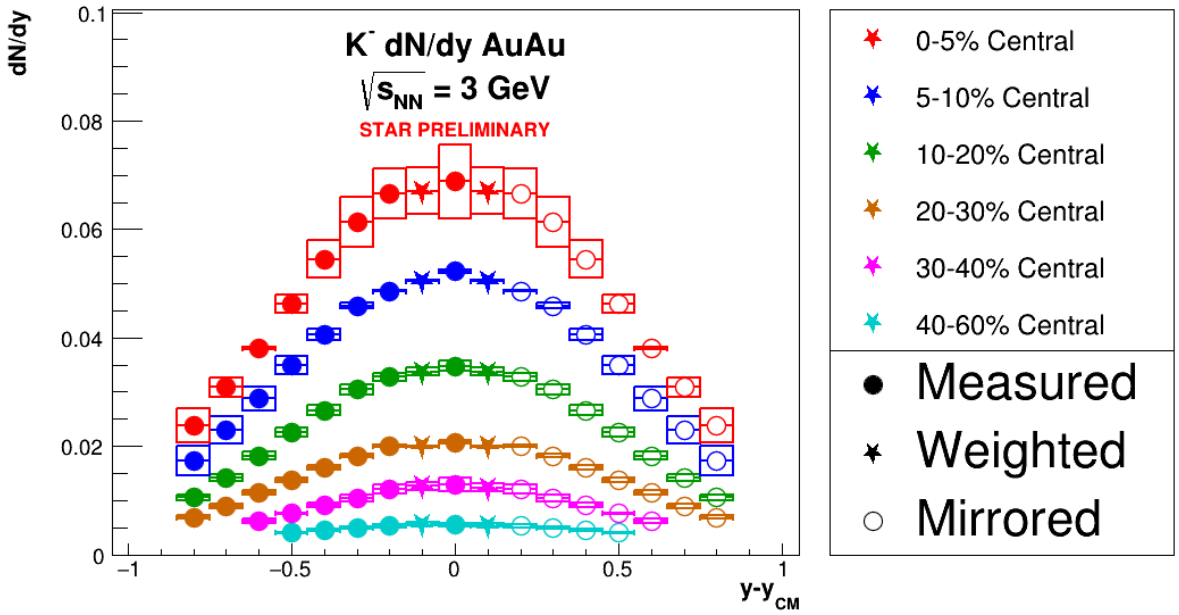

Figure 8.13: Rapidity density distribution of K^- for all centralities.

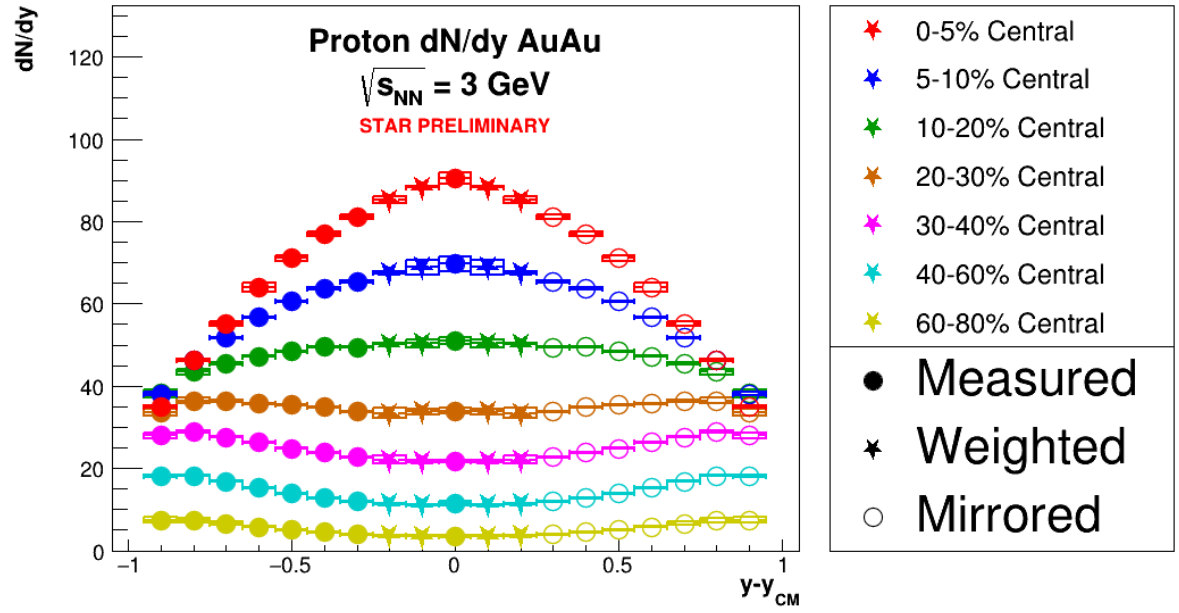

Figure 8.14: Rapidity density distribution of p for all centralities.

8.3.2 Mean Transverse Momentum Distributions

To obtain the $\langle p_T \rangle$, each invariant spectrum, multiplied by $2\pi m_T p_T$, is integrated over transverse mass. This integration is first performed over the binned data points to obtain the fiducial value and then on each of the nominal and systematic fit functions from $m_T - m_0 = 0$ to the low edge of the lowest $m_T - m_0$ bin. The fiducial and extrapolated integrals are then summed and subsequently divided by the total dN/dy in the corresponding bin to obtain the nominal and systematic $\langle p_T \rangle$, where the systematic and nominal central values are the same and the systematic uncertainty is the absolute value of the difference between the extrapolated nominal and systematic values. Figures 8.15, 8.16, 8.17, 8.18, and 8.19 show the mean transverse momentum distributions as a function of rapidity for π^+, π^-, K^+, K^-, and p respectively. Vertical lines represent statistical uncertainties and boxes represent systematic ones; large statistical uncertainties in the $\langle p_T \rangle$ of kaons is due to the larger uncertainties in the spectra points compared to the other particle species, particularly in more peripheral collisions where the yields are low. Unlike the dN/dy distributions, no symmetrization has been performed, nor have points been mirrored across midrapidity.

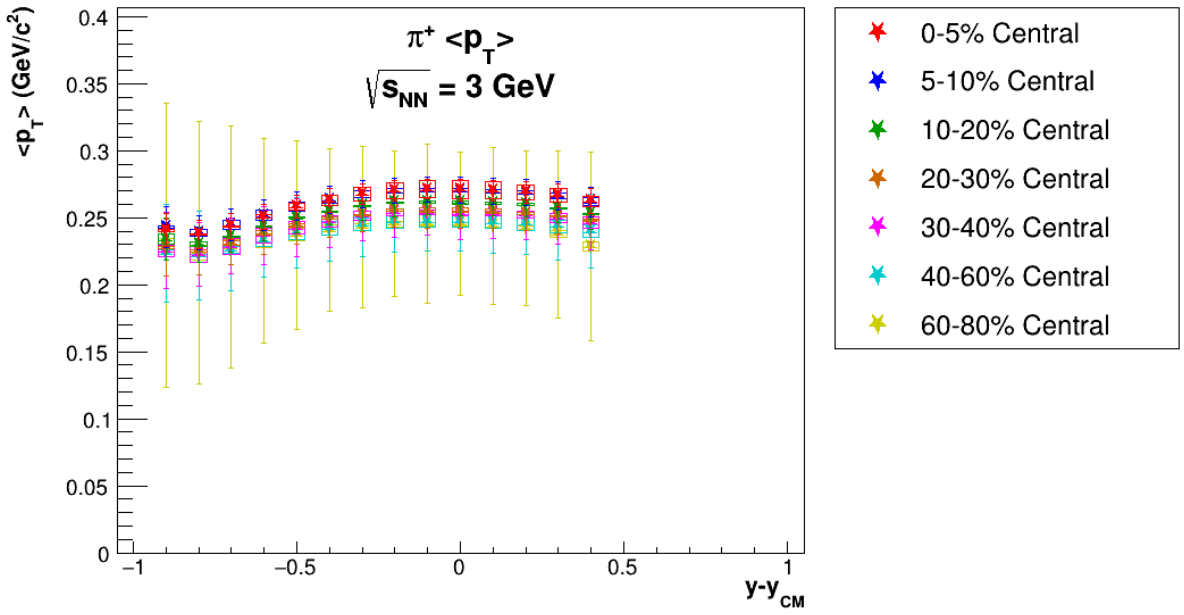

Figure 8.15: $\langle p_T \rangle$ of π^+ for all centralities.

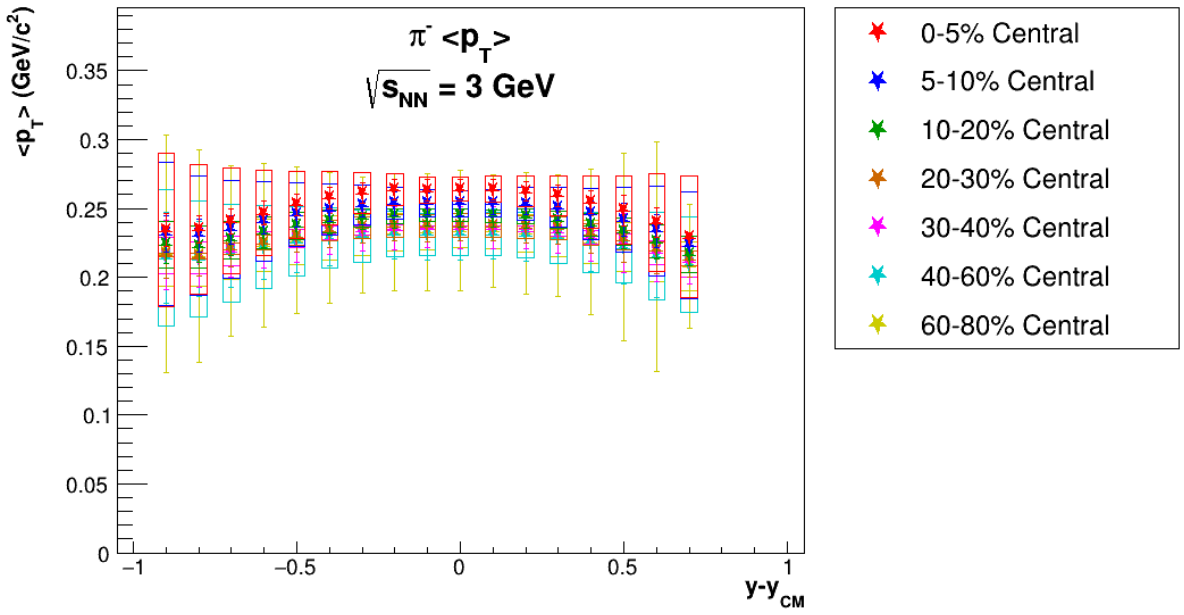

Figure 8.16: $\langle p_T \rangle$ of π^- for all centralities.

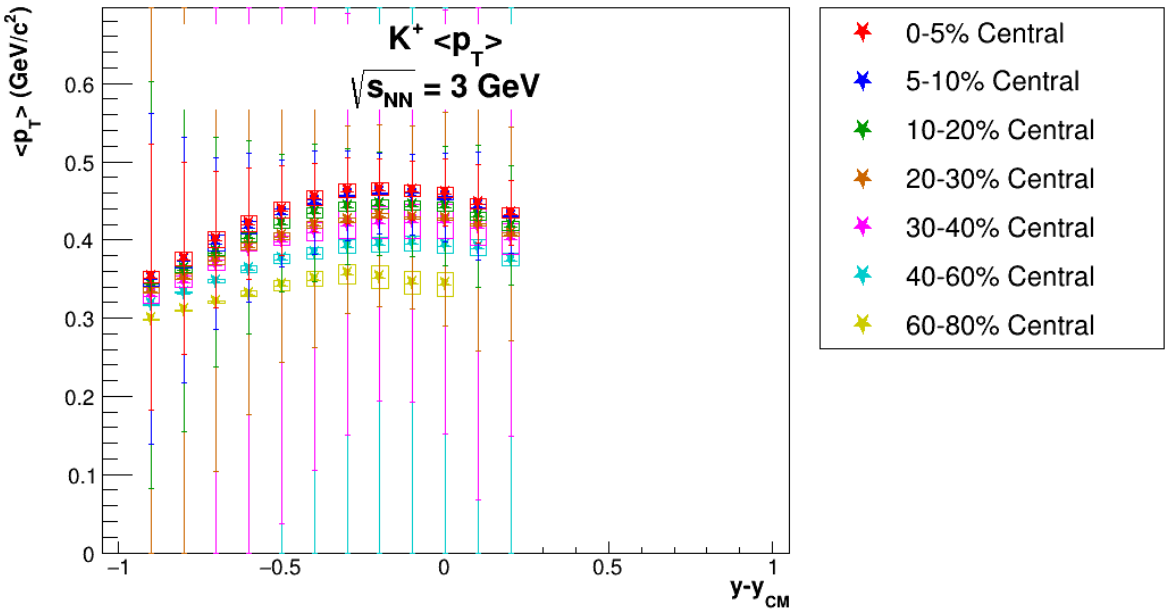

Figure 8.17: $\langle p_T \rangle$ of K^+ for all centralities.

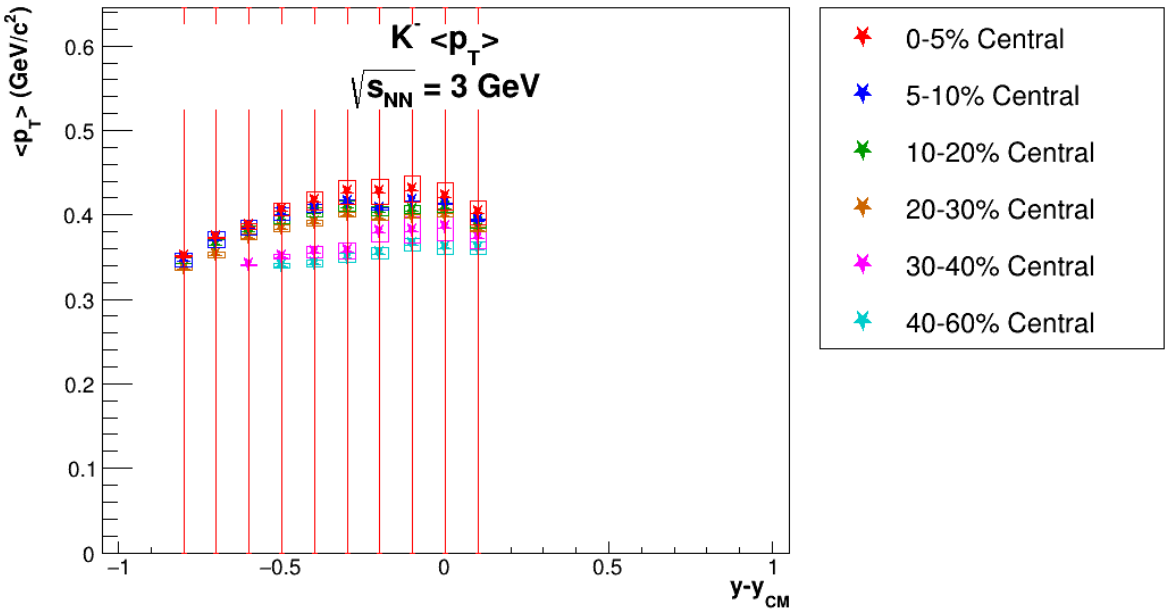

Figure 8.18: $\langle p_T \rangle$ of K^- for all centralities.

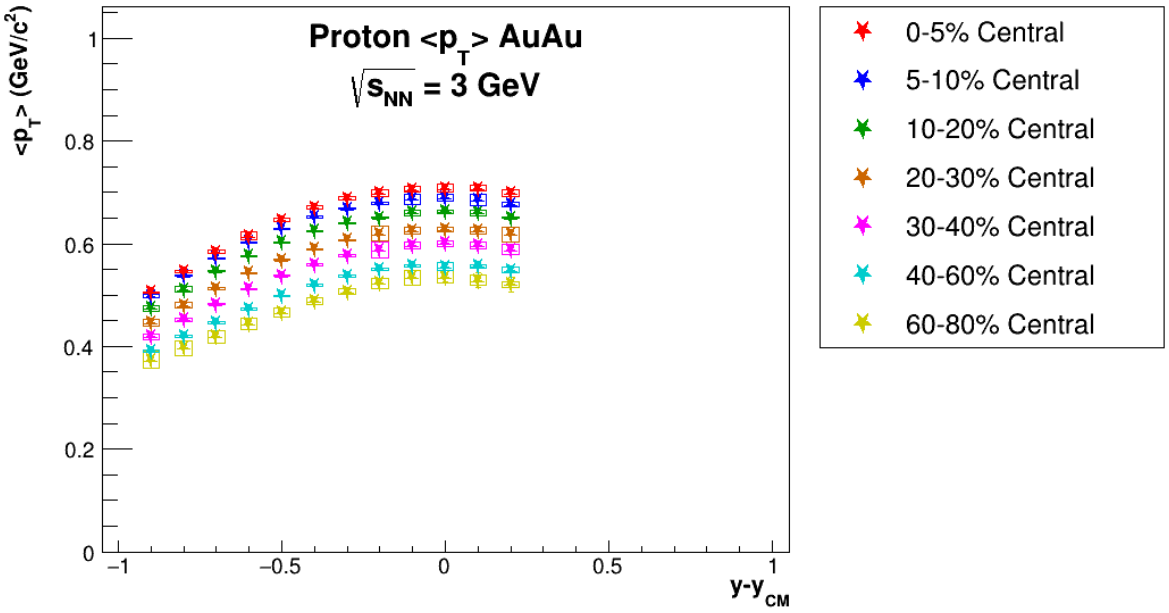

Figure 8.19: $\langle p_T \rangle$ of p for all centralities.

8.4 Full Phase Space Yields

This section will present the full phase space (4π) yields for each hadron. The rapidity density distributions can be fit with various different models and then integrated to obtain the 4π yields. In the case of pions and kaons, a single Gaussian distribution is used to fit dN/dy. Examples of these fits for 0-5% central collisions can be seen in Fig. 8.20. For protons, it is clear from Fig. 8.14

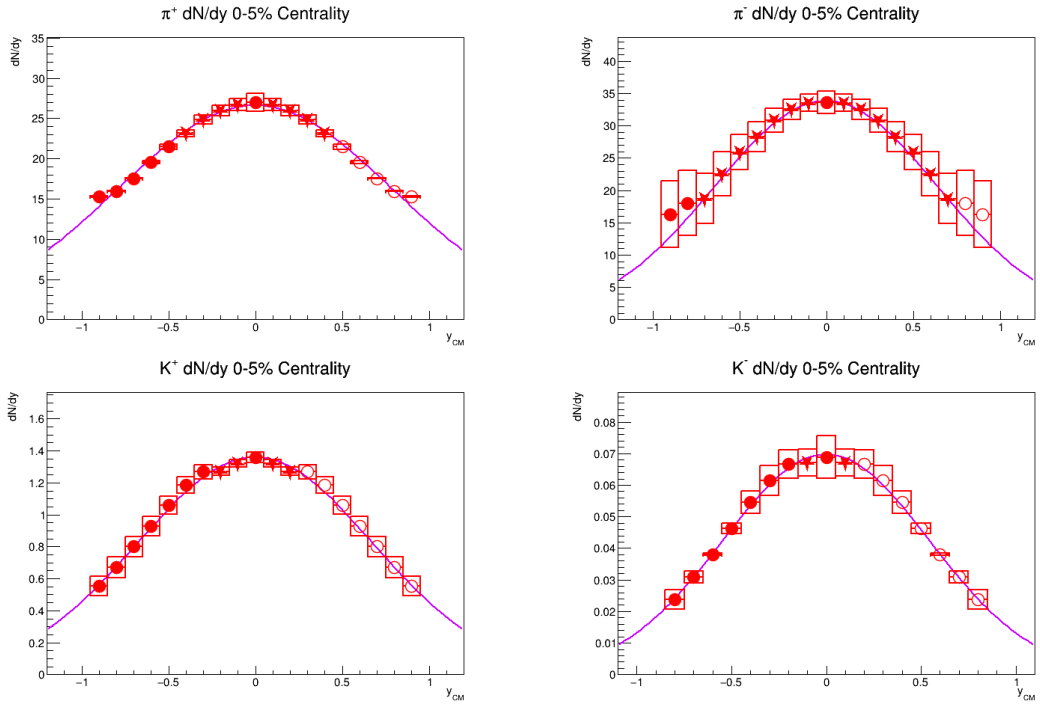

Figure 8.20: Single Gaussian fit of π^+ (top left), π^- (top right), $K+$ (bottom left), and $K-$ (bottom right) rapidity density distribution in 0-5% central collisions.

that a single Gaussian distribution would be insufficient to fit the dN/dy, particularly with more peripheral collisions. Initially, two mirrored Gaussian distributions were used, but they could not describe the rapidity distribution near both mid- and target rapidity. An asymmetric generalized Gaussian distribution was also attempted with better results, but still not providing the best fit. Instead, the author developed a new model based on the concept of baryon stopping.

As each participating nucleon interacts, it loses energy, which can be measured as a loss of

rapidity. Each collision undergone by a single nucleon will then cause additional rapidity loss. Using a Glauber Monte Carlo (as discussed in section 4.2), a distribution of the number of collisions undergone by a single nucleon was generated, as shown in Fig. 8.21. This is a discrete distribution and must be made continuous, which is done using a Gaussian kernel. A number of normalized Gaussians are constructed, each with their mean fixed to the integer value of a different bin and their yields fixed to the number of counts in that bin. A single standard deviation is used for all Gaussians (red curves in Fig. 8.21). These Gaussians are summed to obtain the total distribution, seen in magenta in Fig. 8.21. The standard deviation of these Gaussians is tuned so that the shape of the total distribution matches the distribution from the Glauber Model as closely as possible while being broad enough to not show bin effects. This procedure is followed for each centrality, providing different shapes with which to fit the proton rapidity density distributions at each centrality.

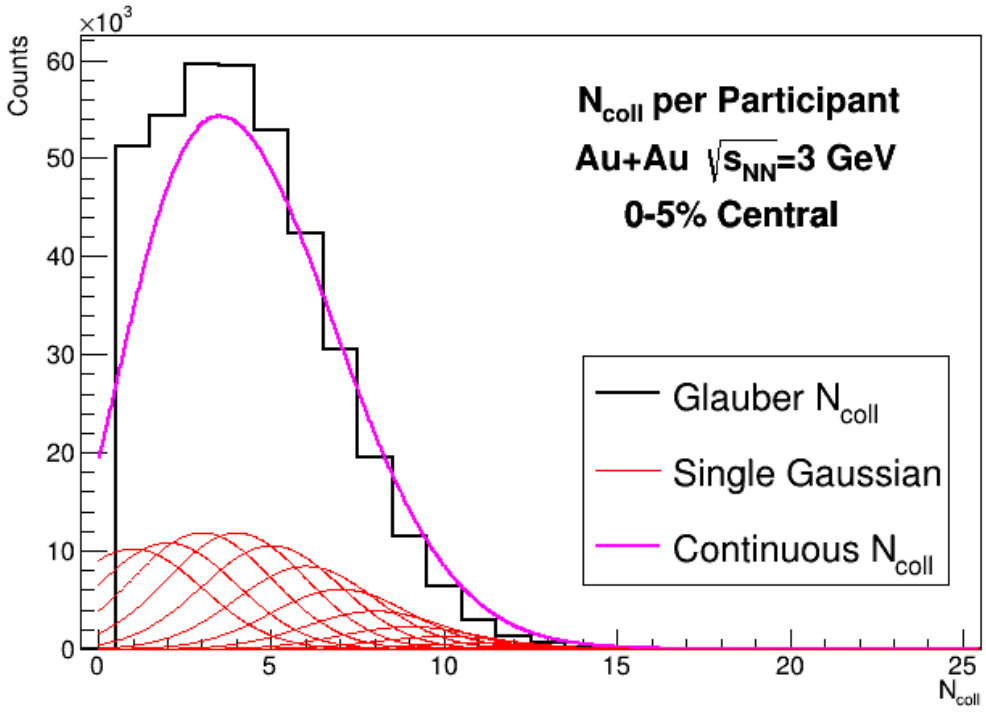

Figure 8.21: Model used to fit proton dN/dy. A distribution of N_{coll} for each participant is constructed from a Glauber Model and then smoothed using a Gaussian kernel.

The fit to the protons uses the sum of this functional form with a mirrored version (using the exact same parameters), with additional parameters to shift the peaks and stretch them both horizontally and vertically. In the fit to the dN/dy distribution, only these new parameters are allowed to change. This function does an excellent job of describing the proton dN/dy, as can be seen in Fig. 8.22. The agreement of this model with the data suggest that the model is quite accurately describing the phenomenon of baryon stopping, which will be further discussed in section 9.3.

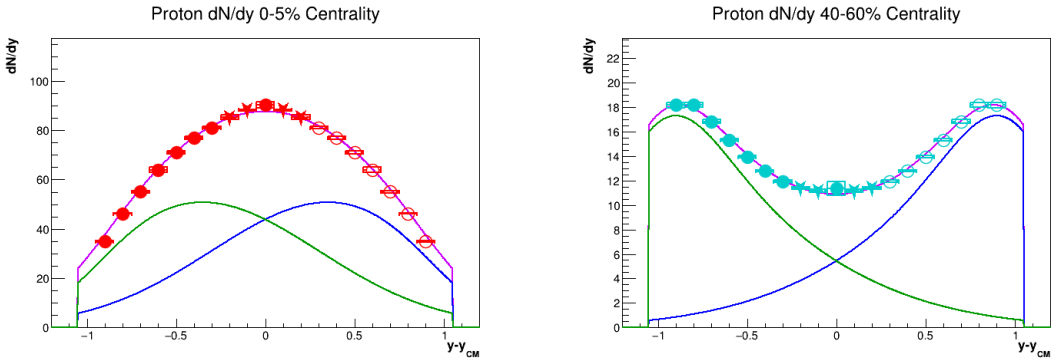

Figure 8.22: Fit of p rapidity density distributions incorporating two mirrored versions of the model described in the text for 0-5% central (left) and 40-60% central (right) collisions. The green and blue lines each represent one of the two functions of the form described in the text, which add together into the magenta line.

From each of these dN/dy fits, the full phase space yields can be obtained by integrating over rapidity. Figures 8.23-8.27 show the 4π yields for π^+, π^-, K^+, K^-, and p respectively as a function of N_{part}. The dependence on centrality is almost linear, as expected since particle multiplicity has been shown to scale with N_{part}.

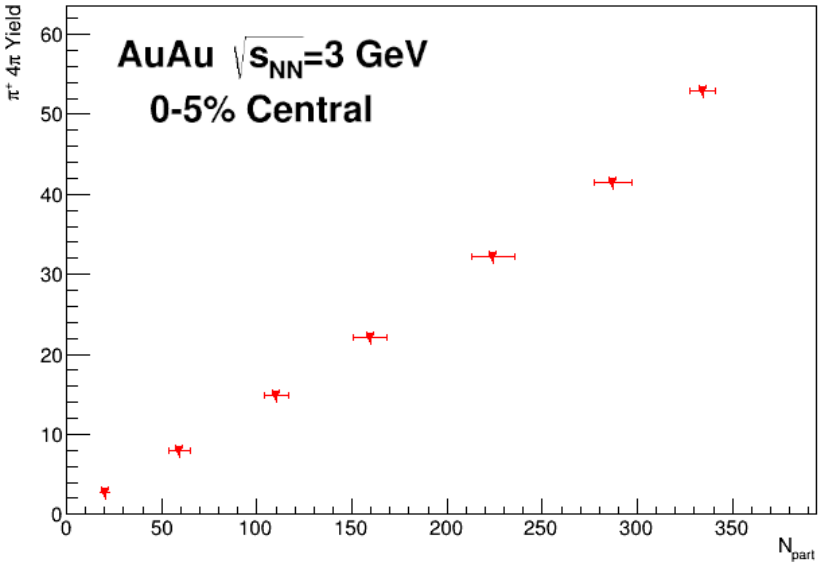

Figure 8.23: Full phase space yield of π^+ as a function of the number of participants in each centrality class.

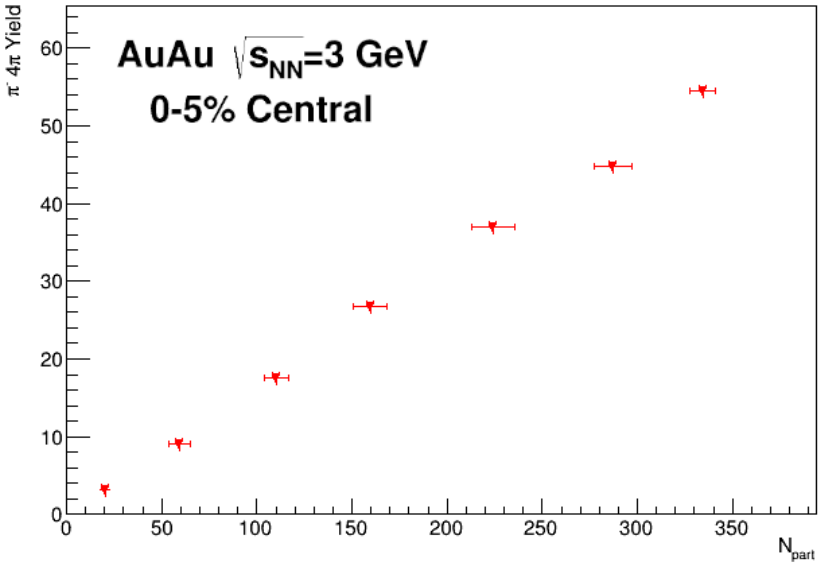

Figure 8.24: Full phase space yield of π^- as a function of the number of participants in each centrality class.

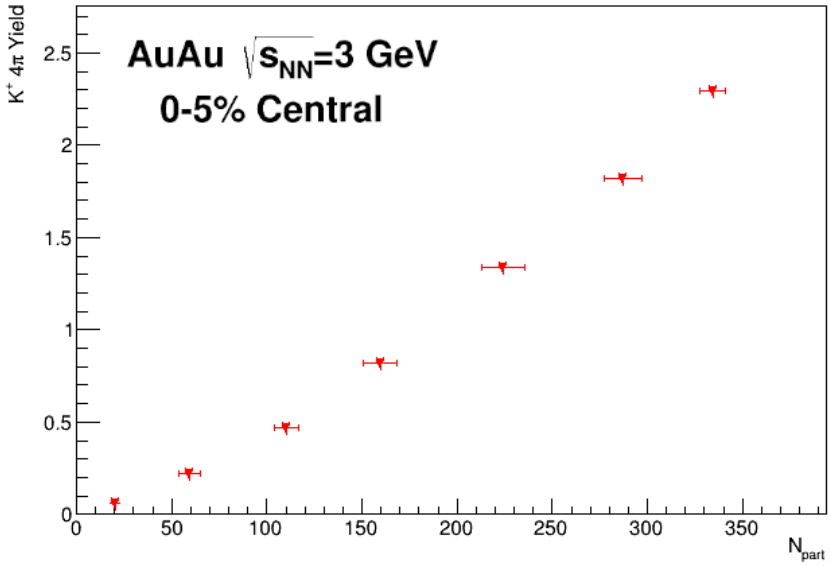

Figure 8.25: Full phase space yield of K^+ as a function of the number of participants in each centrality class.

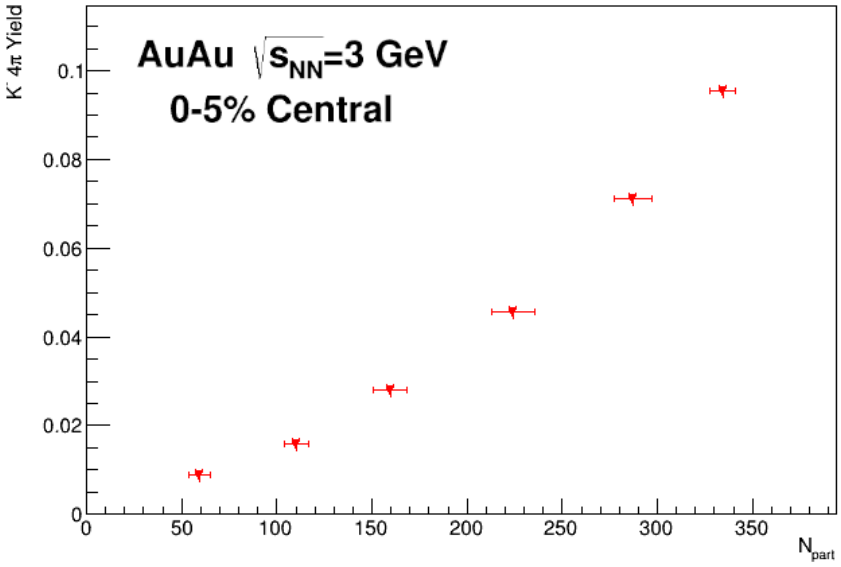

Figure 8.26: Full phase space yield of K^- as a function of the number of participants in each centrality class.

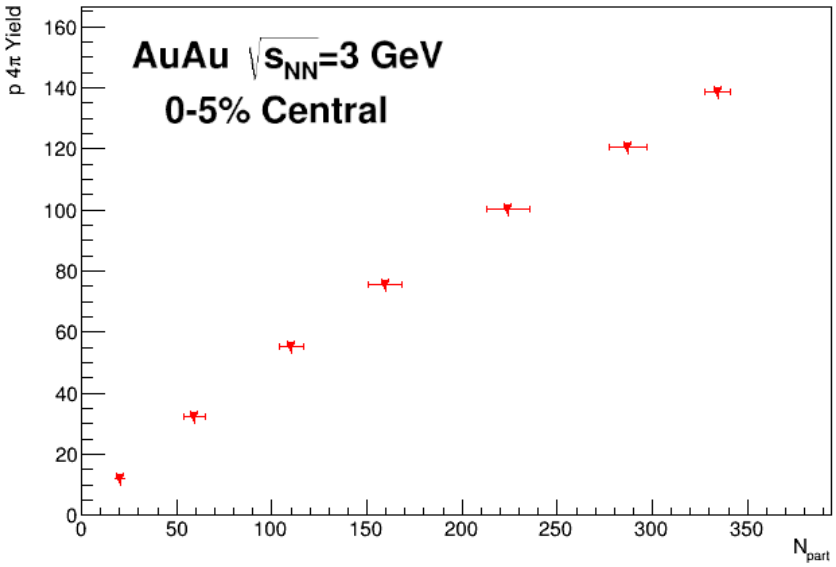

Figure 8.27: Full phase space yield of p as a function of the number of participants in each centrality class.

Chapter 9

Analysis and Interpretation

This chapter takes the measurements discussed in chapters 7 and 8, and presents additional physics observables along with interpretation. First, the pion ratio will be presented in section 9.1, which will lead to the extraction of the Coulomb potential of the fireball. Next, section 9.2 will present the ratio of kaons and discuss the associated production mechanism. Finally, baryon stopping will be discussed in section 9.3 and measurements of protons will demonstrate the centrality dependence of stopping.

9.1 Pion Ratios

Pions in heavy-ion collisions have two primary production mechanisms: thermal (pair) production and the decay of the Δ resonance. The former is relatively straightforward and dominates at top RHIC and LHC energies, however the latter is the dominating mechanism at $\sqrt{s_{NN}} = 3$ GeV.

9.1.1 Pion Ratio Predictions

It is useful to have a prediction of the observable in order to compare to the measurement. In order to obtain a prediction of the pion ratio, the probabilities of producing each pion from the decay of the Δ resonance must be calculated, as this will provide a lower limit to the pion ratio since the thermal ratio should be unity in the thermal scenario.

The Δ resonance is essentially an excited state of the nucleon with a spin of 3/2. The four Δ states, Δ^{++} (uuu), Δ^{+} (uud), Δ^{0} (udd), and Δ^{-} (ddd), form an isospin quartet, similar to the nucleon isospin pair. The Δ resonances almost always decay into a nucleon and pion, with each of these channels and the respective probabilities (determined through Clebsch-Gordan coefficients and the proton and neutron content of gold) shown in Tab. 9.1. The Clebsch-Gordan probabilities are

Production Channel	Clebsch-Gordan Probability	Total Probability
$p+p \rightarrow \Delta^{++}+n \rightarrow p+\pi^{+}+n$	0.75	0.1206
$p+p \rightarrow \Delta^{+}+p \rightarrow n+\pi^{+}+p$	0.0833	0.0134
$p+p \rightarrow \Delta^{+}+p \rightarrow p+\pi^{0}+p$	0.1667	0.0268
$p+n/n+p \rightarrow \Delta^{+}+n \rightarrow n+\pi^{+}+n$	0.1667	0.0801
$p+n/n+p \rightarrow \Delta^{+}+n \rightarrow p+\pi^{0}+n$	0.3333	0.1601
$p+n/n+p \rightarrow \Delta^{0}+p \rightarrow n+\pi^{0}+p$	0.3333	0.1601
$p+n/n+p \rightarrow \Delta^{0}+p \rightarrow p+\pi^{-}+p$	0.1667	0.0801
$n+n \rightarrow \Delta^{0}+n \rightarrow n+\pi^{0}+n$	0.1667	0.0598
$n+n \rightarrow \Delta^{0}+n \rightarrow p+\pi^{-}+n$	0.0833	0.0299
$n+n \rightarrow \Delta^{-}+p \rightarrow n+\pi^{-}+n$	0.75	0.2691

Table 9.1: Production channels and decay paths for Δ resonances in heavy-ion collisions. The Clebsch-Gordan probabilities are determined from isospin and the total probabilities incorporate the number of protons and neutrons in gold.

determined adding the isospin of each hadron, since the total isospin and I_3 must be equal in every stage of the reaction, then multiplying the coefficients from each interaction/decay. For example, in $p+p \rightarrow \Delta^{+}+p \rightarrow n+\pi^{+}+p$, the $p+p$ interaction must have a total isospin of $|1,+1\rangle$ (with a probability of 1 from Clebsch-Gordan coefficients) which means $\Delta^{+}+p$ must have the same total isospin, which has a probability of 0.25. Next, the final state of $n+\pi^{+}+p$ must also be in the same isospin state, or really the $n+\pi^{+}$ must be in the same isospin state as Δ^{+} ($|\frac{3}{2},+\frac{1}{2}\rangle$), which has a probability of 0.33. All these probabilities are multiplied, giving the Clebsch-Gordan probability of 0.0833. The total probabilities take those Clebsch-Gordan ones, multiplied by the probability of the specific collision. The probability of $p+p$, $p+n/n+p$, and $n+n$ collisions are Z^2/A^2, $2Z(A-Z)/A^2$, and $(A-Z)^2/A^2$ respectively (where A is the atomic mass and Z is the atomic number of gold). Adding up the total probabilities for each pion, the following probabilities are obtained: $\pi^{+}=21.4\%$, $\pi^{0}=40.7\%$, and $\pi^{-}=37.9\%$. One essential assumption in this calculation

is that every NN collision will produce a Δ resonance, which is not inherently true. From the pion probabilities, the predicted pion ratio from the Δ resonance is $(\pi^+/\pi^-)_{\rm CG} = 56.5\%$.

A similar, empirical, prediction can be made using measured cross sections for these production processes. Measurements of the various cross sections for $N+N \rightarrow N+N+\pi$ through the production and successive decay of a Δ resonance have been performed and extracted [54] at 1 AGeV, which corresponds to the energy analyzed by the KaoS experiment in a $Au + Au$ system. The measured cross sections are $\sigma_{pp\rightarrow pn\pi^+} = 18.5$ mb, $\sigma_{pn\rightarrow nn\pi^+} + \sigma_{np\rightarrow nn\pi^+} = 5$ mb, and $\sigma_{pn\rightarrow pp\pi^-} + \sigma_{np\rightarrow pp\pi^-} = 5$ mb. The π^- production cross section through the $n + n$ process, $\sigma_{nn\rightarrow pn\pi^-}$, is not measurable as neutron targets are not possible and expected to be the same as $\sigma_{pp\rightarrow pn\pi^+}$ based on symmetry arguments. The cross section for each specific final state in an Au+Au collision is shown in Tab. 9.2. The total cross sections for each charged pion are: $\pi^+ = 4.176 \pm 0.160$ mb and $\pi^- = 7.838 \pm 0.337$

Process	σ of Process (mb)	Au+Au Prob.	$\sigma_{\rm Au+Au}$ of Process (mb)
$pp \rightarrow pn\pi^+$	18.5	0.161	2.975 ± 0.149
$pn \rightarrow nn\pi^+$ $+\ np \rightarrow nn\pi^+$	5	0.240	1.201 ± 0.060
$pn \rightarrow pp\pi^-$ $+\ np \rightarrow pp\pi^-$	5	0.240	1.201 ± 0.060
$nn \rightarrow pn\pi^-$	18.5	0.359	6.637 ± 0.332

Table 9.2: Probabilities of producing charged pions through the Δ resonance channel from measured cross sections at 1 AGeV. A 5% uncertainty is used for the measured cross sections to account for the measured uncertainties and the uncertainty in the extraction of the values from the figure.

mb, which gives a ratio of $(\pi^+/\pi^-)_\sigma = 53.3 \pm 3.1\%$. This is very close to and within uncertainty of the prediction extracted purely theoretically using the Clebsch-Gordan coefficients, which was $(\pi^+/\pi^-)_{\rm CG} = 56.5\%$, the difference most likely resulting from uncertainties in the cross sections.

Constructing a ratio of pions from the midrapidity yields or the full phase space yields is inherently not comparable to this predicted pion ratio as they both contain contributions from thermal pion production and have not been corrected for the attraction/repulsion caused by the Coulomb potential of the fireball. Both problems can be addressed by constructing a ratio of the pion spectra themselves, investigating the low transverse mass region where the Δ resonance production

mechanism dominates, and using a model to correct for the Coulomb effect from the fireball.

9.1.2 Coulomb Potential

The Coulomb potential of the fireball is expected to have a non-negligible effect on the momentum distributions of the measured charged hadrons. This should be most evident in the charged pions due to their light mass, thus motivating the use of the charged pions to extract the Coulomb potential. Previous analyses have extracted this Coulomb potential with a simple physics-based model. The measured final energy of the charged hadron should be related to its initial energy before any final-state modification and the Coulomb potential itself:

$$E_f^{\pm}(p_f) = E_i(p_i) \pm V_C, \tag{9.1}$$

or rearranged solving for E_i

$$E_i(p_i) = E_f^{\pm}(p_f) \mp V_C, \tag{9.2}$$

where p_i and p_f are the initial and final pion momenta and the $\pm$ in the E_f indicates the charge of the pion. The Coulomb potential must be positive as the net charge of the system is positive, so this demonstrates that π^+ will be shifted to a higher final energy and π^- will be shifted to a lower one relative to their initial energies. A Coulomb correction can then be made to a fit model for the pions [55]; in this case, a Bose-Einstein distribution was selected as pions are bosons and such a function is needed to properly describe the behavior at low transverse mass. The Bose-Einstein distribution

$$\frac{1}{N_{\text{Evt}}} \frac{1}{2\pi m_T} \frac{d^2N}{dm_T dy} = A \frac{1}{e^{E_i/T_\pi} - 1}, \tag{9.3}$$

is modified by replacing E_i with the right-hand side of Eq. 9.2. However, the current form of this model assumes a static source, which is known to not be the case in heavy-ion collisions where there is an expansion of the fireball. The charge of the fireball comes primarily from protons, therefore an effective Coulomb potential, V_{eff}, can be calculated by integrating the proton emission function up to

a maximum kinetic energy corresponding to the pion velocity, $E_{\max} = E_\pi m_p/m_\pi - m_p$. The effective potential can be written for a 2D expansion, assuming a cylindrical geometry with a transverse expansion, or for a 3D expansion assuming a spherical expansion

$$V_{\text{eff}} = \begin{cases} V_C\left(1 - e^{-x^2}\right) & \text{for 2D expansion,} \\ V_C\left(\text{erf}\,(x) - \frac{2}{\sqrt{\pi}} x e^{-x^2}\right) & \text{for 3D expansion,} \end{cases} \tag{9.4}$$

where $x = \sqrt{E_{\max}/T_p}$, T_p is the proton temperature (i.e. the temperature of the proton fireball), and $\text{erf}\,(x)$ is the error function [56]. The 2D expansion case is most applicable to higher energies where boost-invariance holds, which is clearly not the case here because the rapidity distributions peak at midrapidity. Instead, the 3D expansion case will be used at this energy, although the 2D case will be used at some higher energies for comparison.

Two Jacobians are required in this calculation: a Jacobian, $J^\pm$, to account for the conversion from initial to final coordinates and an effective Jacobian, $J^\pm_{\text{eff}}$, which results from the explicit dependence of V_{eff} on the pion kinetic energy, $E_{\max}$. The need for this effective Jacobian was recently idetified by the HADES collaboration [56], as it had been omitted in previous analyses. The derivations of these Jacobians are discussed in Appendix A, giving

$$J^\pm = \frac{E_i p_i}{E_f p_f} = \frac{(E_f \mp V_{\text{eff}})\sqrt{(E_f \mp V_{\text{eff}})^2 - m^2}}{E_f\sqrt{E_f^2 - m^2}}. \tag{9.5}$$

and

$$J^\pm_{\text{eff}} = \begin{cases} 1 \mp \frac{V_C m_p}{m_\pi T_p} e^{-x^2} & \text{for 2D expansion,} \\ 1 \mp \frac{2}{\sqrt{\pi}} \frac{V_C m_p}{m_\pi T_p} x e^{-x^2} & \text{for 3D expansion,} \end{cases} \tag{9.6}$$

with x as previously defined.

The inclusion of these Jacobians generates the Coulomb-corrected Bose-Einstein distribution

$$\frac{1}{N_{\text{Evt}}}\frac{1}{2\pi m_T}\frac{d^2N^\pm}{dm_T dy} = J^\pm \times J^\pm_{\text{eff}} \times \frac{A^\pm}{e^{(E_f \mp V_{\text{eff}})/T_\pi} - 1}, \tag{9.7}$$

where V_{eff} is defined in Eq. 9.4, $A^{\pm}$ is the amplitude, and T_π is the slope parameter, commonly called the temperature (to be exact, this is the temperature of the boson gas as the model uses Bose-Einstein statistics).

With the Coulomb-corrected Bose-Einstein distribution, the π^+/π^- ratio can be constructed using the 3D expansion by dividing the distribution for positive pions by the one for negative pions

$$R_f(E_f) = \frac{(E_f - V_{\text{eff}})\sqrt{(E_f - V_{\text{eff}})^2 - m^2}}{(E_f + V_{\text{eff}})\sqrt{(E_f + V_{\text{eff}})^2 - m^2}} \quad \frac{1 - \frac{2}{\sqrt{\pi}}\frac{V_C m_p}{m_\pi T_p} x e^{-x^2}}{1 + \frac{2}{\sqrt{\pi}}\frac{V_C m_p}{m_\pi T_p} x e^{-x^2}} \quad \frac{A^+}{A^-}\frac{e^{(E_f + V_{\text{eff}})/T_\pi} - 1}{e^{(E_f - V_{\text{eff}})/T_\pi} - 1} \quad . \tag{9.8}$$

This ratio can be used to fit the π^+/π^- ratio as a function of transverse mass, an example of which can be seen in Fig. 9.1 where the midrapidity pion ratio for 0-5% central collisions is fit. This

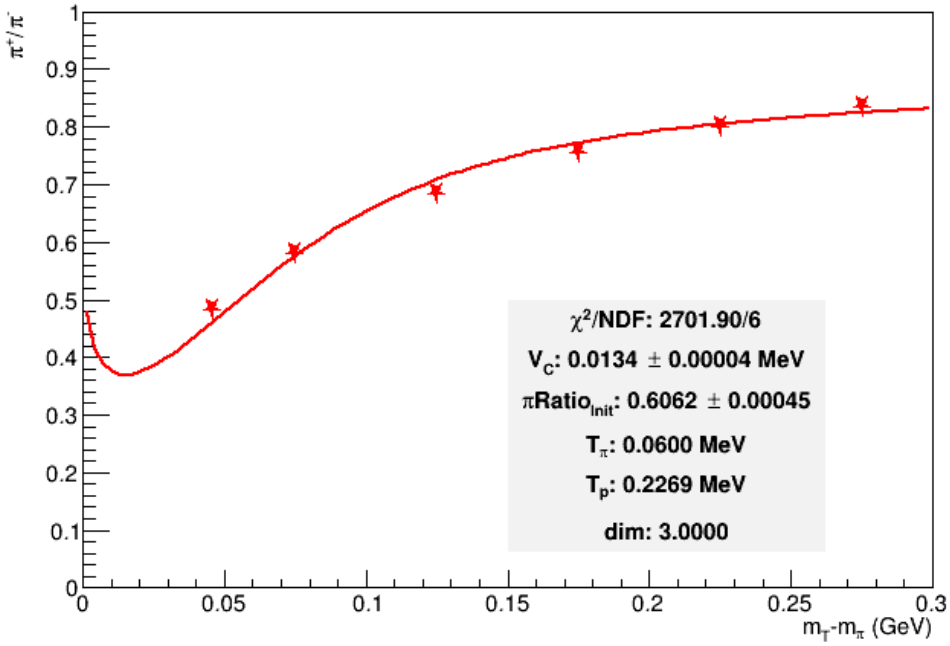

Figure 9.1: Ratio of π^+/π^- in $\sqrt{s_{NN}} = 3$ GeV collisions at midrapidity in 0-5% central collisions fit with Eq. 9.8. Fit parameters and χ^2/NDF can be seen in the inset box. The large χ^2/NDF is due to the very small statistical uncertainties of the spectra.

demonstrates that the model describes the data well, though the acceptance limits of STAR preclude

measurement of this ratio at lower transverse mass where the largest effect due to the Coulomb potential would be seen. This same model has been used to fit data from the KaoS experiment (at $\sqrt{s_{NN}} = 2.33$ GeV) and the E895 experiment (at $\sqrt{s_{NN}} = 2.7,\ 3.3,\ 3.8,$ and 4.3 GeV). Due to a large covariance between parameters, it is necessary to fix the pion and proton temperatures (T_π and T_p). Previous analyses have extracted these values using a two component fit (as mentioned in section 8.1, pions are fit with a two-component model to account for Δ resonance production and pair production, yet Eq. 9.8 only contains a Δ resonance production component) [55, 56]. The temperatures extracted from both refs. [55] and [56] were used with this model and the values from ref. [55] provided better fits and were therefore used for all energies. Reference [55] fit the temperatures linearly with $\sqrt{s_{NN}}$, and that linear fit was used to fix the temperatures employed in this analysis and for the recent HADES measurements [56] (values shown in Tab. 9.3). While these temperatures are not the same as those obtained from the fits of the pion spectra, the spectra fit models used by each experiment are different and therefore have differing interpretations of the temperature, so this method provides consistency by using a single method to obtain the temperatures and a single functional form to fit the data across all energies. Fixing the temperatures allows for the extraction of V_C and the initial pion ratio before modification due to the Coulomb potential, $\pi\text{Ratio}_{\text{init}}$, the latter being A^+/A^- from Eq. 9.8. Figure 9.2 shows the extracted Coulomb potential and initial pion ratio as a function of collision energy, with Tab. 9.3 showing the parameters used and corresponding uncertainties.

There is a clear trend of both V_C and $\pi\text{Ratio}_{\text{init}}$ as a function of collision energy, with the measurement at $\sqrt{s_{NN}} = 3$ GeV following that trend. Furthermore, the predicted pion ratios from sec. 9.1.1 can be compared to $\pi\text{Ratio}_{\text{init}}$, particularly the KaoS measurement at $\sqrt{s_{NN}} = 2.33$ GeV, which corresponds to a single beam kinetic energy of 1 AGeV. This is the energy at which the empirical prediction using the cross sections was made. The KaoS value of $\pi\text{Ratio}_{\text{init}}$ is $54.9 \pm 0.9\%$, which is compared to $(\pi^+/\pi^-)_{\text{CG}} = 56.5\%$ using the Clebsch-Gordan method, and $(\pi^+/\pi^-)_\sigma = 53.3\%$ using the cross section method. This demonstrates a very good agreement between this measurement and the predictions, indicating the validity of this model.

Additionally, trends across centrality can be observed for both V_C and $\pi\text{Ratio}_{\text{init}}$. However, since

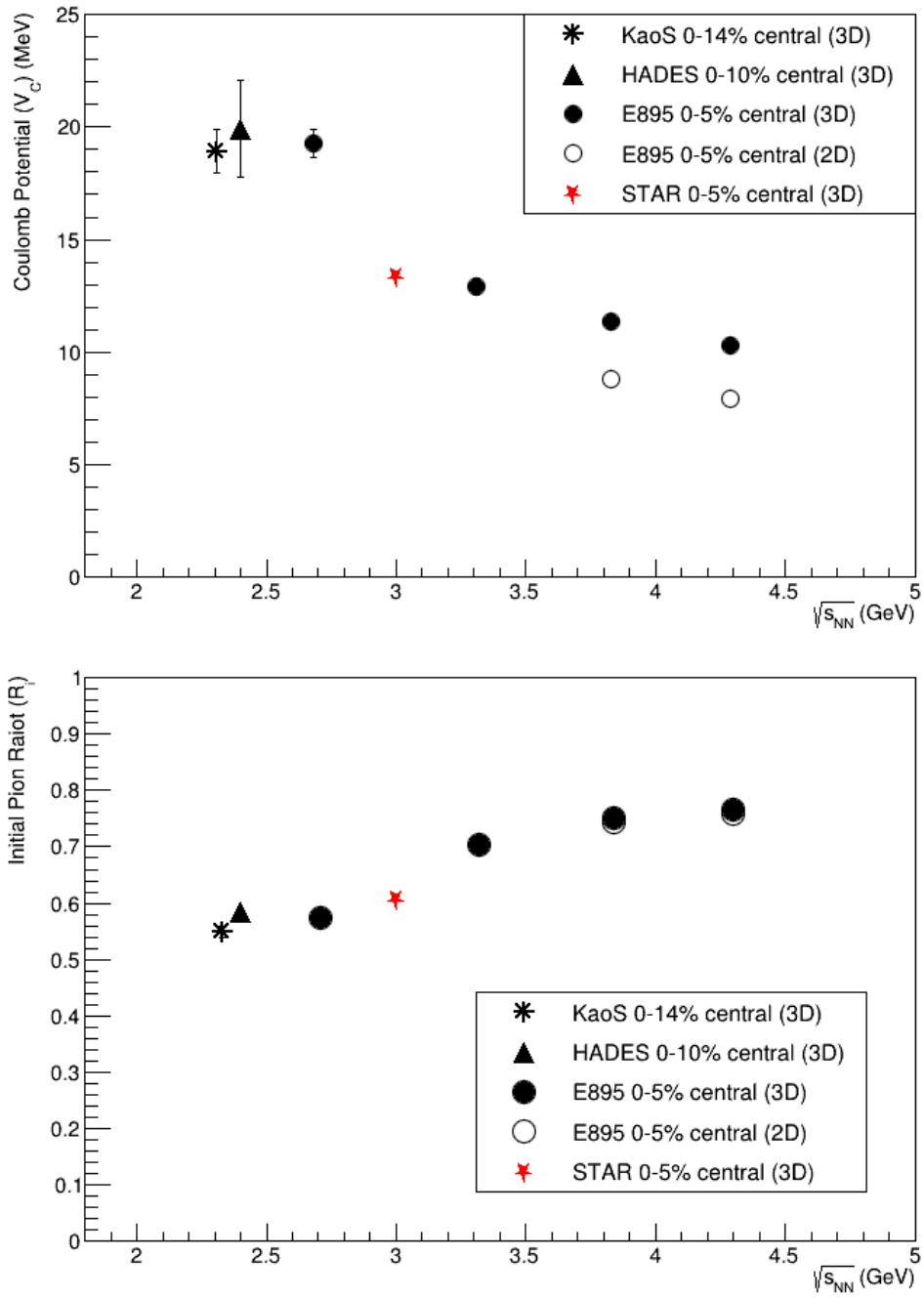

Figure 9.2: Measurements of the Coulomb potential, V_C, using Eq. 9.8 (top) and of the initial pion ratio, $\pi\text{Ratio}_{\text{init}}$, (bottom). To provide consistency of methodology, temperatures were fixed to those found in ref. [55]. The values of $\pi\text{Ratio}_{\text{init}}$ can be compared to the predictions from subsection 9.1.1 and are in good agreement.

Experiment	$\sqrt{s_{NN}}$ (GeV)	Dimensions	V_C (MeV)	$\pi\text{Ratio}_{\text{init}}$	T_π (MeV)	T_p (MeV)
KaoS	2.33	3	18.9 ± 0.9	$54.9 \pm 0.9\%$	73.1	180
HADES	2.4	3	19.9 ± 2.1	$58 \pm 2\%$	74	181.4
E895	2.7	3	19.3 ± 0.6	$57.5 \pm 0.6\%$	77.7	187
STAR	3.0	3	15.4 ± 0.1	$65.78 \pm 0.03\%$	81.4	192.7
E895	3.3	3	12.9 ± 0.4	$70.4 \pm 0.5\%$	84.8	198
E895	3.8	3	11.4 ± 0.3	$75.1 \pm 0.4\%$	89.6	206
E895	4.3	3	10.3 ± 0.3	$76.6 \pm 0.5\%$	93.4	212
E895	3.8	2	8.8 ± 0.2	$74.3 \pm 0.4\%$	89.6	206
E895	4.3	2	7.9 ± 0.3	$75.8 \pm 0.5\%$	93.4	212

Table 9.3: Parameters from fitting pion ratio model (Eq. 9.8) to data from experiments at various energies. The pion and proton temperatures, T_π and T_p, are fixed to a linear trend observed in ref. [55] and therefore have no associated uncertainty. The data from this analysis are highlighted in yellow.

previous measurements did not investigate the centrality dependence, the same method cannot be used to constrain the temperatures. Rather, T_π and T_p were set using the temperatures obtained from the spectral fits at midrapidity. The proton temperature comes from the systematic fit model of a thermal distribution as the kinetic temperature obtained from the nominal blast wave model fit has a very different interpretation which is not comparable to the pion temperature since they are different models. The pion temperature is also obtained from a thermal distribution, which provides consistency between the models used to obtain the pion and proton temperatures. Figure 9.3 shows the extracted Coulomb potential and initial pion ratio as a function of centrality for collisions at $\sqrt{s_{NN}} = 3$ GeV. Clear monotonic trends exist on both V_C and $\pi\text{Ratio}_{\text{init}}$ across centrality. The higher Coulomb potential in central collisions compared to peripheral ones is consistent with a similar trend in baryon stopping, which will be discussed further in section 9.3. The lower initial pion ratio in central collisions compared to peripheral ones suggest that peripheral collisions have a higher fraction of thermal pion production than central ones. This may hint that peripheral collisions are more thermalized and create more pion pairs in first-chance collisions, whereas central collisions have a larger chance for rescattering, making thermal pion production less likely and favoring Δ production, which is a larger fraction of the pion yield at low energies. It is perhaps impossible to answer this with one data set alone, so a future systematic study with the rest of the STAR

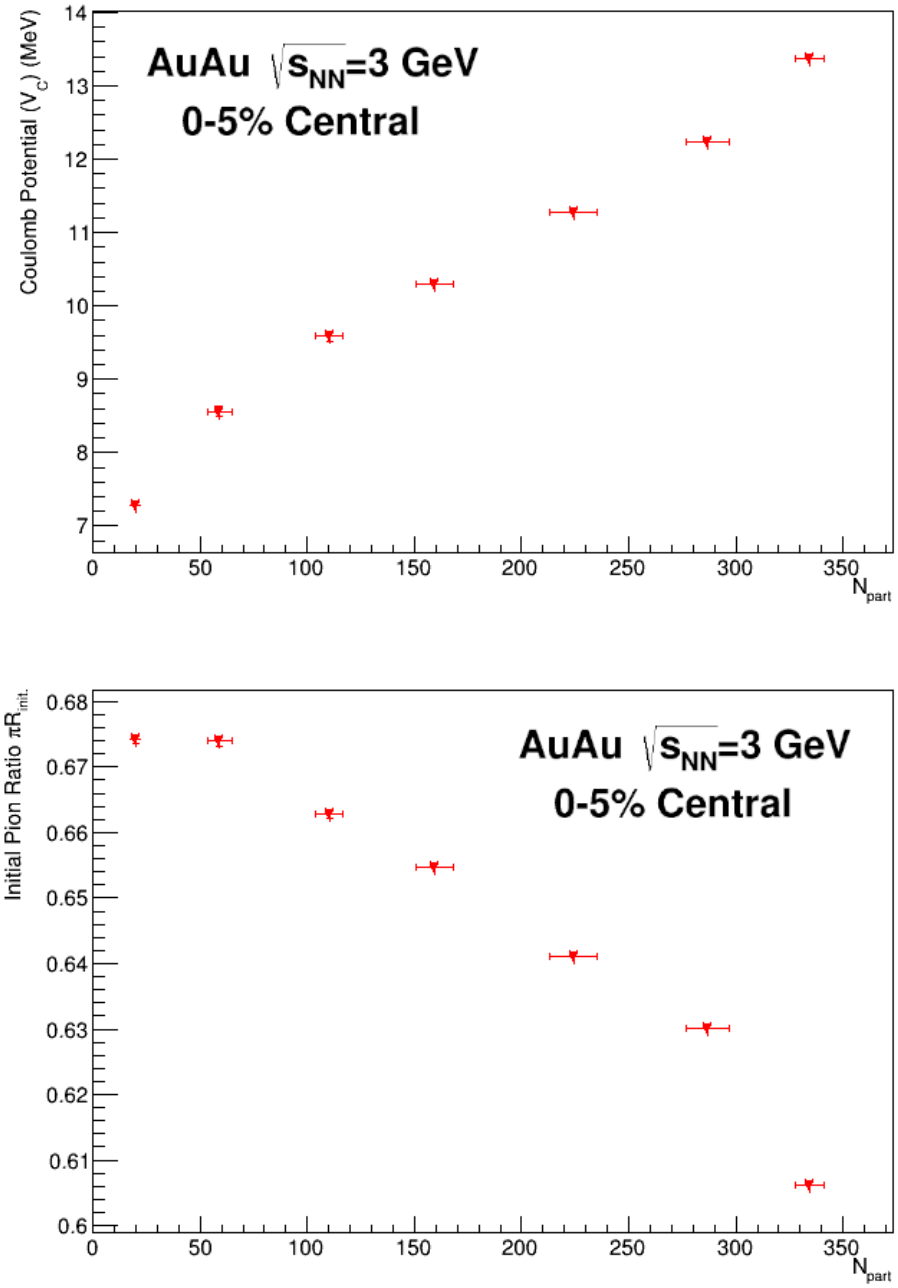

Figure 9.3: Measurements of the Coulomb potential, V_C, using Eq. 9.8 (top) and of the initial pion ratio, $\pi\text{Ratio}_{\text{init}}$, (bottom) as a function of number of participating nucleons $\sqrt{s_{NN}} = 3$ GeV. Unlike the measurements discussed above in Fig. 9.2 and Tab. 9.3, the pion and proton temperatures were fixed to the values obtained from the spectral fits. The vertical axes are both zero-suppressed.

fixed-target data sets will be essential for further understanding these trends.

9.2 Kaon Ratios

The nucleon carries a net strangeness of zero, so any strange hadron measured must have been produced during the interaction. The kaon is the lightest strange hadron, with a mass of 493.677 MeV [45]. However, in order to pair produce K^+ ($u\bar{s}$) and K^- ($\bar{u}s$), 987.354 MeV is required. Very few, if any, anti-baryons are created at this low energy, so it is easiest to put the $\bar{s}$ quark into the K^+ as it is the lightest strange hadron. The s quark can go into a K^-, or it can also go into a strange baryon through a process called associated production. The lightest strange baryon is the Λ, with a mass of 1115.683 MeV [45], which has an extra 177 MeV compared to a nucleon. It is therefore much more energetically favorable to excite a nucleon into a Λ and produce a kaon than it is to pair produce two kaons. This associated production process ($N + N \rightarrow \Lambda + K + N$) has a lower energy threshold than direct pair production of kaons and is expected to dominate at this energy. This associated production mechanism can create either a K^+ or a K^0, the exact details of which are shown in Tab. 9.4. This shows that K^+ and K^0 can both be created through this associated

Hadrons	Quarks
$p + p \rightarrow \Lambda + K^+ + p$	$uud + uud \rightarrow uds + u\bar{s} + uud$
$p + n \rightarrow \Lambda + K^+ + n$	$uud + udd \rightarrow uds + u\bar{s} + udd$
$p + n \rightarrow \Lambda + K^0 + p$	$uud + udd \rightarrow uds + d\bar{s} + uud$
$n + n \rightarrow \Lambda + K^0 + n$	$udd + udd \rightarrow uds + d\bar{s} + udd$

Table 9.4: Channels of associated production of a kaon with a Λ baryon.

production mechanism.

Although K^+ and K^0 have the same number of associated production channels, the neutrons to proton ratio indicates that they will not have the same yields. Taking the probability of $p + p$, $p + n/n + p$, and $n + n$ collisions as Z^2/A^2, $2Z(A - Z)/A^2$, and $(A - Z)^2/A^2$ respectively (where A is the atomic mass and Z is the atomic number of gold), the probability of producing a K^+ is approximately 0.4 while the probability of producing a K^0 is approximately 0.6. The yields of K^+

and K^0 produced through associated production with the Λ should add together to the Λ yield. This same type of mechanism is possible with the creation of $\bar{\Lambda} + K^-$, however it has a much higher energy threshold as it also requires the production of a baryon to conserve baryon number and so does not occur at this energy. This means that the only production mechanism for K^- at this energy is pair production with a K^+, while the K^+ has the same mechanism in addition to the associated production mechanism.

To understand the contribution of the different production mechanisms, a ratio of the yields of K^-/K^+ is constructed, as this will indicate the fraction of K^+ produced in pairs with K^-. The remaining K^+ yield then indicated the fraction that were produced in association with a Λ baryon. Figure 9.4 shows this ratio of midrapidity K^-/K^+ in 0-5% central collisions as a function of $\sqrt{s_{NN}}$. At $\sqrt{s_{NN}} = 3$ GeV, this ratio is 0.052, indicating that 5.2% of K^+ are pair produced with a K^- and the remaining 94.8% are produced in association with the Λ baryon. This measurement follows the trends between the measurements from KaoS at SIS18 and E866/E917 at the AGS. The associated production mechanism should turn off and be replaced by pair production of kaons once a high enough energy is reached, which may help to explain the "horn" seen by NA49 [32] in conjunction with the transition of primary pion production mechanism from the Δ resonance to pair production. The yield of K^+ through the associated production mechanism should increase until the energy threshold to consistently produce kaon pairs is reached; at that threshold, a drop in the K^+ yield is expected, giving rise to a horn-like feature.

9.3 Baryon Stopping

The ions, prior to collision, have all of their nucleons at target/beam rapidity. As the ions pass through each other, the participating nucleons interact and can lose energy. All of the initial energy was longitudinal, so it is natural to describe the loss of the initial energy with rapidity. The shift of the participating nucleons from beam/target rapidity is a way to measure this energy loss, called baryon stopping and indicated as δy, the shift of the participant proton peak from beam rapidity, in

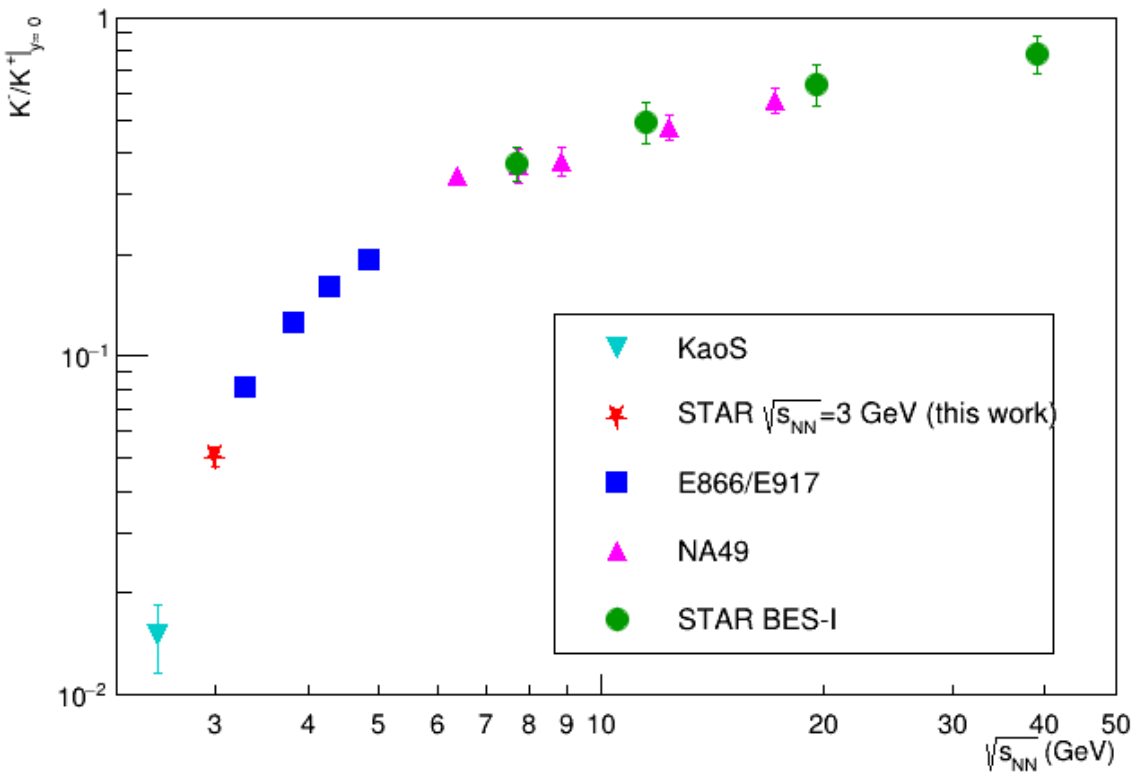

Figure 9.4: Ratio of midrapidity K^-/K^+ in 0-5% central A+A collisions as a function of $\sqrt{s_{NN}}$. This ratio indicates the fraction of K^+ which are pair produced with a K^-. The remaining K^+ are produced in association with a Λ baryon.

Fig. 9.5. The proton rapidity density distribution is sensitive to baryon stopping, particularly in these fixed-target collisions, as the acceptance of the STAR detector covers an entire half of rapidity space (mid- to target rapidity). This means that the stopped participants are well within the STAR acceptance and can be directly measured.

Various studies have previously been performed of baryon stopping and rapidity loss [57], indicating peaks in the proton distribution near beam rapidity and dips near midrapidity in peripheral collisions, with a sole peak at midrapidity in central collisions. Calculations indicate a change in the average rapidity loss across collision energy and centrality [58] and suggest a plateau around midrapidity at sufficiently high collisions energy [59]. This boost invariance around midrapidity was

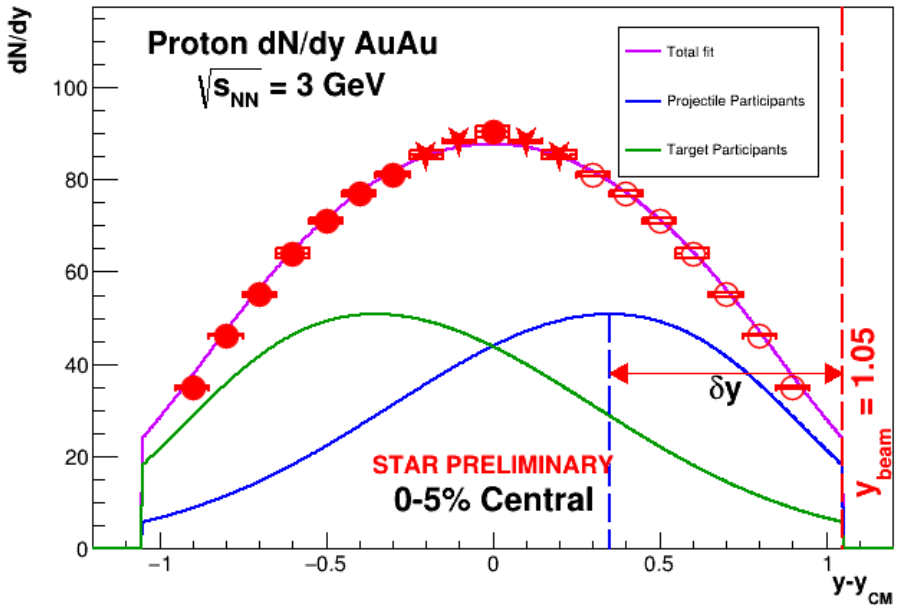

Figure 9.5: Proton rapidity density distribution in central $Au + Au$ collisions. The fit model is based off the number of collisions from a Monte Carlo Glauber Model and is used to identify the peak of the participant protons. The stopping, δy, is indicated as the shift of the participant proton peak from beam rapidity.

proposed by Bjorken [59] and has been an important insight for the field as higher collisions energies have been achieved and indicates that the midrapidity region is dominated by isotropic hadron production, with participating nucleons remaining near beam rapidity due to their transparency to each other. The question still remains, how do nucleons become transparent to each other? A number of theoretical calculations attempt to answer this using relativistic hydrodynamics [60, 61, 62, 63]. Landau proposed a non-boost invariant hydrodynamic model which agrees quite well with the current measurements [13, 60].

Extensions to the Landau hydrodynamics model have been made over the years, with more recent calculations indicating that the proton rapidity density distribution should be fit with the sum of two exponential distributions of the hyperbolic cosine of rapidity (i.e. $Ae^{-(1/\sigma)\cosh(y \pm y_{\text{shift}})}$), shifted in opposite directions from midrapidity to account for the baryon stopping [64]. This motivated the

functional form used to fit the proton rapidity density distributions in sec. 8.4, which are further used here to extract δy, although the exact functional form is different than that proposed by Ivanov [64]. The details of this model were discussed in section 8.4 as the same model was used to extrapolate the proton rapidity density distribution to obtain the full phase space yields. The model uses a distribution of the number of collisions undergone by each participant, obtained from a Monte Carlo Glauber Model, which is smoothed out using a Gaussian kernel, as seen in Fig. 8.21. A visual representation of δy can be seen in Fig. 9.5.

In this model, protons cannot be forward of beam rapidity nor backward of target rapidity, so hard cutoffs are implemented in the fit functions at those rapidity limits.

The trend in stopping as a function of center of mass energy is shown in Fig. 9.6. Previous

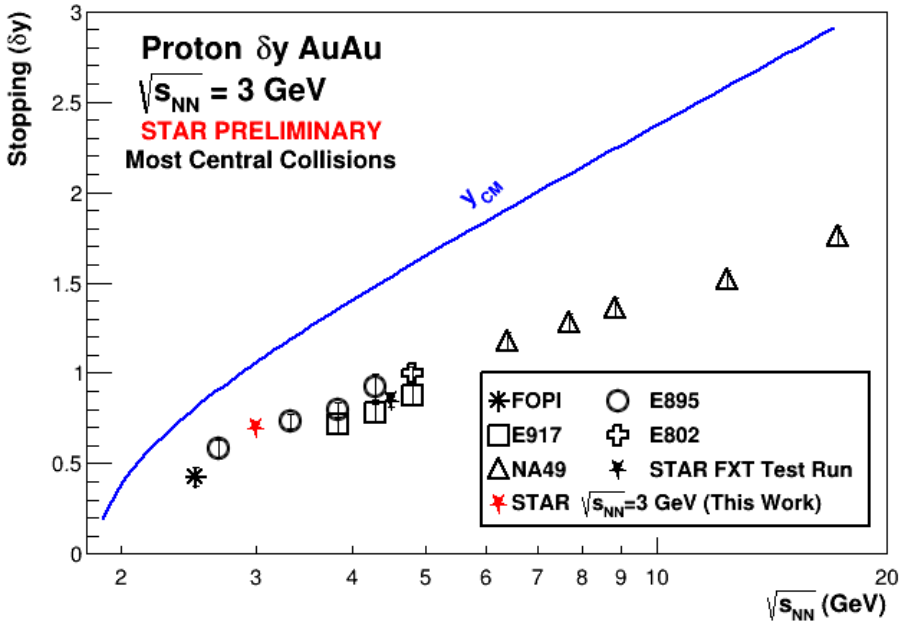

Figure 9.6: Baryon stopping in central $A + A$ collisions, given as the shift, δy, of the peak in the participant proton rapidity distribution from beam rapidity. The blue curve labeled y_{CM} indicated the shift of midrapidity from beam rapidity. Measurements from the AGS indicate a clear trend, with which these results from $\sqrt{s_{NN}} = 3$ GeV agree.

measurements of stopping used two Gaussians ranther than the method employed in this analysis;

however, the stopping obtained using Gaussians in the 0-5% centrality bin is within 5% of the value obtained using the method described in section 8.4. Theoretical calculations indicate that baryon stopping may be sensitive to the equation of state of the system and may help identify the order of the phase transition at high chemical potential [65]. While this measurement at $\sqrt{s_{NN}} = 3$ GeV may not independently prove the existence of a first-order phase transition, it lays the groundwork for a systematic study of stopping with the STAR fixed-target program using a single method for extracting the stopping. This program covers the energy range of $\sqrt{s_{NN}} = 3 - 13.7$ GeV and will cover the critical region between 4 and 6 GeV, where Fig. 9.6 shows a disagreement between measurements at the AGS, some of which may be indicating a dip in the stopping trend that may suggest a first-order phase transition or differences in the methods used to extract δy.

In addition to the trends across $\sqrt{s_{NN}}$, this analysis presents an extensive measurement of baryon stopping as a function of centrality. Many experiments at the AGS and SPS only performed measurements in central collisions, and while some centrality dependence of baryon stopping has been previously studied [57], such a large range of the centrality dependence of baryon stopping has never before been studied. Figure 9.7 shows the baryon stopping, δy, plotted against the average number of binary collisions divided by half the average number of participants, which represents the average number of collisions undergone by a single nucleon. The observed trend suggests a non-linear increase in the average rapidity based on the number of collisions undergone by each nucleon [58].

This method of plotting follows naturally from the model used to fit the proton rapidity density distributions and indicates an increase in the amount of rapidity loss for more central collisions where the number of collisions is higher. The exponential trend is an indication that each successive collision causes a larger rapidity loss than the previous one, resulting in a higher amount of stopping in central collisions than in peripheral ones. This exponential trend has never before been studied and requires further input from theorists to understand the implications. Furthermore, this trend is consistent with the trend observed in the Coulomb potential extracted from the pion ratio, which indicated a higher V_C in central collisions compared to peripheral ones, hinting at a larger fireball charge. A larger amount of stopped protons in central collisions would cause this increase of the

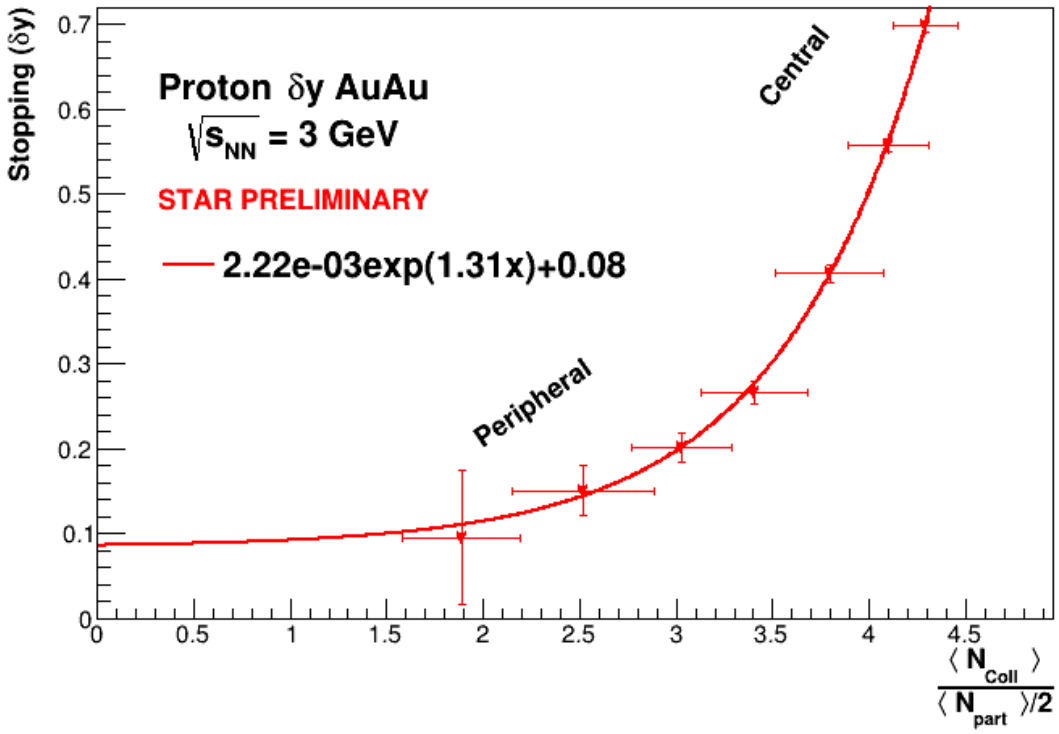

Figure 9.7: Baryon stopping as a function of centrality in $Au + Au$ collisions at $\sqrt{s_{NN}} = 3$ GeV. Stopping, δy, is plotted against the average number of binary collisions divided by half the average number of participants, representing the average number of collisions undergone by a single nucleon. The exponential trend is an indication that each successive collision causes a larger rapidity loss than the previous one.

fireball charge, as such charge comes primarily from protons. Future studies at higher collision energies from the STAR BES-II and FXT programs will help to identify how this trend changes as a function of collision energy.

Chapter 10

Conclusions

The primary goals of this dissertation, to measure the spectra and yields of $\pi^{\pm}$, $K^{\pm}$, and p in STAR fixed-target collisions at $\sqrt{s_{NN}} = 3$ GeV, have been accomplished. Transverse mass spectra as a function of rapidity and centrality have been presented along with rapidity density and mean transverse momentum distributions as a function of centrality. This marks the first measurements of charged kaons away from midrapidity in the AGS energy range along with the first measurements of the centrality dependence of hadrons in the same energy range.

The particle production mechanisms of each hadron were investigated in detail. Pions are produced primarily through the Δ resonance, though pair production does contribute to their yields. Positively charged kaons are produced almost exclusively ($\sim 95\%$) in association with a Λ, with the rest produced in pairs with a K^-. This associated production mechanism may be the source of the peak in the "horn" observed by NA49 (see Fig. 1.7) rather than the onset of deconfinement as argued by NA49, though further experimental measurements, with theoretical input, would be needed to confirm this. The observed protons are almost exclusively participants from the original nuclei, as evidenced by their rapidity density distributions showing strong indications of baryon stopping.

The ratio of pions has been used to extract the Coulomb potential of the fireball and the initial pion ratio before such modification. Predictions using Clebsch-Gordan coefficients and measured pion cross sections provide limits to the initial pion ratio, which are consistent with the value extracted from KaoS using the same model. Additionally, centrality trends in the Coulomb potential and

initial pion ratio show a monotonic behavior consistent with the expectations of a smaller fireball in more peripheral collisions.

Proton rapidity density distributions were used to investigate baryon stopping, with the first measurements across centrality. The model developed for this analysis to fit the proton rapidity density distribution is physics-based and uses the number of collisions undergone by each participant, which assumes an average rapidity loss per collision. The results of this model are very consistent with previous measurements in central collisions and the minimum-bias data set allowed this analysis to extend to more peripheral collisions. The observed trends in centrality indicate an exponential relationship between the rapidity loss from stopping and the average number of collisions per participant, suggesting that more collisions cause a larger average rapidity loss. This may be explained by each successive collision being at a lower energy than the previous, which could cause a larger rapidity loss for successive collisions. These results are also consistent with those from the Coulomb potential analysis, indicating a larger charge in the midrapidity region in central collisions compared to peripheral ones due to the primarily proton content of the fireball.

While this analysis alone does not characterize the QGP nor the phase transition between it and a hadron gas, it lays out a systematic manner in which other energies in the STAR FXT and BES-II programs can be analyzed. Trends across centrality and energy in the hadron yields may be sensitive to the phase transition, as may the trend in baryon stopping. The author hopes that others will build on this analysis and measure the energy and centrality trends in these observables.

Appendix A

Coulomb-correction Jacobians

In this appendix, the Jacobians, $J^{\pm}$ and $J^{\pm}_{\text{eff}}$, used in the Coulomb correction for pions will be derived. First, $J^{\pm}$ will be derived, which accounts for the switch between initial and final coordinates, followed by $J^{\pm}_{\text{eff}}$, which accounts for the use of the effective potential. The Jacobian itself is truly the determinant of the Jacobian matrix, which is comprised of the partial derivatives of the initial variables with respect to the final ones [66].

Equation 9.2 introduced the relationship between the initial and final pion energies through the Coulomb potential. If V_C is constant with respect to energy, then $dE_i = dE_f$; however, these energies are functions of momentum and $dp_i \neq dp_f$, which is where $J^{\pm}$ originates. Momentum is three-dimensional, so it must be written in the proper coordinates, which would be p_{total}, p_T, and ϕ, but these must be obtained from Cartesian coordinates

$$p_{\text{total}} = \sqrt{p_x^2 + p_y^2 + p_z^2} \qquad p_T = \sqrt{p_x^2 + p_y^2} \qquad \phi = \arcsin p_y/p_T. \tag{A.1}$$

The first step is to convert the 3D differential $dp_x dp_y dp_z \rightarrow dp_{\text{total}} dp_T d\phi$ using an intermediate

Jacobian, J_{coord},

$$J_{\text{coord}} = \begin{vmatrix} \frac{dp_x}{dp_{\text{total}}} & \frac{dp_x}{dp_T} & \frac{dp_x}{d\phi} \\ \frac{dp_y}{dp_{\text{total}}} & \frac{dp_y}{dp_T} & \frac{dp_y}{d\phi} \\ \frac{dp_z}{dp_{\text{total}}} & \frac{dp_z}{dp_T} & \frac{dp_z}{d\phi} \end{vmatrix} = \begin{vmatrix} \frac{p_{\text{total}}}{p_x} & \cos\phi & -p_T \sin\phi \\ \frac{p_{\text{total}}}{p_y} & \sin\phi & p_T \cos\phi \\ \frac{p_{\text{total}}}{p_z} & 0 & 0 \end{vmatrix} = \frac{p_{\text{total}} p_T}{\sqrt{p_{\text{total}}^2 - p_T^2}}. \tag{A.2}$$

It follows that

$$dp_x dp_y dp_z = \frac{p_{\text{total}} p_T}{\sqrt{p_{\text{total}}^2 - p_T^2}} dp_{\text{total}} dp_T d\phi.$$

The energies are functions of the total energy, so p_T and ϕ can be integrated out

$$\begin{aligned} dp_{\text{total}} &= \int_0^{2\pi} \int_0^{p_{\text{total}}} \frac{p_{\text{total}} p_T}{\sqrt{p_{\text{total}}^2 - p_T^2}} dp_{\text{total}} dp_T d\phi \\ &= 2\pi p_{\text{total}} dp_{\text{total}} \int_0^{p_{\text{total}}} \frac{p_T}{\sqrt{p_{\text{total}}^2 - p_T^2}} dp_T \\ &= -2\pi p_{\text{total}} \sqrt{p_{\text{total}}^2 - p_T^2} \Big|_0^{p_{\text{total}}} dp_{\text{total}} \\ &= 2\pi p_{\text{total}}^2 dp_{\text{total}}. \end{aligned} \tag{A.3}$$

Next, $J^{\pm}$ can be written

$$J^{\pm} = \frac{d^3 p_i}{d^3 p_f} = \frac{2\pi p_{i,\text{total}}^2 dp_{i,\text{total}}}{2\pi p_{f,\text{total}}^2 dp_{f,\text{total}}} = \frac{p_{i,\text{total}}^2}{p_{f,\text{total}}^2} \frac{dp_{i,\text{total}}}{dp_{f,\text{total}}} = \frac{p_{i,\text{total}}^2}{p_{f,\text{total}}^2} \frac{dp_{i,\text{total}}}{dE_f} \frac{dE_f}{dp_{f,\text{total}}}. \tag{A.4}$$

The final energy, E_f, can trivially be written as

$$E_f = \sqrt{p_{f,\text{total}}^2 + m^2}. \tag{A.5}$$

The initial momentum, $p_{i,\text{total}}$, also can be written in terms of E_f with a little more work

$$\begin{aligned} E_i &= E_f \mp V_C \\ \sqrt{p_{i,\text{final}}^2 + m^2} &= E_f \mp V_C \\ p_{i,\text{final}}^2 + m^2 &= (E_f \mp V_C)^2 \\ p_{i,\text{final}} &= \sqrt{(E_f \mp V_C)^2 - m^2}. \end{aligned} \tag{A.6}$$

Now these derivatives can be taken:

$$\frac{dp_{i,\text{final}}}{dE_f} = \frac{E_f \mp V_C}{\sqrt{(E_f \mp V_C)^2 - m^2}} = \frac{E_i}{p_{i\text{final}}}, \tag{A.7}$$

and

$$\frac{dE_f}{dp_{f,\text{final}}} = \frac{p_{f,\text{final}}}{\sqrt{p_{f,\text{total}}^2 + m^2}} = \frac{p_{f,\text{total}}}{E_f}. \tag{A.8}$$

Plugging Eqs. A.7 and A.8 into Eq. A.4 gives the total Jacobian,

$$J^{\pm} = \frac{p_{i,\text{total}}^2}{p_{f,\text{total}}^2} \frac{E_i}{p_{i\text{final}}} \frac{p_{f,\text{total}}}{E_f} = \frac{p_{i,\text{total}} E_i}{p_{f,\text{total}} E_f}. \tag{A.9}$$

The effective Jacobian, $J_{\text{eff}}^{\pm}$, can be obtained in a similar manner by taking Eq. 9.2 and replacing V_C with $V_{\text{eff}}(E_f)$. The following derivation follows from that done in ref. [56]. The Jacobian previously derived, $J^{\pm}$, is still valid as the same conversion from initial to final momentum must occur, however, the previous assumption that $dE_i = dE_f$ is now false. Instead,

$$J_{\text{eff}}^{\pm} = \frac{dE_i}{dE_f} = \frac{d(E_f \mp V_{\text{eff}}(E_f))}{dE_f} = 1 \mp \frac{dV_{\text{eff}}(E_f)}{dE_f}, \tag{A.10}$$

which is a one-dimensional Jacobian matrix and therefore identically defines the determinant. Taking this derivative

$$\frac{dV_{\text{eff}}}{dE_f} = \frac{dV_{\text{eff}}}{dx} \frac{dx}{dE_f} = \frac{dV_{\text{eff}}}{dx} \frac{dx}{dE_{\max}} \frac{dE_{\max}}{dE_f}, \tag{A.11}$$

the chain rule must be used. This gives,

$$\frac{dE_{\max}}{dE_f} = \frac{m_p}{m_\pi}, \tag{A.12}$$

$$\frac{dx}{dE_{\max}} = \frac{x}{2E_{\max}} = \frac{1}{T_p}\frac{1}{2x}, \tag{A.13}$$

and

$$\frac{dV_{\text{eff}}}{dx} = \begin{cases} 2V_C x e^{-x^2} & \text{for 2D expansion,} \\ \frac{4}{\sqrt{\pi}} V_C x^2 e^{-x^2} & \text{for 3D expansion.} \end{cases} \tag{A.14}$$

Combining these together gives

$$\frac{dV_{\text{eff}}}{dE_f} = \begin{cases} V_C \frac{m_p}{m_\pi T_p} e^{-x^2} & \text{for 2D expansion,} \\ V_C \frac{2m_p}{\sqrt{\pi} m_\pi T_p} x e^{-x^2} & \text{for 3D expansion.} \end{cases} \tag{A.15}$$

Finally, this goes into Eq. A.10 to give

$$J^{\pm}_{\text{eff}} = \begin{cases} 1 \mp V_C \frac{m_p}{m_\pi T_p} e^{-x^2} & \text{for 2D expansion,} \\ 1 \mp V_C \frac{2m_p}{\sqrt{\pi} m_\pi T_p} x e^{-x^2} & \text{for 3D expansion.} \end{cases} \tag{A.16}$$

Bibliography

[1] Planck Collaboration, Aghanim, N., et al. *Planck 2018 results - VI. Cosmological parameters.* A&A **641**, A6 (2020). doi:10.1051/0004-6361/201833910. URL https://doi.org/10.1051/0004-6361/201833910.

[2] E. Rutherford. *The Scattering of α and β Particles by Matter and the Structure of the Atom.* Philosophical Magazine **21**, 669–688 (1911).

[3] E. Rutherford. *LIV. Collision of α particles with light atoms. IV. An anomalous effect in nitrogen.* The London, Edinburgh, and Dublin Philosophical Magazine and Journal of Science **37** (222), 581–587 (1919). doi:10.1080/14786440608635919. https://doi.org/10.1080/14786440608635919, URL https://doi.org/10.1080/14786440608635919.

[4] J. Chadwick. *The existence of a neutron.* Proceedings of the Royal Society of London. Series A, Containing Papers of a Mathematical and Physical Character **136** (830), 692–708 (1932). doi:10.1098/rspa.1932.0112. https://royalsocietypublishing.org/doi/pdf/10.1098/rspa.1932.0112, URL https://royalsocietypublishing.org/doi/abs/10.1098/rspa.1932.0112.

[5] H. Yukawa. *On the Interaction of Elementary Particles. I.* Proceedings of the Physico-Mathematical Society of Japan. 3rd Series **17**, 48–57 (1935). doi:10.11429/ppmsj1919.17.0_48.

[6] M. Gell-Mann. *The Eightfold Way: a theory of strong interaction symmetry* (1961). doi:10.2172/4008239. URL https://www.osti.gov/biblio/4008239.

[7] M. Gell-Mann. *A schematic model of baryons and mesons.* Phys. Lett. **8** (3), 214–215 (1964). ISSN 0031-9163. doi:https://doi.org/10.1016/S0031-9163(64)92001-3. URL https://www.sciencedirect.com/science/article/pii/S0031916364920013.

[8] B. V. Struminsky. *Magnetic moments of baryons in the quark model.* JINR publication P-1939 (1965). Dubna.

[9] F. Tkachov. *A contribution to the history of quarks: Boris Struminsky's 1965 JINR publication* (2009). doi:10.48550/ARXIV.0904.0343. URL https://arxiv.org/abs/0904.0343.

[10] M. Y. Han and Y. Nambu. *Three-Triplet Model with Double* SU(3) *Symmetry.* Phys. Rev. **139**, B1006–B1010 (1965). doi:10.1103/PhysRev.139.B1006. URL https://link.aps.org/doi/10.1103/PhysRev.139.B1006.

[11] O. W. Greenberg. *Spin and Unitary-Spin Independence in a Paraquark Model of Baryons and Mesons.* Phys. Rev. Lett. **13**, 598–602 (1964). doi:10.1103/PhysRevLett.13.598. URL https://link.aps.org/doi/10.1103/PhysRevLett.13.598.

[12] E. Fermi. *High Energy Nuclear Events.* Progress of Theoretical Physics **5** (4), 570–583 (1950). ISSN 0033-068X. doi:10.1143/ptp/5.4.570. https://academic.oup.com/ptp/article-pdf/5/4/570/5430247/5-4-570.pdf, URL https://doi.org/10.1143/ptp/5.4.570.

[13] L. D. Landau. *On the multiparticle production in high-energy collisions.* Izv. Akad. Nauk Ser. Fiz. **17**, 51–64 (1953).

[14] R. Hagedorn and J. Rafelski. *Hot hadronic matter and nuclear collisions.* Phys. Lett. B **97** (1), 136–142 (1980). ISSN 0370-2693. doi:https://doi.org/10.1016/0370-2693(80)90566-3. URL https://www.sciencedirect.com/science/article/pii/0370269380905663.

[15] STAR Collaboration, M. M. Aggarwal, et al. *An Experimental Exploration of the QCD Phase Diagram: The Search for the Critical Point and the Onset of De-confinement* (2010). doi:10.48550/ARXIV.1007.2613. URL https://arxiv.org/abs/1007.2613.

[16] STAR Collaboration. *Studying the Phase Diagram of QCD matter* (2014). URL https://drupal.star.bnl.gov/STAR/files/BES_WPII_ver6.9_Cover.pdf.

[17] T. Matsui and H. Satz. *J/ψ suppression by quark-gluon plasma formation.* Phys. Lett. B **178** (4), 416–422 (1986). ISSN 0370-2693. doi:https://doi.org/10.1016/0370-2693(86)91404-8. URL https://www.sciencedirect.com/science/article/pii/0370269386914048.

[18] V. Khachatryan, A. Sirunyan, et al. (CMS). *Suppression of Υ(1S), Υ(2S), and Υ(3S) quarkonium states in PbPb collisions at $\sqrt{s_{NN}} = 2.76$ TeV.* Phys. Lett. B **770**, 357–379 (2017). ISSN 0370-2693. doi:https://doi.org/10.1016/j.physletb.2017.04.031. URL https://www.sciencedirect.com/science/article/pii/S0370269317303052.

[19] *Observation of the Υ(3S) meson and sequential suppression of Υ states in PbPb collisions at $\sqrt{s_{NN}} = 5.02$ TeV* (2022). CMS PAS HIN-21-007, URL https://cds.cern.ch/record/2805926/files/HIN-21-007-pas.pdf.

[20] M. Connors, C. Nattrass, et al. *Jet measurements in heavy ion physics.* Rev. Mod. Phys. **90**, 025005 (2018). doi:10.1103/RevModPhys.90.025005. URL https://link.aps.org/doi/10.1103/RevModPhys.90.025005.

[21] C. Manuel. *The Stopping Power of Hot Nuclear Matter.* https://physics.aps.org/articles/v7/97 (2014). [Online; accessed 21-October-2022].

[22] J. Adams, M. Aggarwal, et al. *Experimental and theoretical challenges in the search for the quark–gluon plasma: The STAR Collaboration's critical assessment of the evidence from RHIC collisions.* Nuclear Physics A **757** (1), 102–183 (2005). ISSN 0375-9474. doi:https://doi.org/10.1016/j.nuclphysa.2005.03.085. First Three Years of Operation of RHIC, URL https://www.sciencedirect.com/science/article/pii/S0375947405005294.

[23] M. Gyulassy and L. McLerran. *New forms of QCD matter discovered at RHIC.* Nuclear Physics A **750** (1), 30–63 (2005). ISSN 0375-9474. doi:https://doi.org/10.1016/j.nuclphysa.2004.10.034.

Quark-Gluon Plasma. New Discoveries at RHIC: Case for the Strongly Interacting Quark-Gluon Plasma. Contributions from the RBRC Workshop held May 14-15, 2004, URL https://www.sciencedirect.com/science/article/pii/S0375947404011480.

[24] U. Heinz and R. Snellings. *Collective Flow and Viscosity in Relativistic Heavy-Ion Collisions*. Annual Review of Nuclear and Particle Science **63** (1), 123–151 (2013). doi:10.1146/annurev-nucl-102212-170540. https://doi.org/10.1146/annurev-nucl-102212-170540, URL https://doi.org/10.1146/annurev-nucl-102212-170540.

[25] M. Abdallah, B. Aboona, et al. *Disappearance of partonic collectivity in* $\sqrt{s_{NN}} = 3$ *GeV Au+Au collisions at RHIC*. Phys. Lett. B **827**, 137003 (2022). ISSN 0370-2693. doi:https://doi.org/10.1016/j.physletb.2022.137003. URL https://www.sciencedirect.com/science/article/pii/S037026932200137X.

[26] L. Adamczyk, J. K. Adkins, et al. (STAR Collaboration). *Centrality and Transverse Momentum Dependence of Elliptic Flow of Multistrange Hadrons and* ϕ *Meson in* Au + Au *Collisions at* $\sqrt{s_{NN}} = 200$ GeV. Phys. Rev. Lett. **116**, 062301 (2016). doi:10.1103/PhysRevLett.116.062301. URL https://link.aps.org/doi/10.1103/PhysRevLett.116.062301.

[27] A. Bazavov, H.-T. Ding, et al. *QCD equation of state to* $\mathcal{O}(\mu_B^6)$ *from lattice QCD*. Phys. Rev. D **95**, 054504 (2017). doi:10.1103/PhysRevD.95.054504. URL https://link.aps.org/doi/10.1103/PhysRevD.95.054504.

[28] M. A. Halasz, A. D. Jackson, et al. *Phase diagram of QCD*. Phys. Rev. D **58**, 096007 (1998). doi:10.1103/PhysRevD.58.096007. URL https://link.aps.org/doi/10.1103/PhysRevD.58.096007.

[29] Y. Hatta and M. A. Stephanov. *Proton-Number Fluctuation as a Signal of the QCD Critical End Point*. Phys. Rev. Lett. **91**, 102003 (2003). doi:10.1103/PhysRevLett.91.102003. URL https://link.aps.org/doi/10.1103/PhysRevLett.91.102003.

[30] W.-j. Fu, X. Luo, et al. *Hyper-order baryon number fluctuations at finite temperature and density.* Phys. Rev. D **104**, 094047 (2021). doi:10.1103/PhysRevD.104.094047. URL https://link.aps.org/doi/10.1103/PhysRevD.104.094047.

[31] J. Rafelski and B. Müller. *Strangeness Production in the Quark-Gluon Plasma.* Phys. Rev. Lett. **48**, 1066–1069 (1982). doi:10.1103/PhysRevLett.48.1066. URL https://link.aps.org/doi/10.1103/PhysRevLett.48.1066.

[32] M. Gaździki and M. I. Gorenstein. *On the early stage of Nucleus-Nucleus Collisions.* Acta Phys. Pol. B **30** (9), 2705 (1999). URL https://www.actaphys.uj.edu.pl/R/30/9/2705.

[33] R. Critelli, J. Noronha, et al. *Critical point in the phase diagram of primordial quark-gluon matter from black hole physics.* Phys. Rev. D **96**, 096026 (2017). doi:10.1103/PhysRevD.96.096026. URL https://link.aps.org/doi/10.1103/PhysRevD.96.096026.

[34] J. L. Klay, N. N. Ajitanand, et al. (E895 Collaboration). *Charged pion production in* $2A$ *to* $8A$ *GeV central Au + Au Collisions.* Phys. Rev. C **68**, 054905 (2003). doi:10.1103/PhysRevC.68.054905. URL https://link.aps.org/doi/10.1103/PhysRevC.68.054905.

[35] J. L. Klay, N. N. Ajitanand, et al. (E895 Collaboration). *Longitudinal Flow of Protons from* $(2 - -8)A$GeV *Central Au + Au Collisions.* Phys. Rev. Lett. **88**, 102301 (2002). doi:10.1103/PhysRevLett.88.102301. URL https://link.aps.org/doi/10.1103/PhysRevLett.88.102301.

[36] L. Ahle, Y. Akiba, et al. *An excitation function of* K^- *and* K^+ *production in Au+Au reactions at the AGS.* Phys. Lett. B **490** (1), 53–60 (2000). ISSN 0370-2693. doi:https://doi.org/10.1016/S0370-2693(00)00916-3. URL https://www.sciencedirect.com/science/article/pii/S0370269300009163.

[37] C. Montag. *RHIC status and plans.* AIP Conference Proceedings **2160** (1), 040006 (2019). doi:10.1063/1.5127686. https://aip.scitation.org/doi/pdf/10.1063/1.5127686, URL https://aip.scitation.org/doi/abs/10.1063/1.5127686.

[38] H. Hahn, E. Forsyth, et al. *The RHIC Design Overview*. Nucl. Instrum. Meth. A **499** (2), 245–263 (2003). ISSN 0168-9002. doi:https://doi.org/10.1016/S0168-9002(02)01938-1. The Relativistic Heavy Ion Collider Project: RHIC and its Detectors, URL https://www.sciencedirect.com/science/article/pii/S0168900202019381.

[39] C. Gardner et al. *Setup and Performance of the RHIC Injector Accelerators for the 2007 Run with Gold Ions*. In *Proc. 22th Particle Accelerator Conference (PAC07), Albuquerque, NM, USA, June 25-29, 2007*, number 22 in Particle Accelerator Conference, pages 1862–1864. JACoW, Geneva, Switzerland (2007). ISBN 1-4244-0917-9. URL http://accelconf.web.cern.ch/p07/PAPERS/TUPAS096.PDF.

[40] C. Gardner et al. *Operation of the RHIC Injector Chain with Ions from EBIS*. In *Proc. 6th International Particle Accelerator Conference (IPAC'15), Richmond, VA, USA, May 3-8, 2015*, number 6 in International Particle Accelerator Conference, pages 3804–3807. JACoW, Geneva, Switzerland (2015). ISBN 978-3-95450-168-7. doi:https://doi.org/10.18429/JACoW-IPAC2015-THPF046. URL http://jacow.org/ipac2015/papers/thpf046.pdf.

[41] J. Alessi, D. Barton, et al. *Electron Beam Ion Source Preinjector Project (EBIS) Conceptual Design Report*. Technical report, Brookhaven National Laboratory (2005). doi:10.2172/15016043. URL https://www.osti.gov/biblio/15016043.

[42] K. Ackermann, N. Adams, et al. *STAR detector overview*. Nulc. Instrum. Meth. A **499** (2), 624–632 (2003). ISSN 0168-9002. doi:https://doi.org/10.1016/S0168-9002(02)01960-5. The Relativistic Heavy Ion Collider Project: RHIC and its Detectors, URL https://www.sciencedirect.com/science/article/pii/S0168900202019605.

[43] A. Schmah. *Collaboration Communications*.

[44] M. Anderson, J. Berkovitz, et al. *The STAR time projection chamber: a unique tool for studying high multiplicity events at RHIC*. Nucl. Instrum. Meth. A **499** (2), 659–678 (2003). ISSN 0168-9002. doi:https://doi.org/10.1016/S0168-9002(02)01964-2. The Relativistic Heavy Ion

Collider Project: RHIC and its Detectors, URL https://www.sciencedirect.com/science/article/pii/S0168900202019642.

[45] R. L. Workman and Others (Particle Data Group). *Review of Particle Physics*. PTEP **2022**, 083C01 (2022). doi:10.1093/ptep/ptac097.

[46] H. Bichsel. *A method to improve tracking and particle identification in TPCs and silicon detectors*. Nucl. Instrum. Meth. A **562** (1), 154–197 (2006). ISSN 0168-9002. doi:https://doi.org/10.1016/j.nima.2006.03.009. URL https://www.sciencedirect.com/science/article/pii/S0168900206005353.

[47] H. Bichsel. *Comparison of Bethe-Bloch and Bichsel Functions*. STAR Note SN0439, URL https://drupal.star.bnl.gov/STAR/starnotes/public/sn0439.

[48] P. Fachini et al. *Proposal for a Large Area Time of Flight System for STAR* (2004). STAR Note SN0621, URL https://drupal.star.bnl.gov/STAR/files/tof-5-24-2004.pdf.

[49] F. Geurts, M. Shao, et al. *Performance of the prototype MRPC detector for STAR*. Nucl. Instrum. Meth. A **533** (1), 60–64 (2004). ISSN 0168-9002. doi:https://doi.org/10.1016/j.nima.2004.07.001. Proceedings of the Seventh International Workshop on Resistive Plate Chambers and Related Detectors, URL https://www.sciencedirect.com/science/article/pii/S0168900204014056.

[50] M. S. Abdallah, J. Adam, et al. (STAR Collaboration). *Flow and interferometry results from* Au + Au *collisions at* $\sqrt{s_{NN}} = 4.5$ *GeV*. Phys. Rev. C **103**, 034908 (2021). doi:10.1103/PhysRevC.103.034908. URL https://link.aps.org/doi/10.1103/PhysRevC.103.034908.

[51] J. R. Taylor. *Classical mechanics*. Univ. Science Books (2005). ISBN 978-1891389221.

[52] E. Schnedermann, J. Sollfrank, and U. Heinz. *Thermal phenomenology of hadrons from 200A GeV S+S collisions*. Phys. Rev. C **48**, 2462–2475 (1993). doi:10.1103/PhysRevC.48.2462. URL https://link.aps.org/doi/10.1103/PhysRevC.48.2462.

[53] L. Adamczyk, J. K. Adkins, et al. (STAR Collaboration). *Bulk properties of the medium produced in relativistic heavy-ion collisions from the beam energy scan program.* Phys. Rev. C **96**, 044904 (2017). doi:10.1103/PhysRevC.96.044904. URL https://link.aps.org/doi/10.1103/PhysRevC.96.044904.

[54] B. J. VerWest and R. A. Arndt. NN *single pion production cross sections below 1500 MeV.* Phys. Rev. C **25**, 1979–1985 (1982). doi:10.1103/PhysRevC.25.1979. URL https://link.aps.org/doi/10.1103/PhysRevC.25.1979.

[55] D. Cebra, S. G. Brovko, et al. *Coulomb effect in Au+Au and Pb+Pb collisions as a function of collision energy* (2014). doi:10.48550/ARXIV.1408.1369. URL https://arxiv.org/abs/1408.1369.

[56] J. Adamczewski-Musch et al. (HADES). *Impact of the Coulomb field on charged-pion spectra in few-GeV heavy-ion collisions.* Eur. Phys. J. A **58** (9), 166 (2022). doi:10.1140/epja/s10050-022-00796-6. 2202.12750.

[57] B. B. Back, R. R. Betts, et al. (E917 Collaboration). *Baryon Rapidity Loss in Relativistic $Au + Au$ Collisions.* Phys. Rev. Lett. **86**, 1970–1973 (2001). doi:10.1103/PhysRevLett.86.1970. URL https://link.aps.org/doi/10.1103/PhysRevLett.86.1970.

[58] F. Videbæk and O. Hansen. *Baryon rapidity loss and midrapidity stacking in high energy nucleus-nucleus collisions.* Phys. Rev. C **52**, 2684–2693 (1995). doi:10.1103/PhysRevC.52.2684. URL https://link.aps.org/doi/10.1103/PhysRevC.52.2684.

[59] J. D. Bjorken. *Highly relativistic nucleus-nucleus collisions: The central rapidity region.* Phys. Rev. D **27**, 140–151 (1983). doi:10.1103/PhysRevD.27.140. URL https://link.aps.org/doi/10.1103/PhysRevD.27.140.

[60] S. Z. Belen'kji and L. D. Landau. *Hydrodynamic theory of multiple production of particles.* Il Nuovo Cimento (1955-1965) **3** (1), 15–31 (1956). ISSN 1827-6121. doi:10.1007/BF02745507. URL https://doi.org/10.1007/BF02745507.

[61] W. Busza and A. S. Goldhaber. *Nuclear stopping power*. Physics Letters B **139** (4), 235–238 (1984). ISSN 0370-2693. doi:https://doi.org/10.1016/0370-2693(84)91070-0. URL https://www.sciencedirect.com/science/article/pii/0370269384910700.

[62] R. Beckmann, S. Raha, et al. *Limiting Fragmentation and Transparency in High Energy Heavy Ion Collisions*. Physica Scripta **29** (3), 197 (1984). doi:10.1088/0031-8949/29/3/002. URL https://dx.doi.org/10.1088/0031-8949/29/3/002.

[63] C.-Y. Wong. *Landau hydrodynamics reexamined*. Phys. Rev. C **78**, 054902 (2008). doi:10.1103/PhysRevC.78.054902. URL https://link.aps.org/doi/10.1103/PhysRevC.78.054902.

[64] Y. B. Ivanov and D. Blaschke. *Baryon stopping in heavy-ion collisions at Elab = 2A-200A GeV*. The European Physical Journal A **52** (8), 237 (2016). ISSN 1434-601X. doi:10.1140/epja/i2016-16237-4. URL https://doi.org/10.1140/epja/i2016-16237-4.

[65] Y. B. Ivanov. *Alternative scenarios of relativistic heavy-ion collisions. I. Baryon stopping*. Phys. Rev. C **87**, 064904 (2013). doi:10.1103/PhysRevC.87.064904. URL https://link.aps.org/doi/10.1103/PhysRevC.87.064904.

[66] F. E. Harris, G. B. Arfken, and H. J. Weber. *Mathematical methods for physicists*. Academic Press, 7 edition (2011).